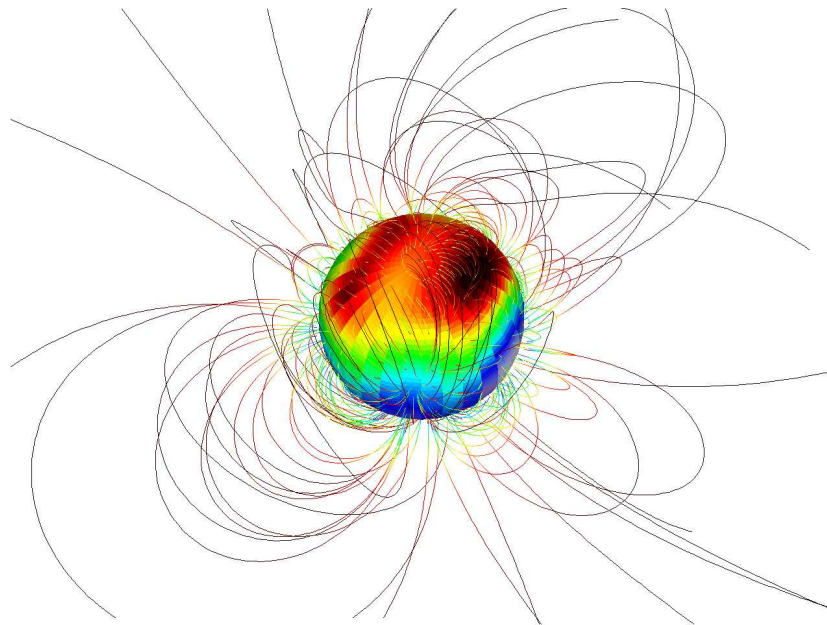


FABIAN EUCHNER

# ZEEMAN TOMOGRAPHY OF MAGNETIC WHITE DWARFS

DISSERTATION





# **Zeeman tomography of magnetic white dwarfs**

Dissertation  
zur Erlangung des Doktorgrades  
der Mathematisch-Naturwissenschaftlichen Fakultäten  
der Georg-August-Universität zu Göttingen

vorgelegt von

**Fabian Euchner**

aus

Kronberg/Taunus

Göttingen, 6. April 2006

D7

Referent: Prof. Dr. Klaus Beuermann

Korreferent: Prof. Dr. Sami K. Solanki

Tag der mündlichen Prüfung: 16. Mai 2006



*Freyheit über alles lieben, Wahrheit nie (auch sogar am Throne nicht) verleugnen.*

BEETHOVEN INS STAMMBUCH VON JOHANNA THEODORA VOCKE, 1793



# Zusammenfassung

Fabian Euchner:  
Zeeman tomography of magnetic white dwarfs

Das Ziel dieser Arbeit war die Entwicklung einer Methode, die geeignet ist, die Magnetfeldverteilung auf der Oberfläche magnetischer Weißer Zwerge anhand einer Sequenz rotationsphasen aufgelöster Fluss- und zirkular polarisierter Spektren zu bestimmen. Ich habe hierfür ein dreidimensionales Gitter, bestehend aus 46 800 theoretischen Stokes  $I$ - und  $V$ -Profilen berechnet, wobei der Betrag der Magnetfeldstärke, die Magnetfeldrichtung relativ zur Sichtlinie und die Effektivtemperatur freie Parameter sind. Mit Hilfe dieser Datenbank von Modellspektren kann das Zeeman-Spektrum eines magnetischen Weißen Zwergs mit vorgegebener Verteilung der Feldvektoren auf der Oberfläche schnell synthetisiert werden. Zur Parametrisierung des Felds wird einerseits eine abgebrochene Multipolentwicklung, andererseits ein Hybridmodell aus gekippten und dezentrierten zonalen Multipolkomponenten benutzt. Ich habe einen Algorithmus zur Bestimmung der optimal angepassten Feldstruktur ausgehend von einem Satz vorgegebener Spektren entwickelt, der auf einer  $\chi^2$ -Minimierung eines Satzes magnetischer Parameter beruht. Die Optimierungsaufgabe wird mit Hilfe einer Evolutionsstrategie gelöst. Die Methode wurde an synthetischen, künstlich verrauschten Ausgangsspektren getestet. Es zeigte sich, dass die einzelnen Flussspektren ein Signal-zu-Rausch-Verhältnis von 50–100 aufweisen müssen, um die ursprüngliche Feldgeometrie verlässlich zu rekonstruieren. Ebenso ist das Vorhandensein der wellenlängenabhängigen zirkularen Polarisation erforderlich.

Diesem Analyseverfahren wurden zwei Objekte unterzogen, deren phasenaufgelöste Fluss- und zirkular polarisierte Spektren mit dem FORS1-Spektrographen des *Very Large Telescope* der ESO mit acht Metern Spiegeldurchmesser aufgenommen wurden. Die Ergebnisse lieferten erstmalig detaillierte Karten der Magnetfeldverteilung auf der Sternoberfläche. Für HE 1045–0908 konnte gute Übereinstimmung zwischen den angepassten Modellen und den Beobachtungsdaten erzielt werden. Das Magnetfeld ist hauptsächlich durch eine Quadrupolkomponente gekennzeichnet, und die häufigste Feldstärke auf der Oberfläche ist  $\sim 16$  MG. Bei PG 1015+014 hat das Feld eine komplexere Struktur. Es ist durch Oktupole, möglicherweise auch durch noch höhere Multipole dominiert. Der hauptsächlich vorherrschende Magnetfeldbereich ist 70–80 MG. Es treten Abweichungen zwischen der Beobachtung und den angepassten Modellen auf, die darauf schließen lassen, dass die von uns verwendeten Feldmodelle womöglich zu grob für eine präzise Beschreibung sind.

Im Zuge dieser Arbeit konnten die genauesten Feldbestimmungen bei magnetischen Weißen Zwergen gewonnen werden, die es zur Zeit gibt. Zeeman-Tomographie hat sich als geeignete Methode erwiesen, um in Zukunft weiteren Aufschluss über die Magnetfeldeigenschaften magnetischer Weißer Zwerge und ihre Rolle bei der Sternentwicklung zu erhalten.



# Abstract

Fabian Euchner:  
Zeeman tomography of magnetic white dwarfs

The aim of this work has been to develop a method that allows to derive the distribution of the surface magnetic fields of magnetic white dwarfs from a set of rotation-phase resolved flux and circular polarization spectra. I have computed a three-dimensional grid of 46 800 theoretical Stokes  $I$  and  $V$  profiles, with the absolute magnetic field strength, the field direction relative to the line of sight, and the effective photospheric temperature as free parameters. The emerging Zeeman spectrum for a magnetic white dwarf with a given distribution of field vectors across its surface can be synthesised from this database of model spectra. For the field parametrization, either a truncated expansion in spherical harmonics or a hybrid model consisting of tilted and off-centred zonal multipole components is used. I have developed an algorithm to determine the best-fitting field structure for a set of given input spectra by a  $\chi^2$ -minimisation of the magnetic field parameters. For the optimisation, an evolutionary strategy is used. The method has been tested on synthetically generated input spectra with artificial noise. It has been found that a signal-to-noise ratio of 50–100 in the individual flux spectra and the inclusion of circular polarization spectra is essential for a reliable reconstruction of the original field geometry.

The method has been applied to phase-resolved flux and circular polarization spectra of two objects that have been obtained with the FORS1 spectrograph at the 8-m ESO *Very Large Telescope*. The results yield for the first time maps of the surface magnetic field distribution with hitherto unknown detail. For HE 1045–0908, the best fitting models are in good agreement with the observations. I find strong evidence for a magnetic field that is largely dominated by a quadrupolar component. The most frequent field strength on the surface is  $\sim 16$  MG. The field of PG 1015+014 is more complex, and is dominated by the octupole and probably even higher multipoles. The dominating field range is 70–80 MG. Remaining discrepancies between observations and the best fitting models suggest that the true field is more complex than can be described by our field models.

In the course of this thesis, the most accurate field determinations of magnetic white dwarfs so far have been obtained. Zeeman tomography has proven its usefulness in order to gain further insight into the properties of magnetic white dwarfs and their role in stellar evolution.



# Contents

<b>Contents</b>	<b>xii</b>
<b>List of Figures</b>	<b>xviii</b>
<b>List of Tables</b>	<b>xx</b>
<b>1 Introduction</b>	<b>1</b>
1.1 Properties of magnetic white dwarfs . . . . .	1
1.1.1 The occurrence of magnetism in white dwarfs . . . . .	2
1.1.2 Distribution of field strengths . . . . .	2
1.1.3 Distribution of rotational periods . . . . .	2
1.1.4 Distribution of masses . . . . .	3
1.1.5 Distribution of temperatures and chemical abundances . . . . .	3
1.2 Origin and evolution of magnetic fields . . . . .	4
1.3 Organisation of this thesis . . . . .	5
<b>2 Reconstruction of the field geometry from synthetic spectra</b>	<b>7</b>
2.1 Abstract . . . . .	8
2.2 Introduction . . . . .	8
2.3 The database . . . . .	9
2.3.1 Radiative transfer for magnetic white dwarfs . . . . .	9
2.3.2 Database spectra . . . . .	10
2.4 Magnetic field geometry . . . . .	10
2.5 Input spectra for the reconstruction procedure . . . . .	13
2.5.1 Integration of the database models . . . . .	13
2.5.2 Relation to the observed flux . . . . .	15
2.5.3 Limb darkening . . . . .	15
2.6 Reconstruction of the field geometry . . . . .	15
2.6.1 Magnetic field models . . . . .	16
2.6.2 Optimization algorithm . . . . .	20
2.6.3 Reconstruction fits . . . . .	24
2.7 Discussion . . . . .	27
2.7.1 Present approach . . . . .	27
2.7.2 Different optimization strategies . . . . .	28
2.7.3 The ZEBRA approach . . . . .	28
2.7.4 A future approach . . . . .	29
2.8 Conclusion . . . . .	29
2.9 Acknowledgements . . . . .	29
2.10 Appendix: Table of best-fit parameters . . . . .	29

<b>3</b>	<b>The quadrupole-dominated magnetic field of HE 1045–0908</b>	<b>33</b>
3.1	Abstract . . . . .	34
3.2	Introduction . . . . .	34
3.3	Observations . . . . .	35
3.3.1	Data reduction . . . . .	36
3.3.2	Data analysis . . . . .	36
3.4	Qualitative analysis of the magnetic field geometry . . . . .	38
3.5	Zeeman tomography of the magnetic field . . . . .	40
3.5.1	Field parametrization . . . . .	41
3.5.2	Results . . . . .	41
3.6	Discussion . . . . .	47
3.7	Acknowledgements . . . . .	49
3.8	Appendix: Table of best-fit parameters . . . . .	49
<b>4</b>	<b>The 70–80 Megagauss magnetic field of PG 1015+014</b>	<b>51</b>
4.1	Abstract . . . . .	52
4.2	Introduction . . . . .	52
4.3	Observations . . . . .	53
4.4	Qualitative analysis of the magnetic field geometry . . . . .	55
4.5	Zeeman tomography of the magnetic field . . . . .	57
4.5.1	Field parametrization . . . . .	58
4.5.2	Results . . . . .	59
4.6	Discussion . . . . .	66
4.7	Acknowledgements . . . . .	69
<b>5</b>	<b>Conclusions and Outlook</b>	<b>71</b>
<b>A</b>	<b>Additional fit results for HE 1045–0908</b>	<b>75</b>
<b>B</b>	<b>Additional fit results for PG 1015+014</b>	<b>81</b>
<b>C</b>	<b>MWDcat – an interactive, online catalogue of magnetic white dwarfs</b>	<b>89</b>
	<b>Bibliography</b>	<b>I</b>
	<b>Acknowledgements / Danksagungen</b>	<b>IX</b>
	<b>List of publications</b>	<b>XI</b>
	<b>Curriculum Vitae</b>	<b>XIII</b>



# List of Figures

2.1	Examples of the database spectra for $B = 20$ MG, $T = 15\,000$ K, and five angles of $\psi$ equally spaced in $\cos \psi$ covering the H $\alpha$ $\sigma^-$ -, $\pi$ -, and $\sigma^+$ -components. <b>a)</b> Intensity, <b>b)</b> degree of circular polarization. The spectra are shifted vertically by arbitrary amounts to avoid overlap. . . . .	11
2.2	<b>a)</b> Rotational geometry of the MWD models. The $x$ -axis points towards the observer, the $z_0$ -axis marks the rotation axis. The dashed line marks the intersection of the $x$ - $z$ -plane with the $x_0$ - $y_0$ -plane. $i$ denotes the inclination, and $\omega$ the rotational phase angle. <b>b)</b> Magnetic geometry of the MWD models. The $z'$ - and $z''$ -axes mark the axes of symmetry for the dipole and quadrupole components. The lines of intersection of the $x'$ - $z'$ -plane and the $x''$ - $z''$ -plane with the $x_0$ - $y_0$ -plane are given by the dashed and the dotted lines, respectively. . . . .	12
2.3	Spectral flux ( <i>top</i> ) and circular polarization ( <i>bottom</i> ) for centred dipoles viewed pole-on with polar field strengths of (A) 200 MG, (B) 80 MG, and (C) 30 MG for $T = 15\,000$ K. The library-based spectra computed using a database of four $\mu$ -values (red) are compared to those for $\mu = 1$ , corrected with a mean limb darkening law (black). Spectra (A) and (B) have been shifted upwards to avoid overlap (1.1 flux units each). The insert shows the relative flux differences for the 30 MG case (C). . . . .	14
2.4	Model (A1), centred dipole viewed at $i = 60^\circ$ : <b>a)</b> $B$ - $\psi$ diagram, <b>b)</b> field strength and longitudinal component, <b>c)</b> flux and polarization spectra. The + and - symbols indicate the sign of the longitudinal component of the magnetic field. For clarity, the flux spectra at $\phi = 0.25, 0.5$ , and $0.75$ have been shifted upwards by one flux unit each. . . . .	16
2.5	<i>Top</i> : Model (A2), centred dipole viewed at $i = 30^\circ$ : <b>a)</b> $B$ - $\psi$ diagram, <b>b)</b> field strength and longitudinal component, <b>c)</b> flux and polarization spectra. <i>Bottom</i> : Model (B), pure quadrupole viewed at $i = 60^\circ$ : <b>a)</b> $B$ - $\psi$ diagram, <b>b)</b> field strength and longitudinal component, <b>c)</b> flux and polarization spectra. See Fig. 2.4 for further explanation. . . . .	17
2.6	<i>Top</i> : Model (C), aligned dipole and quadrupole viewed at $i = 60^\circ$ : <b>a)</b> $B$ - $\psi$ diagram, <b>b)</b> field strength and longitudinal component, <b>c)</b> flux and polarization spectra. <i>Bottom</i> : Model (D), shifted high-field dipole viewed at $i = 60^\circ$ : <b>a)</b> $B$ - $\psi$ diagram, <b>b)</b> field strength and longitudinal component, <b>c)</b> flux and polarization spectra. See Fig. 2.4 for further explanation. . . . .	18
2.7	<i>Top</i> : Model (E), shifted dipole viewed at $i = 60^\circ$ : <b>a)</b> $B$ - $\psi$ diagram, <b>b)</b> field strength and longitudinal component, <b>c)</b> flux and polarization spectra. <i>Bottom</i> : Model (F), non-aligned dipole-quadrupole combination viewed at $i = 60^\circ$ : <b>a)</b> $B$ - $\psi$ diagram, <b>b)</b> field strength and longitudinal component, <b>c)</b> flux and polarization spectra. See Fig. 2.4 for further explanation. . . . .	19

- 2.8 Examples of simulated spectra used as input to the reconstruction procedure. The  $\phi = 0$  spectrum of Model (A1) is shown with a signal-to-noise ratio  $S/N = 20$  and 100 (shifted upwards by one flux unit). *Top*: Flux spectra, *bottom*: circular polarization spectra. . . . . 21
- 2.9 *Left panel*: Contour plot of the  $\chi^2$ -landscape for the spectral flux in the  $B_{\text{pol}}^q, \Theta^q$ -plane. The input configuration is given by  $B_{\text{pol}}^d = 40$  MG,  $B_{\text{pol}}^q = 20$  MG, and  $\Theta^d = \Theta^q = 0^\circ$ . Darker shading corresponds to smaller values of  $\chi_{\text{red}}^2$ . *Centre panel*:  $B$ - $\psi$  diagrams of the field configurations corresponding to the local (*top*) and the global (*bottom*) minimum. *Right panel*: Flux and circular polarization spectra corresponding to the the global minimum (lower curves) and the local minimum in the upper left of the left panel (upper curves, shifted upwards by 0.5 units in flux and 0.1 units in polarization). . . . . 23
- 2.10 Aitoff maps of the magnetic field strength  $B$  (in MG) for Model (A1). The input (*top*) and the high-noise flux-only reconstruction of Table 2.1, Model (A1), line 10 (*bottom*) are shown. The axis of the maps represents the rotation axis. The centre of the maps marks the  $-x_0$  direction (see Fig. 2.2b). The region within  $30^\circ$  from the lower pole is permanently hidden (dashed white line). . . . . 25
- 2.11 Aitoff maps of the field strength  $B$  (in MG) showing the results of reconstruction fits for the Model (F) field distribution (non-aligned dipole-quadrupole combination). The centre of the maps marks the  $-x_0$  direction. The axis of the quadrupole and the field direction at its poles is indicated by the  $+$  and  $-$  symbols, the axis of the dipole correspondingly by the circled  $+$  and  $-$  symbols (see text). **a**) Input field, **b**) low-noise flux-and-polarization reconstruction of Table 2.1, Model (F), line 1, **c**) high-noise flux-only reconstruction of line 4, and **d**) high-noise flux-only reconstruction of line 6. . . . . 26
- 3.1 *Left panel*: Flux spectra of HE 1045–0908 from June 1999 (1–5) and December 1999 (6–7). Spectra 2–7 have been shifted upwards by two flux units each with an additional unit between spectra 5 and 6. *Right panel*: Combined flux and circular polarization spectra of HE 1045–0908 from the June/December 1999 observations, covering approximately one-half of the rotation cycle. These spectra, which have been collected into three phase bins, have been used as input spectra for the Zeeman tomographic procedure. For clarity, the uppermost two curves have been shifted upwards by one and two flux units, respectively. The quoted phases refer to case (i) with  $P_{\text{rot}} = 2.7$  h. . . . . 37
- 3.2 Zeeman maximum ( $\phi = 0$ ) flux  $f_\lambda$  (in units of  $10^{-16}$  erg cm $^{-2}$  s $^{-1}$ ) and circular polarization  $V/I$  of HE 1045–0908, plotted along with the theoretically predicted field-dependent transition wavelengths ( $\lambda$ - $B$  curves) for Balmer absorption lines. The top panel also shows a theoretical circular polarization spectrum for a model atmosphere permeated by a homogeneous field of  $B = 16$  MG (shifted upwards by 0.07 units, with the horizontal dashed grey line denoting the zero polarization level). In the bottom panel, filled circles denote unambiguous identifications of transitions. . . . . 39

- 3.3 Observed circular polarization spectra for phases  $\phi = 0.0$  and  $0.5$  (black curves) and best-fit synthetic spectra (red curves) for different parametrizations of the magnetic field geometry. From top to bottom: centred dipole (D ctrd); centred quadrupole (Q ctrd); off-centred dipole (D offs); off-centred quadrupole (Q offs); centred, non-aligned combination of dipole, quadrupole, and octupole (DQO na ctrd); off-centred, non-aligned combination of dipole, quadrupole, and octupole (DQO na offs). All curves except for the bottom one have been shifted vertically by suitable amounts in  $V/I$ , with the horizontal dashed lines indicating the respective levels of zero polarization. The quoted phases refer to case (i) with  $P_{\text{rot}} = 2.7$  h. . . . . 42
- 3.4 Zeeman tomographic analysis of the magnetic field configuration of HE 1045–0908 using a centred, non-aligned combination of dipole, quadrupole, and octupole. *Top*: Observed (black curves) and best-fit synthetic spectra (red curves). The uppermost two flux (circular polarization) spectra have been shifted for clarity by 2 and 4 (0.1 and 0.2) units in  $f_{\lambda}$  ( $V/I$ ). The quoted phases refer to case (i) with  $P_{\text{rot}} = 2.7$  h. *Bottom left*:  $B$ - $\psi$  diagram, *bottom right*: absolute value of the surface magnetic field, cosine of the angle  $\psi$  between the magnetic field direction and the line of sight, and maximum radial distance reached by field lines in units of the white dwarf radius (see text). . . . . 44
- 3.5 Zeeman tomographic analysis of the magnetic field configuration of HE 1045–0908 using an off-centred, non-aligned combination of dipole, quadrupole, and octupole. *Top*: Observed (black curves) and best-fit synthetic spectra (red curves). The uppermost two flux (circular polarization) spectra have been shifted for clarity by 2 and 4 (0.1 and 0.2) units in  $f_{\lambda}$  ( $V/I$ ). The quoted phases refer to case (i) with  $P_{\text{rot}} = 2.7$  h. *Bottom left*:  $B$ - $\psi$  diagram, *bottom right*: absolute value of the surface magnetic field, cosine of the angle  $\psi$  between the magnetic field direction and the line of sight, and maximum radial distance reached by field lines in units of the white dwarf radius (see text). . . . . 45
- 4.1 *Left panel*: Flux spectra of PG 1015+014 from May 1999. The uppermost 11 spectra have been shifted upwards by 2 flux units, respectively. *Right panel*: Combined flux and circular polarization spectra of PG 1015+014 from the May 1999 observations. These spectra, which have been collected into five phase bins, will be used as input spectra for the Zeeman tomography procedure. For clarity, the uppermost four flux spectra have been shifted upwards by 1.5 flux units, respectively. The tick marks below the top axis indicate the wavelengths that were used to adjust the continuum flux level of the the model spectra to the observations. . . . . 54
- 4.2 Zeeman maximum ( $\phi = 0.25$ , *left panel*) and minimum ( $\phi = 0.86$ , *right panel*) flux ( $f_{\lambda}$ ) and circular polarization ( $V/I$ ) spectra for PG 1015+014, plotted along with the theoretically predicted field-dependent transition wavelengths for Balmer absorption lines ( $\lambda$ - $B$  curves). Transitions corresponding formally to  $|\Delta l| = 0, 2, 4, \dots$  with the zero-field angular momentum quantum number  $l$  have been plotted as dashed curves in the bottom parts of the figures. Filled circles denote unambiguous identifications of transitions, open circles less certain ones. In the top parts, theoretical circular polarization spectra are shown for comparison (shifted upwards for clarity, see the text for the adopted model parameters).  $f_{\lambda}$  is given in units of  $10^{-16} \text{ erg cm}^{-2} \text{ s}^{-1}$ . . . . . 56

- 4.3 Observed circular polarization spectra for phases  $\phi = 0.25$  and  $0.86$  (black curves) and best-fit synthetic spectra (red curves) for different parametrizations of the magnetic field geometry. From top to bottom: off-centred dipole (D offs); centred, non-aligned combination of dipole, quadrupole, and octupole (DQO na ctrd); off-centred, non-aligned combination of dipole, quadrupole, and octupole (DQO na offs); superposition of three individually off-centred, non-aligned dipoles (DDD sum); truncated multipole expansion up to degree  $l = 4$ . The lowermost two curves show individual fits to single phases with a truncated multipole expansion up to  $l = 5$  ( $\phi = 0.25$ ) and  $l = 4$  ( $\phi = 0.86$ ). All curves except for the bottom one have been shifted vertically by suitable amounts in  $V/I$ , with the horizontal dashed lines indicating the respective levels of zero polarization. . . . . 60
- 4.4 Observed spectra of PG 1015+014 (black curves) and best-fit synthetic spectra (red curves) using a superposition of three individually off-centred, non-aligned dipoles. The upper four flux (circular polarization) spectra have been shifted for clarity by 2, 4, 6, and 8 (0.1, 0.2, 0.3, and 0.4) units in  $f_\lambda$  ( $V/I$ ). . . . . 64
- 4.5 Zeeman tomographic analysis of the magnetic field configuration of PG 1015+014 using a superposition of three individually off-centred, non-aligned dipoles. *Left panel:*  $B$ - $\psi$  diagram, *right panel:* absolute value of the surface magnetic field, cosine of the angle  $\psi$  between the magnetic field direction and the line of sight, and maximum radial distance reached by field lines in units of the white dwarf radius. 65
- 4.6 Observed spectra of PG 1015+014 (black curves) and best-fit synthetic spectra (red curves) for a truncated multipole expansion up to degree  $l = 4$ . For clarity, the upper four flux (polarization) spectra have been shifted upwards by 2, 4, 6, and 8 (0.1, 0.2, 0.3, and 0.4) units in  $f_\lambda$  ( $V/I$ ). . . . . 66
- 4.7 Zeeman tomographic analysis of the magnetic field configuration of PG 1015+014 using a truncated multipole expansion up to degree  $l = 4$ . *Left panel:*  $B$ - $\psi$  diagram, *right panel:* absolute value of the surface magnetic field, cosine of the angle  $\psi$  between the magnetic field direction and the line of sight, and maximum radial distance reached by field lines in units of the white dwarf radius. 67
- 4.8 Best-fit results for individual single phase fits to the Zeeman maximum ( $\phi = 0.25$ , *bottom panels*) and minimum ( $\phi = 0.86$ , *top panels*) phases. The field has been parametrized by a truncated multipole expansion up to degree  $l = 5$  for  $\phi = 0.25$ , and up to  $l = 4$  for  $\phi = 0.86$ . *Left panels:*  $B$ - $\psi$  diagram, *right panels:* absolute value of the surface magnetic field, cosine of the angle  $\psi$  between the magnetic field direction and the line of sight, and maximum radial distance reached by field lines in units of the white dwarf radius. . . . . 68
- A.1 Zeeman tomographic analysis of the magnetic field configuration of HE 1045–0908 using a centred dipole model. *Top:* Observed (black curves) and best-fit synthetic spectra (red curves). The uppermost two flux (circular polarization) spectra have been shifted for clarity by 2 and 4 (0.1 and 0.2) units in  $f_\lambda$  ( $V/I$ ). The quoted phases refer to case (i) with  $P_{\text{rot}} = 2.7$  h. *Bottom left:*  $B$ - $\psi$  diagram, *bottom right:* absolute value of the surface magnetic field, cosine of the angle  $\psi$  between the magnetic field direction and the line of sight, and maximum radial distance reached by field lines in units of the white dwarf radius. . . . . 76

- A.2 Zeeman tomographic analysis of the magnetic field configuration of HE 1045–0908 using a centred quadrupole model. *Top*: Observed (black curves) and best-fit synthetic spectra (red curves). The uppermost two flux (circular polarization) spectra have been shifted for clarity by 2 and 4 (0.1 and 0.2) units in  $f_\lambda$  ( $V/I$ ). The quoted phases refer to case (i) with  $P_{\text{rot}} = 2.7$  h. *Bottom left*:  $B$ – $\psi$  diagram, *bottom right*: absolute value of the surface magnetic field, cosine of the angle  $\psi$  between the magnetic field direction and the line of sight, and maximum radial distance reached by field lines in units of the white dwarf radius. . . . . 77
- A.3 Zeeman tomographic analysis of the magnetic field configuration of HE 1045–0908 using an off-centred dipole model. *Top*: Observed (black curves) and best-fit synthetic spectra (red curves). The uppermost two flux (circular polarization) spectra have been shifted for clarity by 2 and 4 (0.1 and 0.2) units in  $f_\lambda$  ( $V/I$ ). The quoted phases refer to case (i) with  $P_{\text{rot}} = 2.7$  h. *Bottom left*:  $B$ – $\psi$  diagram, *bottom right*: absolute value of the surface magnetic field, cosine of the angle  $\psi$  between the magnetic field direction and the line of sight, and maximum radial distance reached by field lines in units of the white dwarf radius. . . . . 78
- A.4 Zeeman tomographic analysis of the magnetic field configuration of HE 1045–0908 using an off-centred quadrupole model. *Top*: Observed (black curves) and best-fit synthetic spectra (red curves). The uppermost two flux (circular polarization) spectra have been shifted for clarity by 2 and 4 (0.1 and 0.2) units in  $f_\lambda$  ( $V/I$ ). The quoted phases refer to case (i) with  $P_{\text{rot}} = 2.7$  h. *Bottom left*:  $B$ – $\psi$  diagram, *bottom right*: absolute value of the surface magnetic field, cosine of the angle  $\psi$  between the magnetic field direction and the line of sight, and maximum radial distance reached by field lines in units of the white dwarf radius. . . . . 79
- B.1 Observed (black curves) and best-fit synthetic spectra (red curves) for PG 1015+014 using an off-centred dipole model. The uppermost four flux (circular polarization) spectra have been shifted for clarity by 2, 4, 6, and 8 (0.1, 0.2, 0.3, and 0.4) units in  $f_\lambda$  ( $V/I$ ). . . . . 82
- B.2 Zeeman tomographic analysis of the magnetic field configuration of PG 1015+014 using an off-centred dipole model. *Left panel*:  $B$ – $\psi$  diagram, *right panel*: absolute value of the surface magnetic field, cosine of the angle  $\psi$  between the magnetic field direction and the line of sight, and maximum radial distance reached by field lines in units of the white dwarf radius. . . . . 83
- B.3 Observed (black curves) and best-fit synthetic spectra (red curves) for PG 1015+014 using a centred, non-aligned combination of dipole, quadrupole, and octupole components. The uppermost four flux (circular polarization) spectra have been shifted for clarity by 2, 4, 6, and 8 (0.1, 0.2, 0.3, and 0.4) units in  $f_\lambda$  ( $V/I$ ). . . . . 84
- B.4 Zeeman tomographic analysis of the magnetic field configuration of PG 1015+014 using a centred, non-aligned combination of dipole, quadrupole, and octupole components. *Left panel*:  $B$ – $\psi$  diagram, *right panel*: absolute value of the surface magnetic field, cosine of the angle  $\psi$  between the magnetic field direction and the line of sight, and maximum radial distance reached by field lines in units of the white dwarf radius. . . . . 85

- 
- B.5 Observed (black curves) and best-fit synthetic spectra (red curves) for PG 1015+014 using an off-centred, non-aligned combination of dipole, quadrupole, and octupole components. The uppermost four flux (circular polarization) spectra have been shifted for clarity by 2, 4, 6, and 8 (0.1, 0.2, 0.3, and 0.4) units in  $f_\lambda$  (V/I). 86
- B.6 Zeeman tomographic analysis of the magnetic field configuration of PG 1015+014 using an off-centred, non-aligned combination of dipole, quadrupole, and octupole components. *Left panel:*  $B$ - $\psi$  diagram, *right panel:* absolute value of the surface magnetic field, cosine of the angle  $\psi$  between the magnetic field direction and the line of sight, and maximum radial distance reached by field lines in units of the white dwarf radius. . . . . 87

# List of Tables

1.1	Break-down of the known magnetic white dwarfs into spectral classes. The numbers quoted in the column ‘pre-SDSS’ reflect the census prior to the <i>Sloan Digital Sky Survey</i> . They are compiled from Table 1 of <a href="#">WF00</a> (60 objects), plus the objects LHS 2534 (DZ, <a href="#">Reid et al. 2001</a> ) and HE 0241–0155 (DA, <a href="#">Reimers et al. 2004</a> ). Five objects from the list of <a href="#">WF00</a> have later been found not to be MWDs (HE 0127-3110, HE 2201-2250, HE 0003-5701, HE 0026-2150, HE 0107-0158). The other columns list the numbers of MWDs found in the Data Release 1 ( <a href="#">S03</a> ) and in the Data Releases 2 and 3 ( <a href="#">V05</a> ) of the SDSS. . . . .	4
2.1	Reconstructed magnetic parameters for the configurations (A)–(F). Each model is introduced by a boldface line which lists the input parameters. The subsequent numbered lines represent the individual reconstructions. In the ‘flag’ column, ‘fp’ denotes simultaneous fits to flux and polarization spectra, ‘f’ fits to flux spectra only. The last column indicates the success rate of the convergence of the multidimensional parameter search. Note that for (B) and (C), $\Theta^a = \Theta^d$ and $\Phi^a = \Phi^d$ . . .	30
3.1	Dates and times for the spectropolarimetric observations of HE 1045–0908 obtained at the ESO VLT ( $t_{\text{exp}}$ : exposure time, n: number of exposures). . . . .	35
3.2	Best-fit magnetic parameters for the different parametrizations of the magnetic field shown in Fig. <a href="#">3.3</a> . The uncertainties in the last digit are denoted by the values in brackets. A short description of the individual models is followed by the formal value of the reduced $\chi^2$ (see text). All models assume a rotational period of 2.7 h, except for model (7), which has been computed for 5.4 h. . . . .	50
4.1	Positions of observed Zeeman features and corresponding Balmer transitions. A colon denotes a less certain identification. . . . .	57
4.2	Best-fit magnetic parameters for the different parametrizations of the magnetic field shown in Fig. <a href="#">4.3</a> . The uncertainties in the last digit are denoted by the values in brackets. For each model, a short description is given in the first line. The best-fit inclinations are $24^\circ \pm 3^\circ$ (model 1), $45^\circ \pm 3^\circ$ (model 2), and $36^\circ \pm 4^\circ$ (model 3). The superscripts ‘d’, ‘q’, and ‘o’ refer to dipole, quadrupole, and octupole, the subscript ‘pol’ to the polar field strength. The last three columns give the offsets in units of the white dwarf radius. Formulae for the field structure are given in Paper I. . . . .	61
4.3	Best-fit magnetic parameters for a superposition of three individually off-centred, non-aligned dipoles (labelled DDD sum in Fig. <a href="#">4.3</a> ). The individual dipole components are denoted by D1, D2, and D3. The uncertainties in the last digit are given by the values in brackets. The best-fit inclination is $23^\circ \pm 4^\circ$ . . . . .	62



---

4.4	Best-fit magnetic parameters for a truncated multipole expansion up to degree $l = 4$ (labelled M in Fig. 4.3). The coefficients $g_l^m$ and $h_l^m$ are in MG. The best-fit inclination is $47^\circ$ . The tilt and the azimuth of the multipole axis relative to the rotational axis are $22^\circ$ and $191^\circ$ . . . . .	62
-----	--	----



# 1 Introduction

In 1844, F. W. Bessel noticed a periodic variation in the proper motion trajectory of Sirius, and attributed this effect to the existence of an unseen companion, Sirius B, which was visually discovered for the first time in 1862. W. S. Adams observed in 1914 that Sirius B had a spectrum of a “white” star, i.e., a rather high surface temperature.<sup>1</sup> Given the object’s faintness, it became clear that the radius of Sirius B is two orders of magnitude smaller than the radii of late-type main-sequence stars. At the same time, a mass of the order of one solar mass was evident from the orbital motion measurements. Consequently, the density had to be  $\sim 10^4$  times higher than the density for any other known star. Sirius B was the first member of a new class of objects called the *White Dwarfs*. R. H. Fowler showed in 1926 that for these objects the pressure that counteracts self gravitation is due to the quantum-mechanical effect of a degenerated electron gas, which was postulated only a few months before by E. Fermi and P. A. M. Dirac.

It was found later that white dwarfs are very numerous in the Galaxy and a common end product of stellar evolution. All stars with  $M \lesssim 8 M_{\odot}$  evolve into white dwarfs once their nuclear fuel is exhausted. Since white dwarfs have only minimal energy production, they form a cooling sequence, radiating away their thermal energy, and end their lives in oblivion.

## 1.1 Properties of magnetic white dwarfs

The atmospheric composition of white dwarfs is dominated either by hydrogen (the DA white dwarfs) or by helium (the DB white dwarfs). This holds for most of the white dwarfs, while there is a small fraction of objects with mixed composition, or with metal lines (see [Sion et al. 1983](#) and [Wesemael et al. 1991](#) for a classification scheme). The spectra of the pure DA and DB white dwarfs are characterised by heavily pressure-broadened absorption lines at the respective laboratory wavelengths of the hydrogen and helium transitions. However, early detections reported “peculiar” spectra for several white dwarfs that did not fit into any known scheme. The most famous object of this class is Grw +70°8247 with its *Minkowski bands* ([Minkowski 1938](#)), which remained a mystery for nearly 50 years. For many of these peculiar objects the emission of polarized light could be detected. This is a strong hint for a magnetic nature of these objects. Meanwhile, magnetism in white dwarfs can be verified reliably thanks to the advances in the theoretical treatment of the physical properties of hydrogen and helium atoms in high magnetic fields. Major efforts in this direction have been made in the 1980s at the University of Louisiana at Baton Rouge ([Henry & O’Connell 1984, 1985](#)), and at the University of Tübingen ([Forster et al. 1984](#); [Rösner et al. 1984](#); [Wunner et al. 1985](#)). Today, the comparison of observed Zeeman spectra with synthetically generated model spectra is the most powerful diagnostic tool to derive the magnetic properties of white dwarfs. The aim of this thesis has been to develop a general method for the

---

<sup>1</sup> The temperature of Sirius B has recently been determined to be in the range of 24 790 K ([Holberg et al. 1998](#)) to 25 190 K ([Barstow et al. 2005](#)).

determination of the surface magnetic field geometry along these lines, and to apply this technique to selected objects.

### 1.1.1 The occurrence of magnetism in white dwarfs

In March 2006, the Web Version<sup>2</sup> of the Villanova White Dwarf Catalog – the most complete database on white dwarfs publicly available – listed 5506 objects (McCook & Sion 1999). The number of known magnetic white dwarfs (MWDs) is about 170 (Wickramasinghe & Ferrario 2000; Gänsicke et al. 2002; Schmidt et al. 2003; Vanlandingham et al. 2005).<sup>3</sup> These numbers suggest a fraction of MWDs of  $\sim 3\%$ . The true value, however, is probably significantly higher, mainly because MWDs with very small and also with very large fields are difficult to identify. Due to their intrinsic faintness, large telescopes are needed, and the circular and/or linear polarization has to be recorded. Recent statistical studies find evidence for a true fractional incidence of up to 20% (Kawka 2003; Liebert et al. 2003).

### 1.1.2 Distribution of field strengths

The magnetic field strengths that have been detected in MWDs span a range of 2 kG–1000 MG, with the majority showing fields of  $\gtrsim 1$  MG. At present, only four objects with very small fields (below 30 kG) are known (Aznar Cuadrado et al. 2004; Fabrika & Valyavin 1999), and another seven objects between 30 kG and 1 MG. It is likely, however, that the true fraction of white dwarfs with fields below 1 MG is substantially higher. This assumption is supported by recent studies of central stars of planetary nebulae (Jordan et al. 2005), and of hot subdwarfs (O’Toole et al. 2005), which find a relatively high occurrence of magnetism among these objects. As a caveat, it has to be noted that the samples used in these studies are very small. Magnetic field values as low as 2 kG, as detected in the study of Aznar Cuadrado et al. (2004), define the current detection limit with 8-m class telescopes.

### 1.1.3 Distribution of rotational periods

In general, white dwarfs are “slow rotators” (i.e., their rotational velocities are much smaller than the theoretical breakup velocities). This is attributed to angular momentum loss in the post-main sequence evolution, which is caused by a stellar wind, and possibly by magnetic braking if magnetic fields are involved (Villata 1992). Typical rotational periods of non-magnetic white dwarfs – which are difficult to measure – are of the order of several hours up to 1 day (Koester & Herrero 1988; Winget et al. 1991; Heber et al. 1997). Rotation is more easily detected in MWDs, because many of them show a periodic variation in broad-band polarization. The distribution of rotational periods for MWDs spans a remarkably wide range and is markedly bimodal, with a preference of the extreme values at the edges (Wickramasinghe & Ferrario 2000, hereafter WF00). There are several objects, including those studied in this thesis, with confirmed rotational periods ranging from 12 min (RE J0137–853, Barstow et al. 1995) up to a few hours (Schmidt & Norsworthy 1991), while other objects show signs of slow rotation with periods of several days. There are

<sup>2</sup> <http://www.astronomy.villanova.edu/WDCatalog/index.html>

<sup>3</sup> 105 of these objects have been found during the last four years in the course of the *Sloan Digital Sky Survey* (see Table 1.1).

also a few objects which show no signs of rotation on a time scale of several decades, thus indicating rotational periods of  $\gtrsim 100$  years.<sup>4</sup> A well-studied object of this class is, e.g., LP 790–29 (Beuermann & Reinsch 2002; Jordan & Friedrich 2002). The slowly rotating objects are thought to have undergone spin-down caused by magnetic braking (see, e.g., Borra et al. 1982 and references therein). In order to explain the high rotational velocities observed for the other class of objects, it has been proposed that they have undergone binary-star evolution. It is a well-known scenario in binary evolution that accretion can lead to a spin-up of the magnetised accreting object (cf., for example, the situation in millisecond pulsars, see Bhattacharya 1996 for a review).

#### 1.1.4 Distribution of masses

Another hint for a possible binary evolution scenario is given by the distribution of masses of MWDs. Since the average mass of a sample of 16 MWDs with well-constrained masses ( $\gtrsim 0.95 M_{\odot}$ ) was found to be significantly in excess of the average mass of all white dwarfs, the possibility has to be considered that at least a part of the short-period MWDs are the results of double-degenerate mergers (Vennes 1999; WF00). The most spectacular object of this class is the aforementioned RE J0137–853, which has not only the shortest rotational period of all MWDs, but also the highest mass ( $1.35 M_{\odot}$ ), and a complex field geometry (Burleigh et al. 1999). Indications for similarly complex field geometries have also been found for other MWDs belonging to the group with short rotational periods: the two objects studied in this thesis; the helium-rich MWD HE 1211–1707 (Jordan et al. 2001; Schmidt et al. 2001); the peculiar object Feige 7 with a mixed atmospheric composition of helium and hydrogen (Achilleos et al. 1992); and the high-field MWD PG 1031+234 (Schmidt et al. 1986; Latter et al. 1987). This could be a hint that during the highly turbulent merging process a modification of the field structure towards more complex patterns, possibly caused by shearing motions and the tangling of field lines, takes place. As a word of caution, however, we note that high-quality phase-resolved spectra, which are essential prerequisites for the determination of the field structure with sufficient details, are more easily obtained for the objects with rotational periods up to a few hours.

#### 1.1.5 Distribution of temperatures and chemical abundances

As the results from the *Sloan Digital Sky Survey* show, the distribution of effective temperatures of MWDs extends from 4500 to  $\sim 50\,000$  K and is rather uniform up to 25 000 K. For higher temperatures, the number of known objects drops steeply. A slight preference of the temperature range where hydrogen lines are strongest can be noticed (Schmidt et al. 2003, hereafter S03; Vanlandingham et al. 2005, hereafter V05). Since the maximum equivalent width of Balmer absorption lines occurs around 12 000 K, stars of this temperature should have a slightly higher detection probability, especially if the observational data are very noisy. Up to now, 27 MWDs are known which do not have pure hydrogen atmospheres. This corresponds to 16 % of all MWDs, which is smaller than the fraction of  $\sim 25$  % observed in non-magnetic white dwarfs (S03), but this may be due to small-number statistics. Apart from magnetic DA white dwarfs, magnetic members of the spectral classes DB, DBA, DQ, DQA, and DZ have been found. Table 1.1 lists

<sup>4</sup> Not all of these very long periods are probably real, since such an effect could also be mimicked by a near-zero inclination, or a magnetic field that shows no azimuthal variations relative to the rotational axis. The latter possibility is indicative of a relatively simple field configuration that can be described with only zonal multipole components.

**Table 1.1:** Break-down of the known magnetic white dwarfs into spectral classes. The numbers quoted in the column ‘pre-SDSS’ reflect the census prior to the *Sloan Digital Sky Survey*. They are compiled from Table 1 of [WF00](#) (60 objects), plus the objects LHS 2534 (DZ, [Reid et al. 2001](#)) and HE 0241–0155 (DA, [Reimers et al. 2004](#)). Five objects from the list of [WF00](#) have later been found not to be MWDs (HE 0127-3110, HE 2201-2250, HE 0003-5701, HE 0026-2150, HE 0107-0158). The other columns list the numbers of MWDs found in the Data Release 1 ([S03](#)) and in the Data Releases 2 and 3 ([V05](#)) of the SDSS.

	pre-SDSS	<a href="#">S03</a>	<a href="#">V05</a>	$\Sigma$
overall	62	54	51	167
DA	47 <sup>a</sup>	45	48	140
non-DA	15	9	3	27
DB	7	3	–	10
DBA	3	–	–	3
DQ	4	5	1	10
DQA	–	–	2	2
DZ	1	1	–	2

<sup>a</sup> This number includes two objects with unclear spectral classification from [WF00](#) (HE 0236-2656, HE 0330-0002).

the number of objects belonging to the respective classes. It can be seen that the objects with helium-line dominated spectra (DB and DBA) comprise 8% of all MWDs, while the fractional occurrence for objects with carbon-feature dominated spectra (DQ and DQA) is 7%, and for other metal-line dominated spectra (DZ) is 1%.

## 1.2 Origin and evolution of magnetic fields

Two different scenarios have been discussed in the literature in order to explain the origin of the magnetic fields in white dwarfs: (i) the fields are “fossil”, i.e. they have existed already in the main-sequence (or even pre-main sequence) stage and have been amplified subsequently by contraction in the post-main sequence evolution; or (ii) the fields are generated by contemporary dynamo action in the white dwarf. While dynamos are known to be able to operate in the convective envelopes of cool WDs, as assumed for the pulsating DB magnetic white dwarf GD 358 with a variable weak field of  $B \simeq 1.3$  kG ([Markiel et al. 1994](#); [Thomas et al. 1995](#)), fields of the order of several tens of MG cannot be generated by this mechanism ([Fontaine et al. 1973](#)). Therefore, the fossil field hypothesis is commonly accepted as an explanation for the high-field MWDs with  $B \gtrsim 1$  MG. These objects are widely believed to have evolved from the chemically peculiar, magnetic Ap and Bp stars, which have magnetic fluxes of the same order of magnitude ( $10^{26}$ – $10^{27}$  G cm<sup>2</sup>). In the Ap/Bp stars, fields in the range  $\sim 0.2$ –25 kG have been measured ([Mathys 2001](#); [Aurière et al. 2003](#)). If the stellar radius shrinks by a factor of 100 in the post-main sequence evolution and flux conservation is assumed ( $BR^2 = \text{const.}$ ), fields of 2–250 MG are attained in the white dwarf stage. This scenario, however, is based on the assumption that the

magnetic flux is conserved to a large extent during post-main sequence evolution. It is not clear if this is true, since at least a small part of the magnetic flux should be expected to be carried away with the envelope material during the process. Nevertheless, there are plausible reasons for this evolutionary scenario: (i) the Ap and Bp stars show large-scale, globally organised, static magnetic fields like the MWDs; (ii) the modelling of the fields requires higher multipoles (quadrupoles and octupoles) for both classes; (iii) both object classes have similar magnetic fluxes; (iv) objects of both classes are predominantly slow rotators; (v) both object classes have similar frequencies and space distributions.

As mentioned in Sect. 1.1.1, recent studies have shown that the number of MWDs with fields well below 1 MG is likely to be much higher than the number of confirmed objects. For these objects (the low-field magnetic white dwarfs), the fossil field and flux conservation hypothesis with Ap and Bp stars as the progenitors is not convincing because of the obvious mismatch in the value of the magnetic flux, and because the space density of the Ap/Bp stars is too small. The question from which class of objects on the main sequence the low-field MWDs might have evolved is subject of an ongoing debate in the literature. Proposed predecessors are upper main sequence stars, probably A stars, with fields of  $\sim 1\text{--}10\text{ G}$ , which are impossible to measure with current instrumentation (Tout et al. 2004; Wickramasinghe & Ferrario 2005), or F/G stars with weak fields that are buried under convective envelopes (S03; Kawka 2003).

## 1.3 Organisation of this thesis

The thesis is organised as follows:

In Chapter 2 I introduce Zeeman tomography, a newly developed method to derive the surface magnetic field distribution on magnetic white dwarfs. I present the results of its application to synthetically generated input spectra with artificial noise and discuss the method's ability to recover the magnetic parameters that were used to create the original spectra.

In Chapter 3 the application of Zeeman tomography to HE 1045–0908 is presented. I have found evidence for a magnetic field topology that is largely dominated by a quadrupolar component.

In Chapter 4 I present the results of the Zeeman tomographic analysis of PG 1015+014. A complex field geometry with dominating field strengths of  $B \simeq 70\text{--}80\text{ MG}$  is found. Remaining discrepancies between the observation and the best-fitting model are discussed.

In Chapter 5 the prerequisites, abilities, and limitations of the method are discussed. I also address alternative approaches, possible improvements of the method, and promising targets for further Zeeman tomographic studies.

In the Appendices A and B, additional fit results are presented which have not been included in the published versions of Chapters 3 and 4.

In Appendix C, *MWDcat* is briefly introduced, a publicly accessible online database on magnetic white dwarfs that I have set up in Göttingen.

Chapters 2 and 3 have been published in the refereed journal *Astronomy & Astrophysics* (2002) **390**, 633–647 and *Astronomy & Astrophysics* (2005) **442**, 651–660. Chapter 4 has been accepted for publication in *Astronomy & Astrophysics*. The scientific results are entirely the result of my

work. The text of these papers was written by me and was discussed with the co-authors. All supplementary material – like figures – has been produced by me. I am co-author of three further refereed publications, of which I wrote only parts and which have not been included in the thesis. Furthermore, I am author or co-author of seven conference papers.

Of the co-authors of the three publications contained in this thesis, K. Beuermann is my supervisor, S. Jordan has written the original stellar atmosphere code with which the theoretical Zeeman spectra were calculated, K. Reinsch and F. V. Hessman have taken the observational data at the VLT telescope, and B. T. Gänsicke participated in the original observation proposal.

This thesis is based on observations collected at the European Southern Observatory, Paranal, Chile, under programme IDs 63.P-0003(A) and 64.P-0150(C).

This work was supported in part by BMBF/DLR grant 50 OR 9903 6.

## 2 Reconstruction of the field geometry from synthetic spectra

F. EUCHNER<sup>1</sup>, S. JORDAN<sup>1,2,3</sup>, K. BEUERMANN<sup>1</sup>, B.T. GÄNSICKE<sup>1</sup>, & F.V. HESSMAN<sup>1</sup>

<sup>1</sup> Universitäts-Sternwarte Göttingen, Geismarlandstr. 11, D-37083 Göttingen, Germany

<sup>2</sup> Institut für Astronomie und Astrophysik, Universität Kiel, D-24098 Kiel, Germany

<sup>3</sup> Institut für Astronomie und Astrophysik, Universität Tübingen, Sand 1, D-72076 Tübingen, Germany

Published in *Astronomy & Astrophysics* (2002) **390**, 633–647, [doi:10.1051/0004-6361:20020726](https://doi.org/10.1051/0004-6361:20020726)



## 2.1 Abstract

We have computed optical Zeeman spectra of magnetic white dwarfs for field strengths between 10 and 200 MG and effective temperatures between 8000 and 40 000 K. They form a database containing 20 628 sets of flux and circular polarization spectra. A least-squares optimization code based on an evolutionary strategy can recover relatively complex magnetic field topologies from phase-resolved synthetic Zeeman spectra of rotating magnetic white dwarfs. We consider dipole and quadrupole components which are non-aligned and shifted off-centre. The model geometries include stars with a single high-field spot and with two spots separated by  $\sim 90^\circ$ . The accuracy of the recovered field structure increases with the signal-to-noise ratio of the input spectra and is significantly improved if circular polarization spectra are included in addition to flux spectra. We discuss the strategies proposed so far to unravel the field geometries of magnetic white dwarfs.

## 2.2 Introduction

About 3% of all white dwarfs have strong magnetic fields between  $10^6$  and  $10^9$  Gauss (Wickramasinghe & Ferrario 2000; Jordan 2001). In many of these magnetic white dwarfs (MWDs), the surface field geometries deviate from simple centred dipoles. This holds for isolated MWDs and for the MWDs in accreting close binaries (Wickramasinghe & Ferrario 2000; Schwöpe 1995). While higher modes are often thought to decay on timescales longer than the  $\tau \gtrsim 10^{10}$  yr of the fundamental mode, Muslimov et al. (1995) showed that quadrupole or octupole components may survive via the Hall effect if an internal toroidal magnetic field component is present. Therefore, studies of the surface field structure provide clues on the internal field configuration and its influence on the evolution of MWDs.

The photospheric spectra of hydrogen-rich MWDs are characterized by broad absorption structures formed by the overlap of numerous components of the Balmer lines, shifted by hundreds or even thousands of Å from their zero-field positions by the linear and quadratic Zeeman effects. These shifts completely obliterate the Doppler shifts caused by rotation even in the most rapidly rotating MWDs. As a consequence, the Zeeman-Doppler imaging method devised for the analysis of rapidly rotating magnetically active main sequence stars (Semel 1989; Donati et al. 1989; Brown et al. 1991) is not applicable to MWDs. The field geometry of MWDs can be derived, however, from the analysis of the pure Zeeman splitting of the photospheric lines and their circular polarization properties as a function of rotational phase. Because of the large Zeeman shifts, this approach must include the whole optical range for  $B \gtrsim 50$  MG. In the absence of positional information from the Doppler effect, however, the inversion of the flux and polarization spectra is an intricate task. Trial-and-error fits of centred or shifted dipoles and quadrupoles (Wickramasinghe & Cropper 1988; Putney & Jordan 1995) are incapable of exploring the full parameter space of possible solutions. We present a new strategy using a pre-computed database of synthetic MWD spectra and an automatic quality-of-fit optimization algorithm.

A first approach along these lines was presented by Donati et al. (1994), who used a maximum entropy algorithm (MEM) to fit a matrix of areal filling factors for a grid of synthetic flux and circular polarization spectra to simulated input data. This way, they obtained the ‘simplest’ and, according to *Occam’s razor*, most likely frequency distribution of transverse and longitudinal field



strengths over the visible stellar disc at each rotational phase, a so-called ZEBRA plot, but this approach does not provide any information about the spatial structure of the magnetic field.

In this paper, we investigate to what extent the underlying global magnetic field distribution can be recovered directly from least-squares fits to phase-resolved flux and polarization spectra of a given signal-to-noise ratio. This approach uses the spatial information provided by the magnetic fields seen at different rotational phases and has the advantage that the uncertainties in the parameters describing the global field structure can be directly related to the noise in the spectra. Its disadvantage lies in the necessary restriction to model fields which can be described by a sufficiently small number of parameters.

We assume fields which can be represented by centred or offset dipole and quadrupole components which need not be aligned with each other. The specific geometries tested here include a star with a single high-field spot and one with two spots separated by  $\sim 90^\circ$ . Our computer code allows us to calculate areal filling factor matrices analogous to ZEBRA plots, the resulting flux spectra, and the wavelength-dependent circular polarization for a given magnetic field model viewed at a number of rotational phases. We compare the results with the reference input (which are simulated data in this case) and determine the best-fit parameters using an evolutionary optimization strategy.

The present paper is arranged as follows. In Sect. 2.3 we describe the database of flux and polarization spectra computed for a wide range of field strengths, viewing angles, and effective temperatures. Section 2.4 describes the general design of the magnetic field models and Sect. 2.5 the construction of the integrated spectra from the database for a given model of the magnetic field. Section 2.6 explains the optimization code, describes the specific field models subjected to the reconstruction tests, and investigates the ability of the code to deduce the respective field parameters from the integrated flux and polarization spectra. Finally, the power and also the limitations of our approach are discussed in Sect. 2.7.

In forthcoming papers, we will analyse phase-resolved spectral flux and circular polarization data of MWDs obtained at the ESO VLT.

## 2.3 The database

### 2.3.1 Radiative transfer for magnetic white dwarfs

Our synthetic Zeeman spectra and wavelength-dependent polarization data are computed with the most recent version of the code developed by S. Jordan. The polarization originates from the different absorption coefficients  $\kappa_l$ ,  $\kappa_r$ , and  $\kappa_p$  for left- and right-handed circularly polarized light, and linearly polarized light travelling perpendicularly to the magnetic field, respectively, and is described by the four Stokes parameters  $I$ ,  $Q$ ,  $V$ , and  $U$ . The influence of the Faraday rotation and the Voigt effect is accounted for by the magneto-optical parameters  $\rho_R$  and  $\rho_W$ . The three radiative transport equations of Unno (1956) then expand into four equations (Beckers 1969; Hardorp et al. 1976) which can be solved by one of several different algorithms: (a) the method of Wickramasinghe & Martin (1979) assumes that the source function is linear in the optical depth and that between two successive depth points the Stokes parameters can be described by exponential functions; (b) direct Runge-Kutta integration; (c) accelerated  $\Lambda$  iterations (Takeda 1991); (d) an approximation for large Faraday rotation (Ramaty 1969); or (e) matrix exponential

solutions (Dittmann 1995). Intensive tests performed by H. Schmidt and S. Jordan in Kiel have demonstrated the numerical equivalence of these methods with high accuracy. For the present paper, we have calculated an extensive database of synthetic flux and circular polarization spectra using Ramaty’s approximation, which is always justified in white dwarf atmospheres, and is rather efficient with regard to CPU time.

The temperature and pressure structure of our atmospheres is taken from zero field LTE models (Koester et al. 1979). As a consequence, the magnetic pressure and magnetic blanketing (Jordan 1992) have been neglected. Convection is assumed to be suppressed by the field (Jordan 2001). For the line opacities, data from the Tübingen group (Forster et al. 1984; Rösner et al. 1984; Wunner et al. 1985) were used. Bound-free opacities were calculated using a modified approximation by Lamb & Sutherland (1974) which leads to small errors only (Jordan 1992; Merani et al. 1995; Jordan & Merani 1995) and saves an enormous amount of computing time. The approach described here was developed in two diploma theses (Euchner 1998; Rahn 1999) and was also implemented by Burleigh et al. (1999).

### 2.3.2 Database spectra

We computed a three-dimensional grid of Stokes  $I$  and  $V$  model spectra with the effective atmospheric temperature  $T$ , the magnetic field strength  $B$ , and the field direction  $\psi$  relative to the line of sight as the independent variables. We considered  $T = 8000$  K,  $9000$  K,  $10\,000$  K,  $11\,000$  K,  $12\,000$  K,  $13\,000$  K,  $15\,000$  K,  $17\,000$  K,  $20\,000$  K,  $25\,000$  K,  $30\,000$  K,  $40\,000$  K,  $B = 10$  MG to  $200$  MG in steps of  $1$  MG, and  $\psi = 0^\circ, 29^\circ, 41^\circ, 51^\circ, 60^\circ, 68^\circ, 76^\circ, 82^\circ, 90^\circ$ , i.e., equidistant in  $\cos \psi$ . This yields a database containing  $12 \times 191 \times 9 = 20\,628$  model spectra for  $I$  and  $V$  each. All spectra are calculated for a surface gravity of  $\log g = 8$ . Since we do not include the linear polarization, the field direction is sufficiently constrained by the total field strength and the longitudinal field component. As an example, Fig. 2.1 shows a section around  $H\alpha$  for a sample of database spectra with  $T = 15\,000$  K,  $B = 20$  MG and five angles of  $\psi$ , equally spaced in  $\cos \psi$ . A typical property of these Zeeman spectra is the weak angular dependence of Stokes  $I$ , except near  $0^\circ$  and  $90^\circ$ , and the more pronounced dependence of Stokes  $V$ . Somewhat simplified, Stokes  $I$  carries much of the information on the distribution of the absolute value of  $\vec{B}$  over the surface of the star, while Stokes  $V$  is needed to derive the distribution of the field directions.

If limb darkening is important the direction cosine  $\mu$  of the line of sight with respect to the vertical direction in the stellar atmosphere needs to be considered as a further parameter in the database. Hence, including a wavelength-dependent description of limb darkening requires an expansion of the number of model spectra in the database by a factor equal to the number of  $\mu$ -values considered. For the present calculations, we use a simple limb darkening law which is independent of wavelength and avoid this extension of the database (see Sect. 2.5.3 below).

## 2.4 Magnetic field geometry

A curl-free field which originates only from sources in the stellar interior can be described by a multipole expansion of the scalar magnetic potential, using spherical harmonics with coefficients  $l$  and  $m = 0, \dots, l$ , which describe the zonal and sectoral periodicity of the field, respectively (see, e.g., Langel 1987). The number of free parameters of the field geometry is  $l(l+2)$ , i.e.  $8$  (15) for

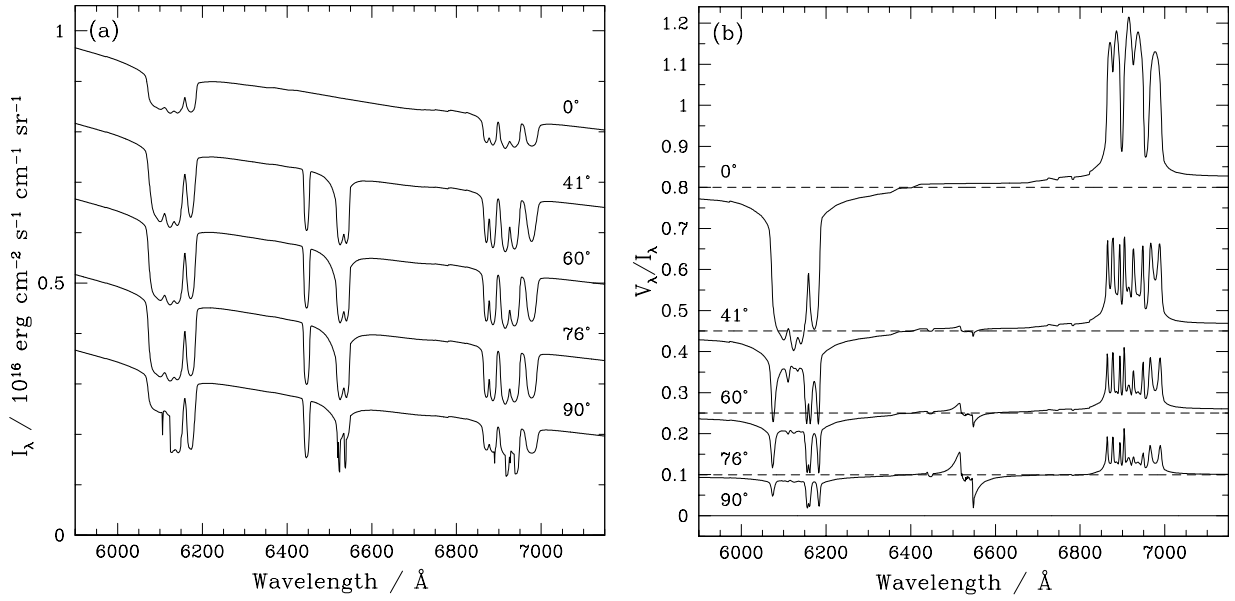


**Figure 2.1:** Examples of the database spectra for  $B = 20$  MG,  $T = 15\,000$  K, and five angles of  $\psi$  equally spaced in  $\cos \psi$  covering the H $\alpha$   $\sigma^-$ -,  $\pi$ -, and  $\sigma^+$ -components. **a)** Intensity, **b)** degree of circular polarization. The spectra are shifted vertically by arbitrary amounts to avoid overlap.

$l = 2$  (3). Defining the viewing geometry requires three additional parameters for the orientation of the rotation axis and the inclination.

The optimization procedure adopted for the present tests can handle only a limited number of multipole parameters and becomes inefficient already when the octupoles ( $l = 3$ ) are included. We have restricted the complexity of the field, therefore, by including only the two lowest zonal harmonics, commonly referred to as ‘dipole’ ( $l = 1$ ,  $m = 0$ ) and ‘quadrupole’ ( $l = 2$ ,  $m = 0$ ), allowing their axes to be inclined with respect to each other. We do not consider the  $m = 1$  and  $m = 2$  quadrupoles, but instead include a common offset of the dipole-quadrupole combination from the centre of the star. This hybrid model has ten free parameters: two polar field strengths; two angles each for the directions of the axes relative to the rotation axis; the three components of the offset; and the inclination, i.e. the angle between the rotation axis and the line of sight. An offset from the centre was included because of its popularity and simplicity (e.g., the Earth’s magnetic field is approximately that of a shifted dipole). The chosen field structure deliberately includes some very similar field geometries described by different sets of parameters: a combination of aligned dipole and quadrupole can be approximated by a shift of the dipole. At sufficient signal to noise, the reconstruction procedure can distinguish between such geometries, a result which is of interest by itself. While our hybrid model is useful for the tests performed in this paper, its limited complexity may not suffice for the interpretation of real, observed spectra.

We consider rotating MWDs viewed at an inclination  $i$  with respect to the rotation axis. Note that a fraction  $f = 0.5(1 - \sin i)$  of the stellar surface is permanently hidden from view and that phase-resolved Zeeman spectroscopy provides no information on the field on this hidden fraction of the surface. In order to save computing time, we restrict ourselves to simultaneously fitting flux and polarization spectra at four rotational phases,  $\phi = 0.0, 0.25, 0.5$ , and  $0.75$ . We avoid a

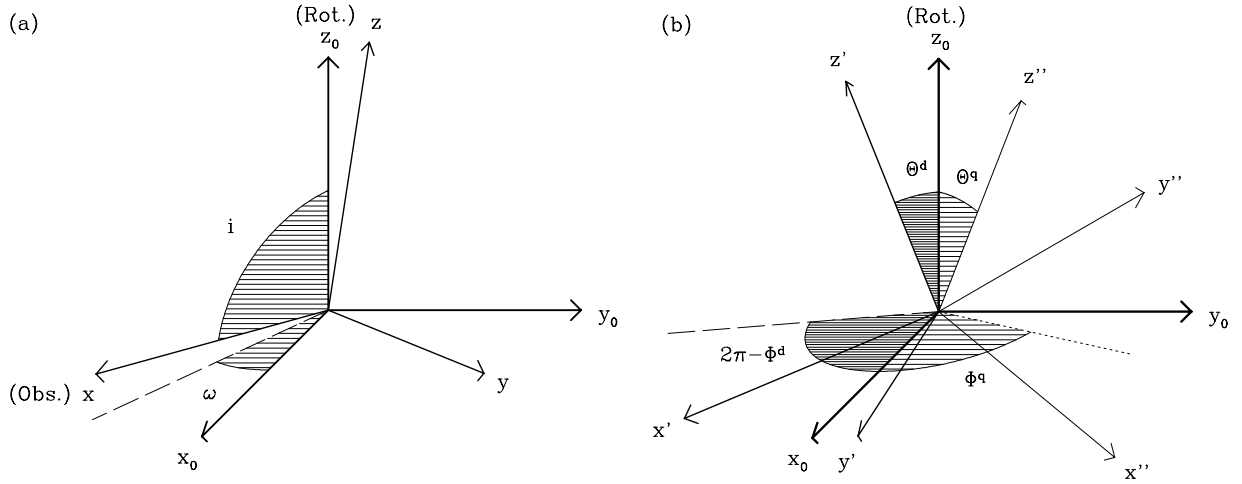


**Figure 2.2:** **a)** Rotational geometry of the MWD models. The  $x$ -axis points towards the observer, the  $z_0$ -axis marks the rotation axis. The dashed line marks the intersection of the  $x$ - $z$ -plane with the  $x_0$ - $y_0$ -plane.  $i$  denotes the inclination, and  $\omega$  the rotational phase angle. **b)** Magnetic geometry of the MWD models. The  $z'$ - and  $z''$ -axes mark the axes of symmetry for the dipole and quadrupole components. The lines of intersection of the  $x'$ - $z'$ -plane and the  $x''$ - $z''$ -plane with the  $x_0$ - $y_0$ -plane are given by the dashed and the dotted lines, respectively.

special geometry by choosing  $\phi = 0$  not to coincide with the nearest approach of one of the axes to the line of sight.

Since observational restrictions often prevent taking phase-resolved data, we also consider the amount of information which can be retrieved from a single flux and polarization spectrum or even a single flux spectrum only. In this case, the data provide information on the magnetic field structure only for one hemisphere of the star.

At any given phase  $\phi$ , the polarization depends on the components of the field transverse and parallel to the line of sight. In order to describe these components, we introduce four Cartesian coordinate systems (Figs. 2.2a and 2.2b): (i, ii) systems  $\Sigma'$  and  $\Sigma''$ , in which  $z'$  and  $z''$  describe the dipolar and quadrupolar axes of symmetry, respectively; (iii) the observer's system  $\Sigma$ , in which the  $x$ -axis points towards the observer and the  $z$ -axis lies in the plane defined by the  $x$ -axis and the rotation axis; and (iv) the auxiliary system  $\Sigma_0$  with  $z_0$  the direction of the rotation axis which defines the inclination angle  $i$ . The rotational phase angle  $\omega = 2\pi\phi$  is defined with respect to the direction of the  $x_0$ -axis which lies in the  $x$ - $z$ -plane for  $\omega = 0$ .

The components of the surface field  $\vec{B}(\vec{r}')$  of the centred dipole in system  $\Sigma'$  are

$$(B^d)_{x'} = 3B_{\text{pol}}^d x' z' / (2r'^5), \quad (2.1)$$

$$(B^d)_{y'} = 3B_{\text{pol}}^d y' z' / (2r'^5), \quad (2.2)$$

$$(B^d)_{z'} = B_{\text{pol}}^d (3z'^2 - r'^2) / (2r'^5), \quad (2.3)$$

with  $\vec{r}' = (x', y', z')$  and  $|\vec{r}'|^2 = r'^2 = x'^2 + y'^2 + z'^2$ . Correspondingly, the components of the centred quadrupole in  $\Sigma''$  are

$$(B^q)_{x''} = B_{\text{pol}}^q x''(5z''^2 - r''^2)/(2r''^7), \quad (2.4)$$

$$(B^q)_{y''} = B_{\text{pol}}^q y''(5z''^2 - r''^2)/(2r''^7), \quad (2.5)$$

$$(B^q)_{z''} = B_{\text{pol}}^q z''(5z''^2 - 3r''^2)/(2r''^7), \quad (2.6)$$

with  $\vec{r}'' = (x'', y'', z'')$  and  $|\vec{r}''|^2 = r''^2 = x''^2 + y''^2 + z''^2$ .  $\Sigma'$  and  $\Sigma''$  are tilted with respect to the rotation axis  $z_0$  by angles  $\Theta^d$  and  $\Theta^q$ , respectively. The azimuth angles of the tilt in  $\Sigma_0$  are  $\Phi^d$  and  $\Phi^q$  at phase  $\phi = 0$ . We apply the appropriate rotations and the translation to transform the fields into the observer's system  $\Sigma$ , add the dipole and quadrupole components, and obtain  $\vec{B}(\vec{r})$  for each surface element, with  $B_x = B_l = B \cos \psi$  the longitudinal component of the field.

The angle  $\delta$  between the dipole and quadrupole axes and the angles  $\eta^d$  and  $\eta^q$  between the line of sight at phase  $\phi$  and the dipole and quadrupole axis, respectively, are given by

$$\cos \delta = \cos \Theta^d \cos \Theta^q + \sin \Theta^d \sin \Theta^q \cos(\Phi^q - \Phi^d), \quad (2.7)$$

$$\cos \eta^d = \cos i \cos \Theta^d + \sin i \sin \Theta^d \cos(2\pi\phi + \Phi^d), \quad (2.8)$$

$$\cos \eta^q = \cos i \cos \Theta^q + \sin i \sin \Theta^q \cos(2\pi\phi + \Phi^q). \quad (2.9)$$

Our magnetic geometries were selected for the purpose of providing sufficient complexity for an effective test of our reconstruction routine. The offset  $\vec{r}_{\text{off}}'$  from the centre is a simple means of producing a substantial amount of azimuthal asymmetry if  $\vec{r}_{\text{off}}'$  is perpendicular to the dipole axis, while  $\vec{r}_{\text{off}}'$  parallel to the dipole axis allows to test the ability of the routine to distinguish between aligned centred dipole-quadrupole combinations and a shifted dipole.

## 2.5 Input spectra for the reconstruction procedure

### 2.5.1 Integration of the database models

We divide the spherical star into surface elements defined by equal steps in latitude and longitude. For given distributions of the magnetic field vector  $\vec{B}$  and the effective temperature  $T$  over the surface, let  $\alpha$  be the running index of the surface elements which are visible at a given rotational phase  $0 \leq \phi \leq 1$  and which have sizes  $A_\alpha$ , central field strengths  $B_\alpha$ , field directions  $\psi_\alpha$ , and direction cosines  $\mu_\alpha$ . The Stokes parameters  $\langle I_\lambda \rangle$  and  $\langle V_\lambda \rangle$  are then computed as weighted sums of the individual contributions corrected for limb darkening by a factor  $f_\alpha^{\text{LD}}$  (discussed below)

$$\begin{pmatrix} \langle I_\lambda \rangle \\ \langle V_\lambda \rangle \end{pmatrix}(\phi) = \sum_{\alpha(\phi)} A_\alpha \mu_\alpha f_\alpha^{\text{LD}} \begin{pmatrix} I_{\lambda,\alpha} \\ V_{\lambda,\alpha} \end{pmatrix}. \quad (2.10)$$

We represent the wavelength-dependent contributions  $I_{\lambda,\alpha}$  and  $V_{\lambda,\alpha}$  from surface element  $\alpha$  by appropriate interpolation in the database grids of the parameters  $T$ ,  $B$ , and  $\psi$ . For  $T$  and  $\psi$ , a bilinear interpolation suffices. For the field strength, we consider all spectra representative of the  $B$ -variation over the finite surface element. We found that a number of 900 surface elements per hemisphere is a good compromise between CPU time and needed accuracy. This number is sufficient to avoid spectral structure caused by the finite element size.

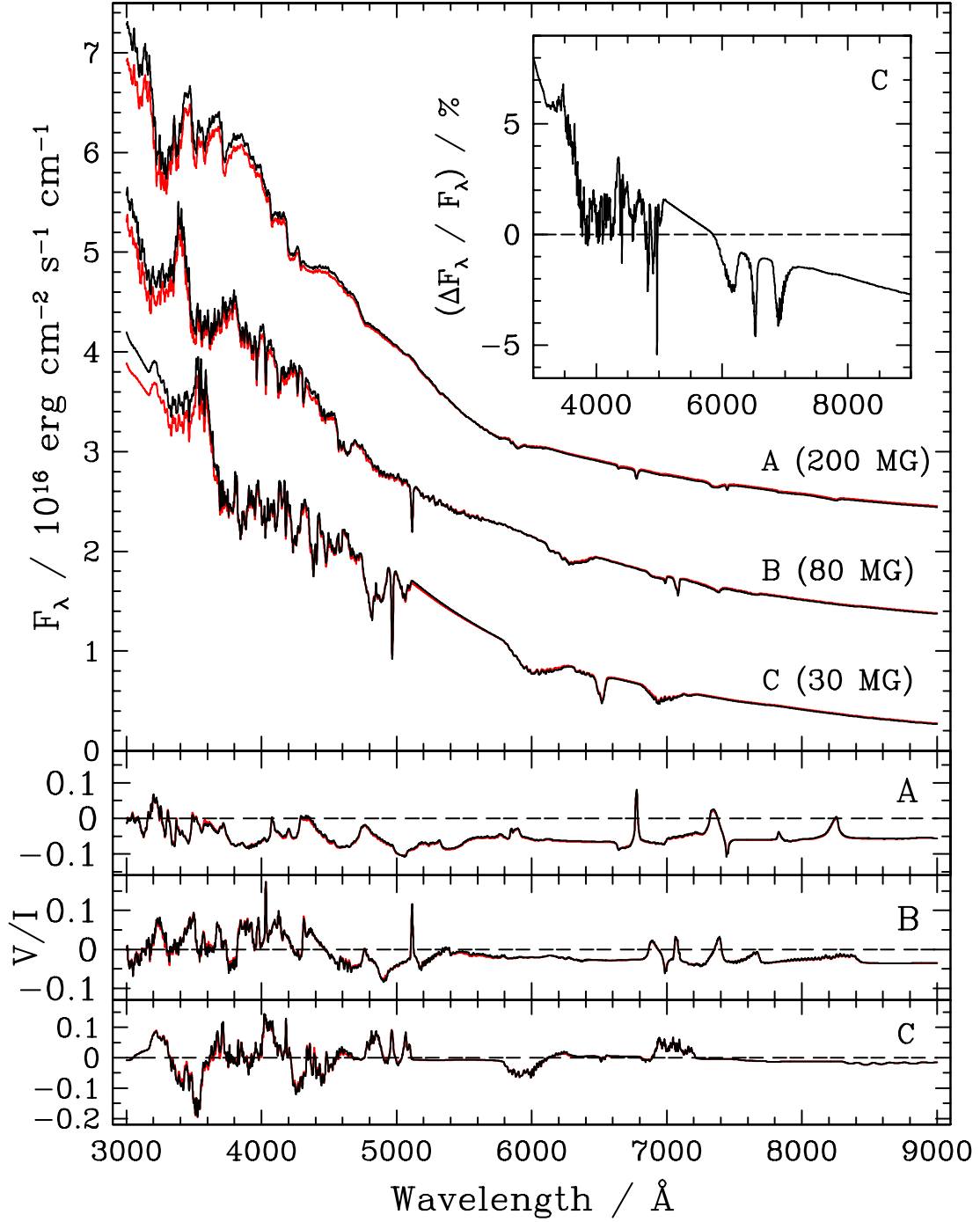


**Figure 2.3:** Spectral flux (*top*) and circular polarization (*bottom*) for centred dipoles viewed pole-on with polar field strengths of (A) 200 MG, (B) 80 MG, and (C) 30 MG for  $T = 15\,000$  K. The library-based spectra computed using a database of four  $\mu$ -values (red) are compared to those for  $\mu = 1$ , corrected with a mean limb darkening law (black). Spectra (A) and (B) have been shifted upwards to avoid overlap (1.1 flux units each). The insert shows the relative flux differences for the 30 MG case (C).

Our code can account for temperature variations over the surface of the white dwarf, but in this paper we consider only stars with uniform surface temperatures.

### 2.5.2 Relation to the observed flux

The flux observed from a star of radius  $R$  at distance  $d$  is

$$f_\lambda = F_\lambda R^2/d^2 \quad (2.11)$$

where  $F_\lambda = \pi \langle I_\lambda \rangle$  is a function of  $T$ , for a given magnetic field distribution. The interpretation of observed Zeeman spectra in terms of  $\langle I_\lambda \rangle$  and  $\langle V_\lambda \rangle$  involves  $T$  and  $R/d$  as fit parameters.

For the present tests,  $T$  and  $R/d$  are considered as fixed parameters and the quantities fitted by variation of the field parameters are  $F_\lambda$  and  $V/I = \langle V_\lambda \rangle / \langle I_\lambda \rangle$ .

### 2.5.3 Limb darkening

We have compared (i) the full radiative transfer for each surface element which accounts for the  $\mu$ -dependence and the variation of  $B$  across the element already in the atomic data, (ii) an interpolation between the spectra for discretized  $\mu$  and  $B$ , and (iii) the application of a wavelength-independent linear limb darkening law replacing the interpolation in  $\mu$ . Method (ii) uses spectra calculated for  $\mu = 0.1, 0.4, 0.7$ , and  $1.0$ . Method (iii) employs a linear law with coefficients which are valid for the visible wavelength range,

$$f_\alpha^{\text{LD}} = I_\lambda(\mu)/I_{\lambda,\mu=1} = 0.70 + 0.30\mu. \quad (2.12)$$

Test calculations for the three approaches (i) to (iii) were performed for centred dipoles viewed pole-on with polar field strengths of (A) 200 MG, (B) 80 MG, and (C) 30 MG. We found the differences between (i) and (ii) to be minute. Case (iii) differs by a wavelength-dependent factor which arises from the neglect of any wavelength dependence in the limb darkening approximation. Figure 2.3 shows the results for cases (ii) and (iii) at an effective temperature of 15 000 K. For all three field strengths, the spectra computed for case (iii) deviate by at most 5% from those of cases (i) and (ii). The insert shows that the absorption lines are about 2% deeper than for the correct treatment.

The simple limb darkening law of Eq. 2.12 is entirely acceptable for the present tests which interpret synthetic spectra with spectra of the same origin. The above comparison suggests, moreover, that a wavelength-independent linear limb darkening law may also be acceptable for the interpretation of observed optical Zeeman spectra of white dwarfs.

## 2.6 Reconstruction of the field geometry

In this Section, we describe a variety of magnetic field and viewing geometries and test the ability of our code to reconstruct their parameters from flux and circular polarization spectra at  $\phi = 0.0, 0.25, 0.5$ , and  $0.75$ . All calculations were performed for an effective temperature of 15 000 K. In order to simulate real data, noise was added to the input spectra at the four phases as



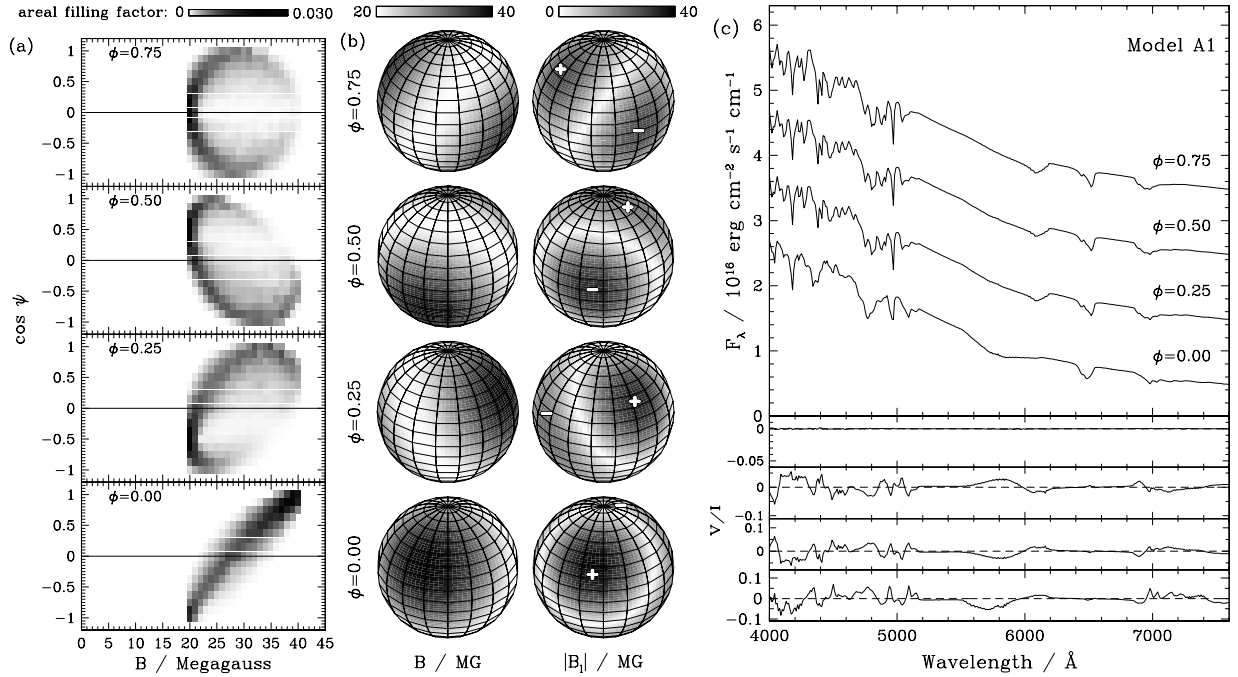


**Figure 2.4:** Model (A1), centred dipole viewed at  $i = 60^\circ$ : **a)**  $B$ - $\psi$  diagram, **b)** field strength and longitudinal component, **c)** flux and polarization spectra. The + and – symbols indicate the sign of the longitudinal component of the magnetic field. For clarity, the flux spectra at  $\phi = 0.25, 0.5$ , and  $0.75$  have been shifted upwards by one flux unit each.

described below. Because of the added noise, the reconstructed field is not necessarily identical to the input field. For the present tests, the wavelength range was restricted to  $4000 \leq \lambda \leq 7600 \text{ Å}$ , which contains the most important Balmer line components, and all spectra were rebinned into  $10 \text{ Å}$  bins, yielding 361 data pixels per spectrum, a total of 1444 pixels in the combined flux spectra at four rotational phases, and another 1444 pixels in the polarization spectra.

### 2.6.1 Magnetic field models

We define seven different magnetic field and viewing geometries against which we test our reconstruction code. The field configurations (A) to (F) are characterized by an increasing level of complexity. The geometrical and spectral properties of the models are summarized in Figs. 2.4–2.7. In each case, the centre panel shows the distributions of the total field strength  $B$  and of the absolute value of the longitudinal component  $B_l$  over the visible hemisphere at the four selected phases. The + and – symbols indicate the sign of the longitudinal component. The range of field strengths realized over the visible part of the surface of the white dwarf is given by the top grey bar. The left-hand panel shows the  $B$ - $\psi$  diagram, a greyscale plot of the frequency distribution of the magnetic field strength  $B$  and the direction cosine  $\cos \psi$ . The fractional contribution of each single database spectrum to the integrated spectrum is represented by the greyscale value of the corresponding pixel in the plot. This presentation includes the effects of pixel area, foreshortening, and limb darkening. The sum of all filling factors would be unity if limb darkening were



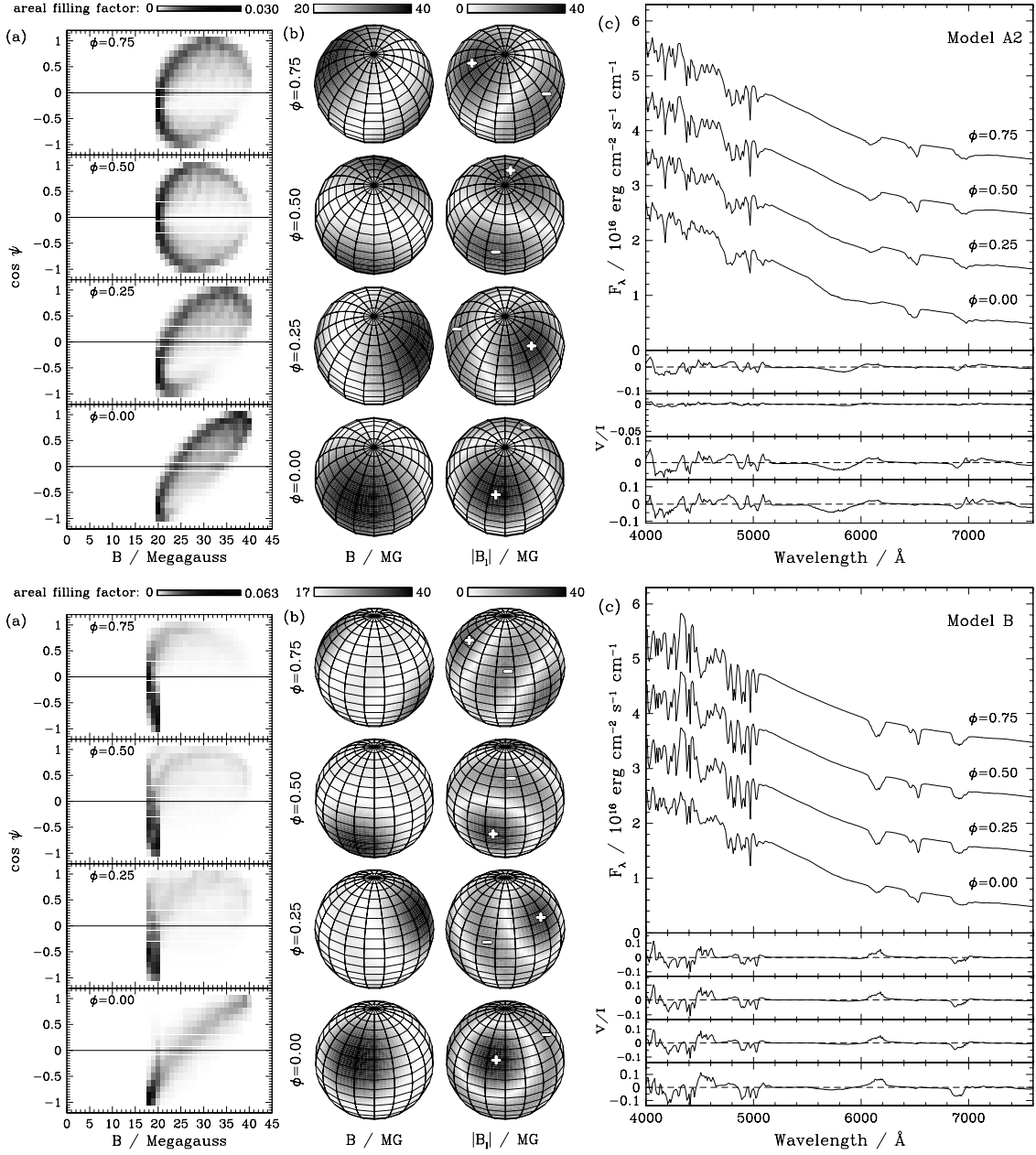


**Figure 2.5:** *Top:* Model (A2), centred dipole viewed at  $i = 30^\circ$ : **a)**  $B$ - $\psi$  diagram, **b)** field strength and longitudinal component, **c)** flux and polarization spectra. *Bottom:* Model (B), pure quadrupole viewed at  $i = 60^\circ$ : **a)**  $B$ - $\psi$  diagram, **b)** field strength and longitudinal component, **c)** flux and polarization spectra. See Fig. 2.4 for further explanation.

neglected, but falls below unity with limb darkening included. The  $B$ - $\psi$  diagrams are equivalent to the ZEBRA plots of Donati et al. (1994), except for the effect of limb darkening which was not included by these authors. The diagrams illustrate the change in the weighting of the two main database parameters,  $B$  and  $\psi$ , as the star rotates. The right-hand panel shows the resulting integrated flux and circular polarization spectra at the four rotational phases.

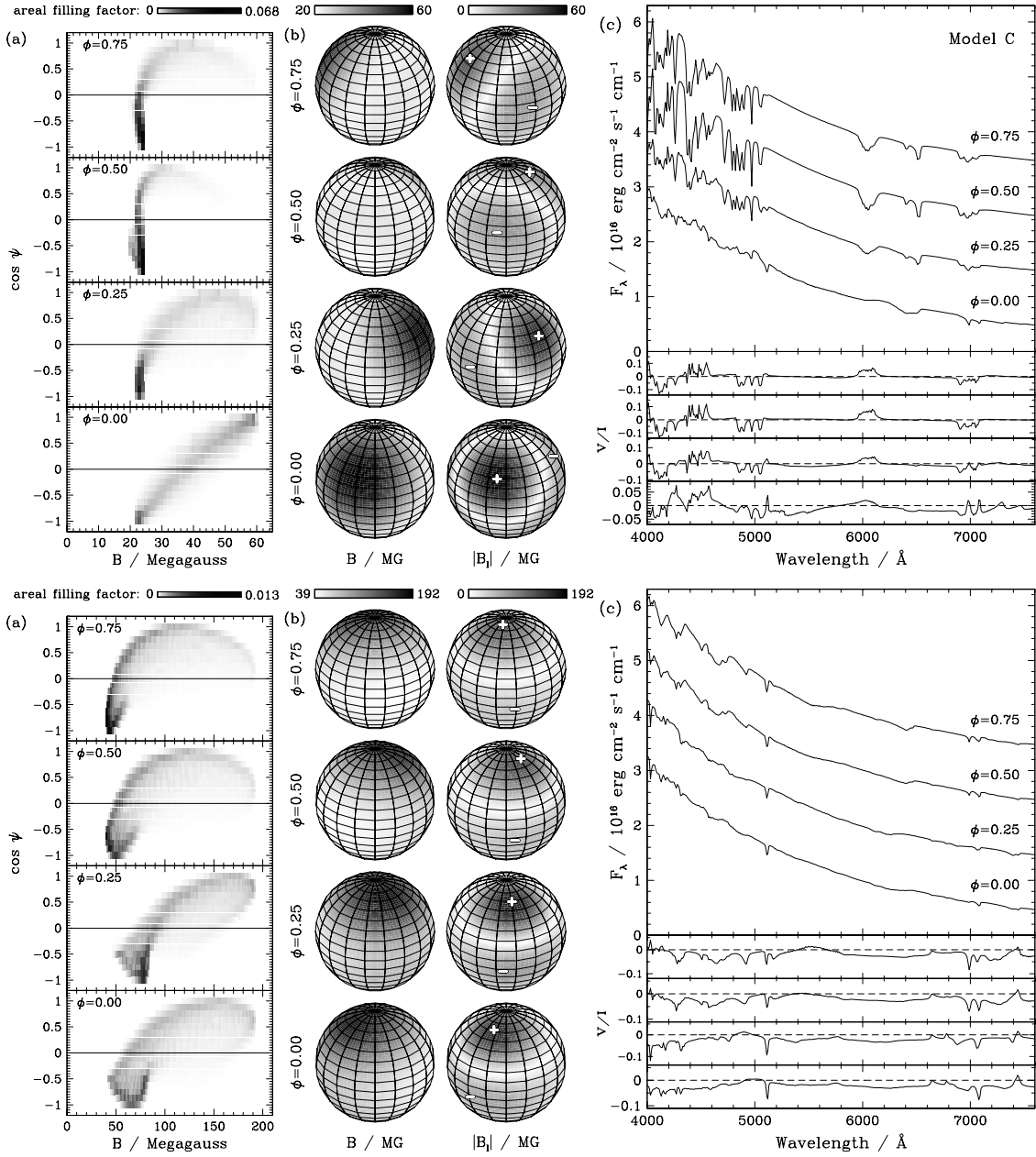


**Figure 2.6:** *Top:* Model (C), aligned dipole and quadrupole viewed at  $i = 60^\circ$ : **a)**  $B$ - $\psi$  diagram, **b)** field strength and longitudinal component, **c)** flux and polarization spectra. *Bottom:* Model (D), shifted high-field dipole viewed at  $i = 60^\circ$ : **a)**  $B$ - $\psi$  diagram, **b)** field strength and longitudinal component, **c)** flux and polarization spectra. See Fig. 2.4 for further explanation.

*Model (A1), centred dipole viewed at  $i = 60^\circ$ :* The polar field strength is  $B_{\text{pol}}^{\text{d}} = 40 \text{ MG}$  and the axis points towards  $(\Theta^{\text{d}}, \Phi^{\text{d}}) = (60^\circ, 340^\circ)$ . This oblique rotator model stands for a simple low-field geometry. The hidden fraction is only 7% of the white dwarf surface. The flux spectra in Fig. 2.4c are quite similar at  $\phi = 0.25, 0.5$ , and  $0.75$ , but the circular polarization spectra are

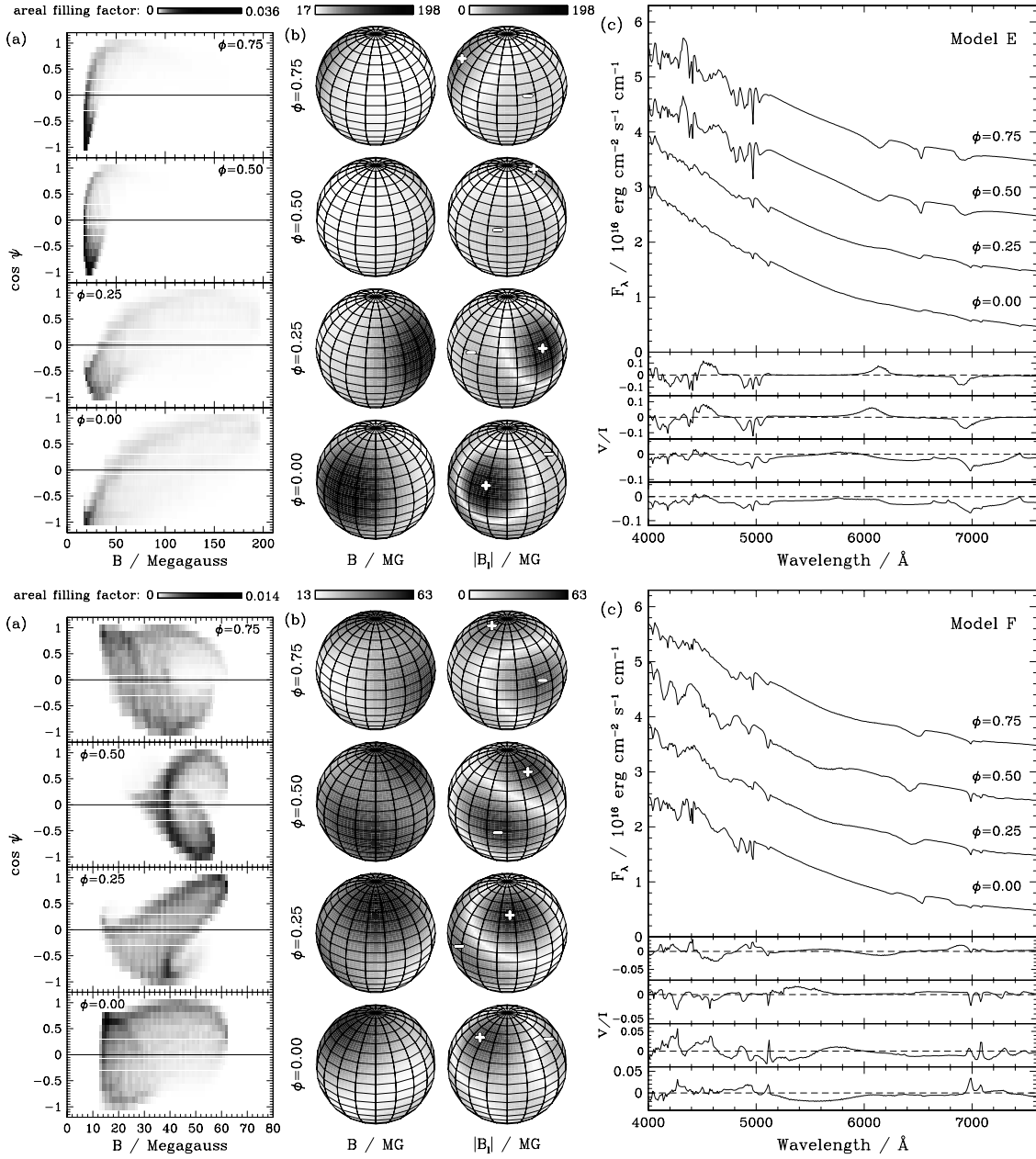


**Figure 2.7:** *Top:* Model (E), shifted dipole viewed at  $i = 60^\circ$ : **a)**  $B$ - $\psi$  diagram, **b)** field strength and longitudinal component, **c)** flux and polarization spectra. *Bottom:* Model (F), non-aligned dipole-quadrupole combination viewed at  $i = 60^\circ$ : **a)**  $B$ - $\psi$  diagram, **b)** field strength and longitudinal component, **c)** flux and polarization spectra. See Fig. 2.4 for further explanation.

not. The  $B$ - $\psi$  diagram looks different at  $\phi = 0$  and so does the flux spectrum. These differences suggest that full phase coverage is essential for a successful recovery of the field geometry.

*Model (A2), centred dipole viewed at  $i = 30^\circ$ :* The hidden fraction of the surface is now 25%. Otherwise, the properties of the model (Fig. 2.5, top) are similar to (A1). For the centred dipoles

of models (A1) and (A2), the circular polarization vanishes at a phase  $\phi_0$ , where the dipole axis is oriented perpendicular to the line of sight.

*Model (B), centred quadrupole viewed at  $i = 60^\circ$ :* The polar field strength is  $B_{\text{pol}}^q = 40$  MG and the axis points towards  $(\Theta^q, \Phi^q) = (60^\circ, 340^\circ)$ . Figure 2.5c (bottom) shows that there is little rotational variation. The flux spectra and the polarization vary little for  $\phi = 0.25, 0.5$ , and  $0.75$ , but differ at  $\phi = 0$ .

*Model (C), aligned centred dipole and quadrupole viewed at  $i = 60^\circ$ :* A quadrupole of  $B_{\text{pol}}^q = 20$  MG is added to a dipole of  $B_{\text{pol}}^d = 40$  MG with  $(\Theta^d, \Phi^d) = (\Theta^q, \Phi^q) = (60^\circ, 340^\circ)$ . The asymmetry introduced into the field geometry causes larger rotational variations in flux and polarization than for the pure dipole or quadrupole (Fig. 2.6c, top).

*Model (D), shifted high-field dipole viewed at  $i = 60^\circ$ :* The polar field strength is  $B_{\text{pol}}^d = 110$  MG, offset in all three coordinates by  $(x'_{\text{off}}, y'_{\text{off}}, z'_{\text{off}}) = (0.05, -0.10, 0.15)$ . The shift along the dipole axis increases the maximum field, and the sideways shift decreases the minimum field to the effect that  $B$  ranges from 39 to 192 MG. That is,  $B$  varies by a factor of five compared to a factor of two for the centred dipole. The high field causes the flux spectra to show substantially less structure than in the previous models, suggesting that a higher signal-to-noise ratio is needed for reconstruction (Fig. 2.6c, bottom). There is substantial variation in the circular polarization over the rotational period, however, which helps in the reconstruction.

*Model (E), shifted dipole viewed at  $i = 60^\circ$ :* This is an extremely off-centred dipole with  $B_{\text{pol}}^d = 58$  MG and  $(x'_{\text{off}}, y'_{\text{off}}, z'_{\text{off}}) = (0.15, -0.10, 0.30)$  which displays a variation of  $B$  over the surface by nearly a factor of 12. For one half of the rotational period, the high-field pole is in view, over the other half the field distribution is concentrated at low field strengths. Effectively, this represents a star with a low field of around 20 MG over most of the star and a spot in which the field rises to 198 MG. The circular polarization displays pronounced rotational structure (Fig. 2.7c, top).

*Model (F), non-aligned dipole-quadrupole combination viewed at  $i = 60^\circ$ :* This is the most complex field model featuring the superposition of a non-aligned dipole and quadrupole with equal polar field strengths of 40 MG. The polar directions,  $(\Theta^d, \Phi^d) = (60^\circ, 340^\circ)$  and  $(\Theta^q, \Phi^q) = (30^\circ, 250^\circ)$ , are separated by  $64^\circ$ . The field geometry features two high-field spots, an upper positive and a lower negative one, which are dominated by the quadrupole and the dipole, respectively, and are separated by  $\sim 90^\circ$  (Fig. 2.7, bottom).

An overview of the models (A)–(F) is given in Table 2.1 (Sect. 2.10). To illustrate the effects of noise in the spectra used in the reconstructions, we show in Fig. 2.8 the flux and polarization spectra of Model (A1) for  $\phi = 0$  at noise levels of  $S/N = 100$  and  $S/N = 20$ .

## 2.6.2 Optimization algorithm

Our spectral synthesis method is sufficiently fast to allow the use of hierarchical search strategies in the parameter space. We utilize the optimization routine *evoC* (Trint & Utecht 1994) that implements an evolutionary strategy algorithm (Rechenberg 1994), and has proven useful already in other astrophysical contexts (Gänsicke & Beuermann 1996; Gänsicke et al. 1998; Kube et al.

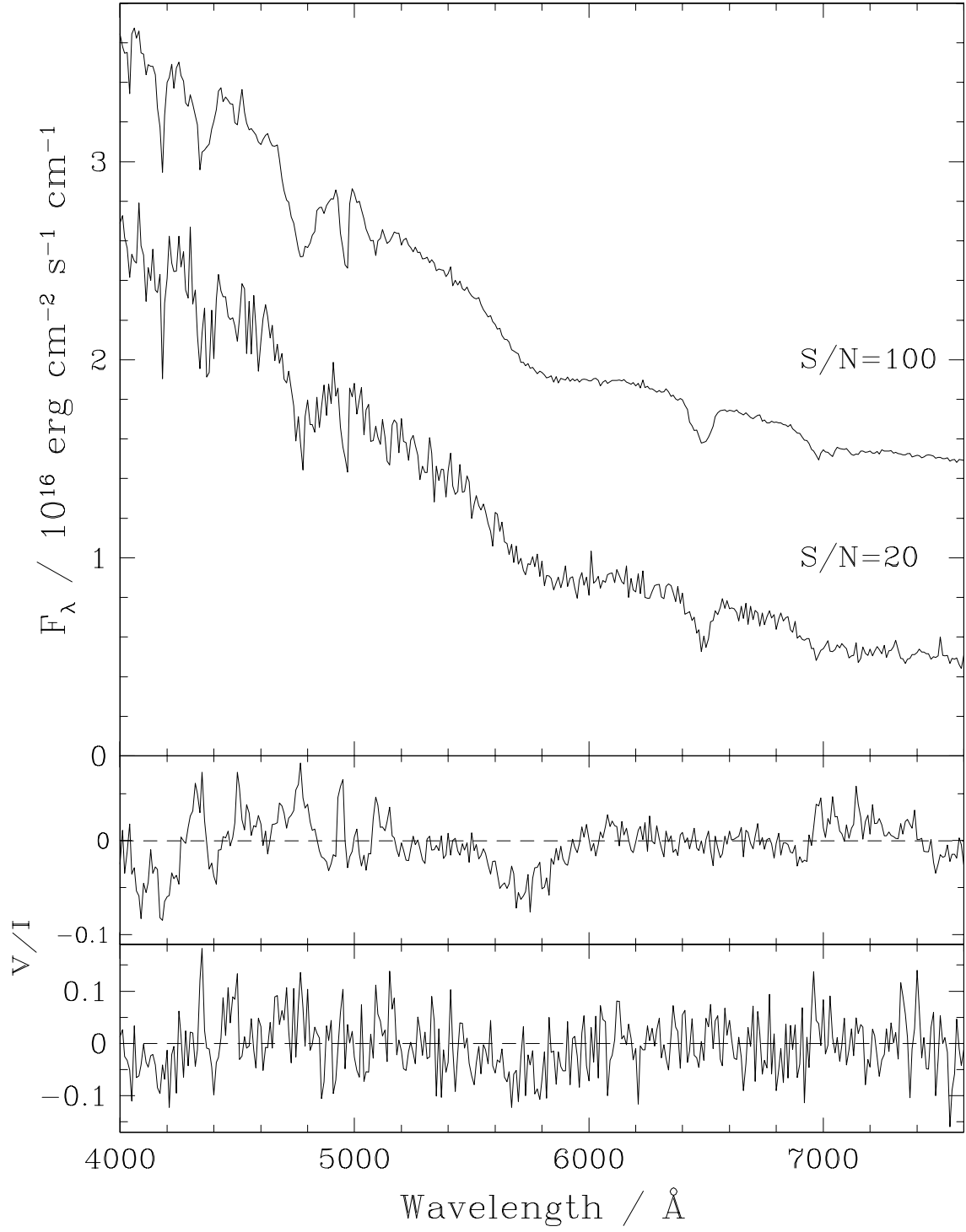


**Figure 2.8:** Examples of simulated spectra used as input to the reconstruction procedure. The  $\phi = 0$  spectrum of Model (A1) is shown with a signal-to-noise ratio  $S/N = 20$  and 100 (shifted upwards by one flux unit). *Top:* Flux spectra, *bottom:* circular polarization spectra.



2000). The task is to find a set  $\vec{a} = (a_1, \dots, a_M)$  of  $M$  free parameters that minimizes the classic penalty function

$$\chi_{\text{red}}^2(\vec{a}) = \frac{1}{N - M} \sum_{j=1}^N \frac{(f_j - s_j(\vec{a}))^2}{\sigma_j^2} \quad (2.13)$$

given the input data pixels  $f_j$ , the model data pixels  $s_j$ , and the standard deviations  $\sigma_j$ . Good fits require  $\chi_{\text{red}}^2 \approx 1$ . We have applied Gaussian noise to the input spectra to yield signal-to-noise ratios, corresponding to relative standard deviations in  $F_\lambda$  and absolute standard deviations in  $V/I$ , of 0.01 and 0.05, respectively. For fits to fluxes only,  $j$  runs up to  $N = 1444$ , and, for fits to both flux and polarization, up to  $N = 2888$ .

For each field model and each reconstruction with a certain set of free parameters, the **evoC** optimization process is run repeatedly, typically 6–20 times, starting each run with different, randomly chosen parameter values. Not all runs end up in the global minimum. A misguided run may be caught in a local minimum corresponding to an incorrect field configuration, which nevertheless has a Zeeman spectrum similar to the input one. We define a success rate of the optimization as the fractional number of runs which reach a best-fit  $\chi_{\text{red}}^2 < 2.0$  for  $S/N = 100$ , and  $\chi_{\text{red}}^2 < 1.1$  for  $S/N = 20$  (corresponding virtually always to the global minimum). As a last finish, we employ a downhill simplex algorithm (Nelder & Mead 1965; Press et al. 1992) on the run with the best  $\chi_{\text{red}}^2$ , which sometimes improves on the **evoC** solution.

In order to illustrate the problem associated with local minima in the  $\chi^2$ -landscape, we present in Fig. 2.9 a simple example of different field geometries which yield similar Zeeman spectra. The input geometry is the sum of a (non-rotating) dipole with  $B_{\text{pol}}^{\text{d}} = 40$  MG and an aligned quadrupole with  $B_{\text{pol}}^{\text{q}} = 20$  MG, viewed at  $i = 60^\circ$  (with  $\Theta^{\text{d}} = \Theta^{\text{q}} = \omega = 0^\circ$ , Fig. 2.2). The right-hand panel of Fig. 2.9 shows the corresponding flux and polarization spectra (lower curves). We add Gaussian noise of  $S/N = 100$  and compute flux and flux+polarization spectra covering a range of quadrupole parameters, with the dipole parameters and the inclination kept fixed. The quadrupole is allowed to vary in strength and orientation with  $\Theta^{\text{q}}$  free at  $\Phi^{\text{q}} = 90^\circ$ . For this choice of parameters, the quadrupole is perpendicular to the dipole and to the line of sight for  $\Theta^{\text{q}} = 90^\circ$ . The left-hand panel of Fig. 2.9 shows a contour plot of the  $\chi^2$ -landscape for the spectral flux in the  $B_{\text{pol}}^{\text{q}}, \Theta^{\text{q}}$ -plane. Besides the global minimum at the parameter values of the input configuration ( $B_{\text{pol}}^{\text{q}} = 20$  MG,  $\Theta^{\text{q}} = 0^\circ$ ), a second pronounced minimum appears at  $B_{\text{pol}}^{\text{q}} = -17$  MG and  $\Theta^{\text{q}} = 90^\circ$ , with the minus sign indicating a reversed polarity of the quadrupole. The flux and circular polarization spectra for this minimum are also shown in the right-hand panel of Fig. 2.9. At moderate noise levels, the flux and polarization spectra of these two diverse field geometries become indistinguishable and it is not surprising that the local minimum (in the upper left corner of the contour plot) persists if flux and circular polarization are considered together. The shallow local minimum at  $B_{\text{pol}}^{\text{q}} \simeq 33$  MG,  $\Theta^{\text{q}} \simeq 80^\circ$ , on the other hand, disappears if  $V/I$  is included in the computation of  $\chi_{\text{red}}^2$ . In the centre panels of Fig. 2.9, the  $B$ - $\psi$  diagrams for both configurations are shown. Both distributions are sufficiently similar if projected either on the  $B$ -axis or on the  $\cos \psi$ -axis to explain why the spectra are similar, but not identical.

Finally, we note that fitting the remaining parameters of the field model (like  $B_{\text{pol}}^{\text{d}}$ ) instead of keeping them fixed would cause the local minima to become even more pronounced. Increased noise also deepens the local minima relative to the global one. A local  $\chi^2$ -minimum is responsible for an incorrect, although not entirely dissimilar, reconstruction of Model F discussed below.

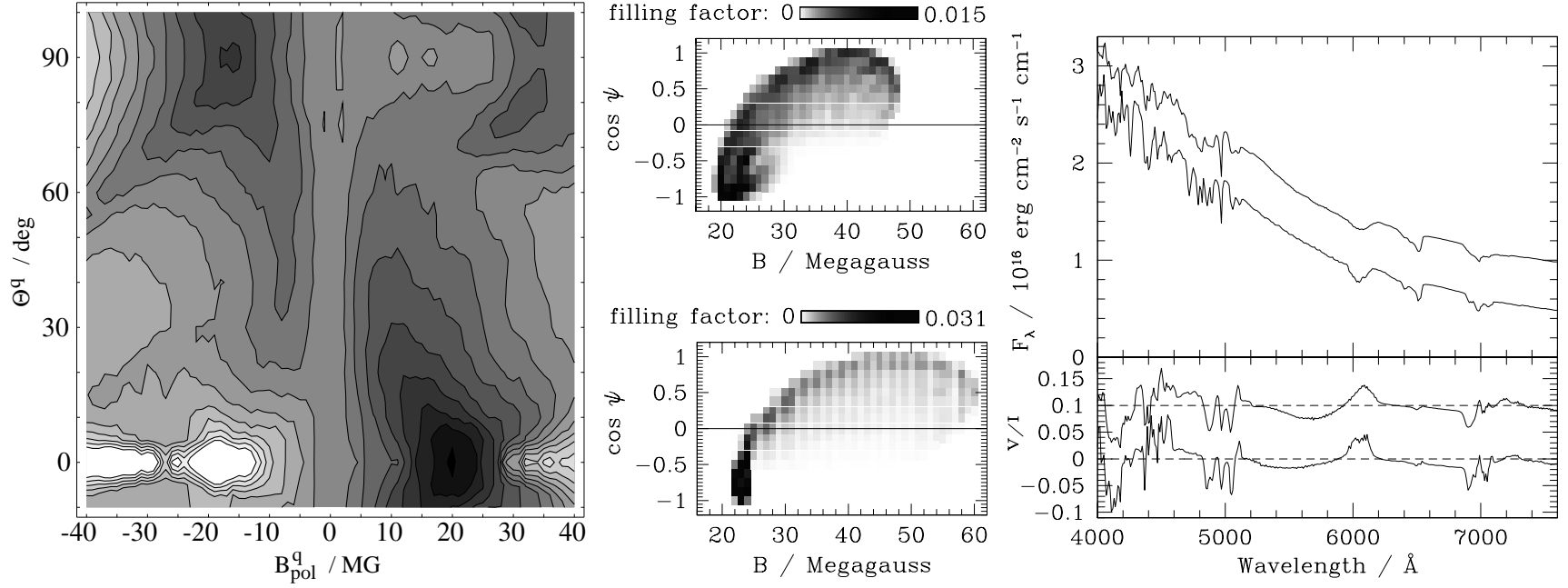


**Figure 2.9:** *Left panel:* Contour plot of the  $\chi^2$ -landscape for the spectral flux in the  $B_{\text{pol}}^q, \Theta^q$ -plane. The input configuration is given by  $B_{\text{pol}}^d = 40 \text{ MG}$ ,  $B_{\text{pol}}^q = 20 \text{ MG}$ , and  $\Theta^d = \Theta^q = 0^\circ$ . Darker shading corresponds to smaller values of  $\chi_{\text{red}}^2$ . *Centre panel:*  $B$ - $\psi$  diagrams of the field configurations corresponding to the local (*top*) and the global (*bottom*) minimum. *Right panel:* Flux and circular polarization spectra corresponding to the the global minimum (lower curves) and the local minimum in the upper left of the left panel (upper curves, shifted upwards by 0.5 units in flux and 0.1 units in polarization).

### 2.6.3 Reconstruction fits

#### General characteristics of the solutions

Depending on the complexity of the input field, we consider reconstructions which differ in the numbers of free parameters, ranging from the full set of ten down to seven (with the quadrupole component or the offset neglected). Some redundancy is allowed because a dipole offset along its axis can also be modelled, to first order, by an aligned centred dipole-quadrupole combination. With data of sufficient  $S/N$ , the reconstruction procedure can recognize such subtle differences.

As a general feature, the reconstructed global field is of relevance only for that part of the stellar surface which is visible during the observation (or covered by the synthetic input in this paper). This underlines the importance of phase-resolved observations which allow the determination of the inclination and, thereby, to estimate the occulted fraction of the surface.

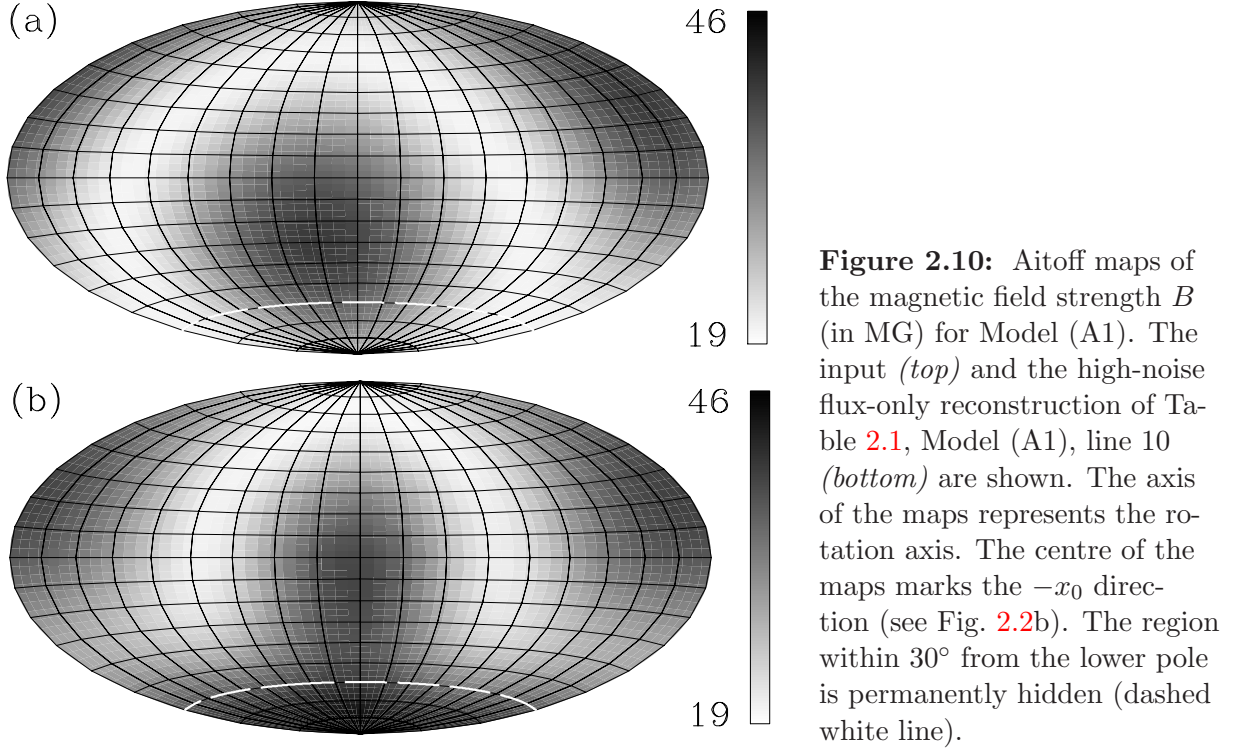
Spectrophotometry of high  $S/N$  is obtained more easily than spectropolarimetry of the same quality. The observer has to decide, therefore, whether a given amount of observing time is better spent on high-quality spectrophotometry or on circular spectropolarimetry of lower quality. In order to address such questions, we reconstructed all field geometries, using the spectral flux *and* the polarization, and using the spectral flux only. The flux-only reconstructions are successful in several cases, but the deviations from the input geometry tend to be larger, and an increased number of non-convergent runs suggest a less well-behaved  $\chi^2$ -landscape. We find that the circular polarization is not needed in simple cases, while its inclusion is extremely useful for the reconstruction of more complex fields.

#### Results for individual field geometries

In this Section, we present the results for the reconstructions of the input models (A) to (F), using the spectra at four rotational phases. All results are listed in Table 1. The column denoted ‘flag’ indicates whether the fit is to flux *and* polarization (fp) or to the flux only (f). The last column illustrates the convergence properties in the multidimensional parameter space, referred to as success rate above (number of successful runs vs. total number of runs).

*Model (A1), centred dipole viewed at  $i = 60^\circ$ :* The results in lines 1–4 assume  $B_{\text{pol}}^q = 0$ , those in lines 5–8 zero offset. All reconstructions are successful and reproduce the dipole field strength within 0.1 MG and the magnetic axis and the inclination with rms deviations of  $5^\circ$  and  $8^\circ$ , respectively. Not surprisingly, the accuracy of the reconstruction benefits from a high  $S/N$ , but is acceptable even for flux-only fits and a low  $S/N$  ratio. Note that errors in  $\Phi^d$  are irrelevant as long as  $\Theta^d$  matches closely. The same holds for  $\Phi^q$  and  $\Theta^q$  as long as  $B_{\text{pol}}^q$  is close to zero. If all parameters are included in the fit (lines 9 and 10), a quadrupole component usually appears which is largely compensated for by a shift in the dipole (plus quadrupole) to the effect that the net field is dipole-like again. The low-noise flux-and-polarization fit of line 9 is quite acceptable, while the high-noise flux-only fit of line 10 produces larger misfits in  $i$  and in the field geometry. Even the latter provides an acceptable reconstruction over the visible part of the surface, but deviates strongly from the input in the permanently occulted part. This result is due to the inclusion of a higher multipole component than present in the input. Figure 2.10 demonstrates this result.





*Model (A2), centred dipole viewed at  $i = 30^\circ$ :* The reconstructions are of a quality similar to that of model (A1). The permanently occulted fraction of the stellar surface, for which the reconstruction remains undefined, is now 25%.

*Models (B, C), pure quadrupole and aligned dipole-quadrupole viewed at  $i = 60^\circ$ :* The four reconstructions each use the same set of parameters as lines 5–8 of model (A1). The lack of a dipole component in (B) and the relative strength of the dipole and quadrupole components in (C) are recognized even in the flux-only and high-noise fits.

*Model (D), shifted high-field dipole viewed at  $i = 60^\circ$ :* The dipole is aligned with the rotation axis. Hence, the rotational modulation is caused by the off-centre shift. In spite of the weaker Zeeman structures (Fig. 2.6c, bottom), the configuration is recovered correctly if the search assumes a shifted dipole (lines 1–4). The absence of a quadrupole component is recognized in the low-noise flux-and-polarization fits (line 5), but less so in the high-noise flux-only fit (line 6). Interestingly, the offset is recognized correctly in both cases.

*Model (E), shifted dipole viewed at  $i = 60^\circ$ :* This is the model which features one high-field spot. If modelled as a shifted dipole, the parameters are recovered with high accuracy, even when the  $S/N$  is low and the polarization is disregarded (lines 1–4). Allowing for a quadrupole component leads to the usual compensatory effects (lines 5 and 6). The reconstruction is acceptable over the visible surface, and deviates only slightly from the input field in the occulted part.

*Model (F), non-aligned dipole-quadrupole combination viewed at  $i = 60^\circ$ :* All fits reproduce the general structure of the field with its two spots, separated by  $\sim 90^\circ$ , but only the fit using flux and polarization spectra at  $S/N = 100$  (line 1) correctly finds the axes of both, the dipole and the quadrupole components. Convergence problems, which arise when the polarization is disregarded (line 3), may be due to a more corrugated  $\chi^2$ -landscape compared with the fits including the

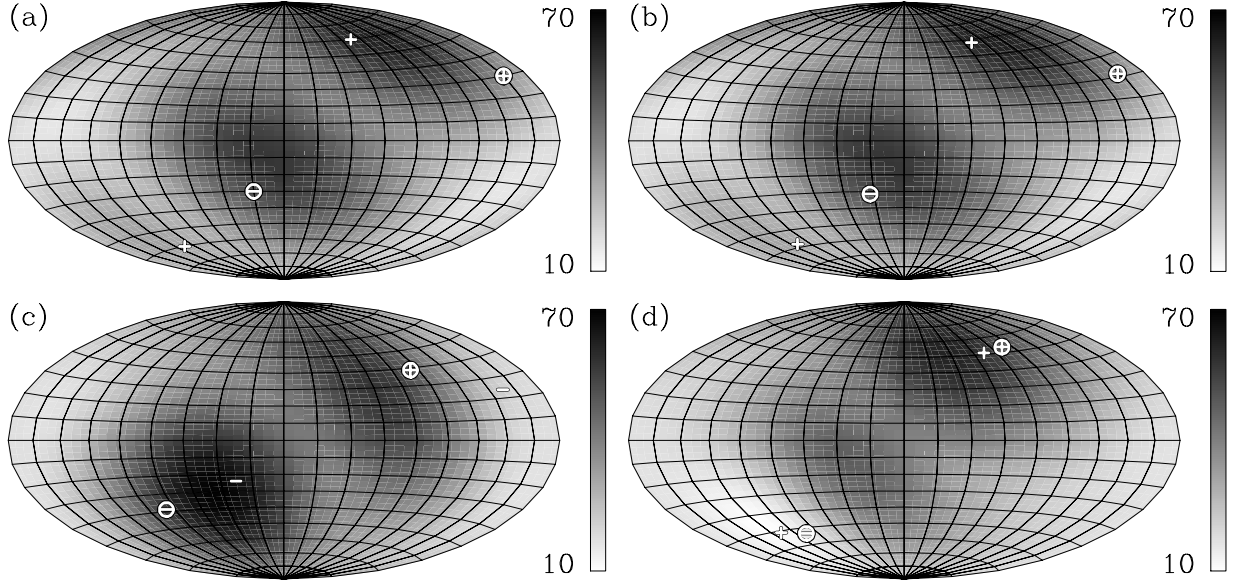


**Figure 2.11:** Aitoff maps of the field strength  $B$  (in MG) showing the results of reconstruction fits for the Model (F) field distribution (non-aligned dipole-quadrupole combination). The centre of the maps marks the  $-x_0$  direction. The axis of the quadrupole and the field direction at its poles is indicated by the  $+$  and  $-$  symbols, the axis of the dipole correspondingly by the circled  $+$  and  $-$  symbols (see text). **a)** Input field, **b)** low-noise flux-and-polarization reconstruction of Table 2.1, Model (F), line 1, **c)** high-noise flux-only reconstruction of line 4, and **d)** high-noise flux-only reconstruction of line 6.

polarization. Figure 2.11 provides an overview of the results for model (F). The input is depicted in Fig. 2.11a and the line-1 reconstruction in Fig. 2.11b. The high-noise flux-only fits of lines 4 and 6 (Figs. 2.11c and 2.11d) deviate in the strengths and orientations of the dipoles and quadrupoles. In Figs. 2.11a and 2.11b, the high-field spot on the northern (southern) hemisphere is dominated by the quadrupolar (dipolar) contribution. In Fig. 2.11c, the polarity of the quadrupole is reversed. Finally, in Fig. 2.11d, dipole and quadrupole are nearly aligned, but the spots are shifted due to the finite values of  $x'_{\text{off}}$  and  $y'_{\text{off}}$ . Nevertheless, these fits are not altogether wrong if only the two-spot structure is considered. They suggest that a low  $\chi^2_{\text{red}}$  does, in fact, indicate a representation which bears some similarity to the input field structure, even if the choice of multipoles differs from that of the input. Seemingly, better results cannot be expected given the high noise of these two fits.

In summary, the code is able to reconstruct the magnetic field geometries of the type discussed here from phase-resolved flux and polarization spectra of high  $S/N$ . Our experience is that the inclusion of more than four phases does not improve the fits substantially, which is understandable given the overlap in surface coverage. Naturally, the reconstruction becomes less perfect when the polarization information is excluded and the noise is increased. Leaving off the polarization also seems to create convergence problems. An important aspect is that phase-dependent spectra allow the inclination of the rotation axis to be determined along with the field geometry. The accuracy achieved ranges from a few degrees to about  $20^\circ$  depending on the quality of the spectra.

### Fits to a single spectrum

If only a single set of flux and polarization spectra or a single flux spectrum is available, information on the field distribution is reduced to the visible hemisphere. The location of the rotation axis remains unknown, and only the angle between the magnetic axis and the line of sight is constrained by the fit. We have performed similar tests as above to single sets of spectra and find that simple field geometries can still be recovered.

## 2.7 Discussion

We have presented a formalized approach to the interpretation of phase-resolved flux and circular polarization spectra of rotating magnetic white dwarfs (MWDs). Tomographically locating positions with a certain field strength  $\vec{B}$  on the surface of the star is hampered by the fact that only the self-eclipse of such a region manifests itself in flux spectra, while the positional information contributed by the rotation is obliterated by the Stark broadening.

### 2.7.1 Present approach

In our approach, we determine the parameters of a global field model directly by a least-squares fit to the spectral data. We caution that it is not *a priori* clear to what extent the global field can be constrained by such an approach, because the spectral information represents an average over the visible hemisphere at each phase. Our results demonstrate, however, that the phase-resolved Zeeman spectra contain enough information to allow the reconstruction of the field geometries considered by us. These involve combinations of dipoles and quadrupoles which are allowed to have different axes and to be shifted off-centre. The model contains up to ten free parameters and is sufficiently general to allow for rather complex surface field geometries featuring, e.g., a dominant single high-field spot, two spots separated by much less than  $180^\circ$ , or even a bipolar spot on an otherwise low-field star (not included in the models presented here). An advantage of our approach is that these fields automatically fulfil the requirement of being produced by sources inside the star. A disadvantage is the limitation in the number of free parameters.

In addition to the cases presented here, we have also attempted to reconstruct octupolar fields and were successful for aligned dipole-quadrupole-octupole combinations. However, if all multipole components with  $l = 3$  and  $m = 0, \dots, 3$  are included (15 parameters for the expansion, two angles describing the direction of the reference axis, and the inclination), the *evoC* minimization algorithm encounters convergence problems, caused by too large a number of free parameters.

Another important aspect is the level of the signal-to-noise ratio  $S/N$  required for a successful reconstruction of the field. The model atmospheres of hydrogen-rich MWDs are characterized by the rather broad and strong Zeeman-shifted Balmer lines which allow a field reconstruction already for  $S/N = 20$ – $100$ :  $S/N = 20$  is the lower limit, while there is little improvement for  $S/N > 100$ . For comparison, Zeeman-Doppler imaging of main sequence stars operates on much fainter metal lines and needs a much higher  $S/N$  (Brown et al. 1991). However, while Zeeman-Doppler imaging is performed over individual lines, the high field strengths of the MWDs require a fit over the whole visible wavelength range.

In the analysis of observed Zeeman spectra, one may encounter some problems which are absent in the present reconstruction of synthetic spectra. While the variation of the statistical noise amplitude with wavelength can be accounted for in the  $\chi^2$ -statistic (Eq. 2.13), systematic uncertainties between the observed and calculated spectra cannot: (i) errors in the theoretical database spectra; and (ii) errors in the flux calibration of the observed spectra. Errors of type (i) may prevent a satisfactory convergence of the fits and/or lead to incorrect values of the parameters describing the field. Our experience is that such errors are of minor importance, given the present state of the theory of radiative transfer in magnetic stellar atmospheres. Errors of type (ii) may affect the ability to recognize high field spots on stars with a predominantly moderate field. For example, in model (F) at phase  $\phi = 0.25$ , and similarly in other models, the  $H\alpha \sigma^-$  component consists of a shallow depression extending from 5000 to 6000 Å. An error in the flux calibration which happens to weaken or strengthen such a depression can lead to serious errors in the derived field distribution. A careful flux calibration is, therefore, of utmost importance.

### 2.7.2 Different optimization strategies

Should MWDs turn out to have field geometries which are more complex and require more free parameters than adopted by us, we may have to consider alternative optimization techniques. E.g., a genetic algorithm may be more robust than the `evoC` code and allow for a somewhat larger number of parameters. A full harmonic expansion with  $l \gg 2$  may become tractable if a regularization operator like MEM drives the solution towards low-order fields while permitting higher-order components to be used as necessary to fit the data.

### 2.7.3 The ZEBRA approach

The problem of retrieving the field structure of rotating MWDs has previously been studied by Donati et al. (1994) in what they called the ZEBRA approach. They used a maximum-entropy method to deduce the most likely two-dimensional frequency distribution  $f(B_t, B_l)$  of the transverse and longitudinal field components with respect to the line of sight separately for each rotational phase. The method has the obvious advantage that no *a priori* assumption is made about the global field structure. On the other hand, the interrelation between the overlapping field distributions at different rotational phases is not utilized and there is no prescription for the interpretation of such an interrelation in terms of a global field. Indeed, there is no guarantee of a physically meaningful reconstruction (e.g. sources only within the star leading to a curl-free field outside the star). Thus, the detailed structure and the physical characteristics of the global field remain undefined in the ZEBRA method in the present form (Donati et al. 1994).

If the underlying global field structure is sufficiently simple, it may be derived in a second step added to the ZEBRA method. In a first step, the best-fit ZEBRA diagrams (or  $B-\psi$  diagrams similar to ours) are determined using a MEM-type regularization scheme as suggested by Donati et al. (1994). In a second step, a parametrized global magnetic field model is then fitted to the phase-resolved ZEBRA diagrams. Since the second step would not involve the computation of spectra from the database, which is by far the most time-critical process in the present method, this two-step approach is probably advantageous with respect to CPU time. Without detailed tests, however, it is not clear whether this approach would be superior to directly fitting the Zeeman spectra.

### 2.7.4 A future approach

One may endeavour to relax the restrictions on the global field structure by parametrizing the surface field as  $(\vec{B}_1, \dots, \vec{B}_N)$  for a star with  $N$  surface elements and to impose a regularization scheme, e.g. MEM, to ensure the smoothness of the solution. The feasibility of such an approach, its convergence properties, and the interpretation of the derived field model would still have to be studied, however, as well as the demands on computation time given the formidable number of parameters.

## 2.8 Conclusion

We have described a method to reconstruct the field structure of magnetic white dwarfs which provides an internally consistent fit to spectropolarimetric data taken at different rotational phases in terms of a parametrized field model. We presently use dipoles and quadrupoles which are allowed to be shifted off-centre to increase the versatility of the model. An application to real data will be described elsewhere.

We do not know whether MWDs have the regular fields adopted here or possibly field structures as complex as spotted main sequence stars. Fortunately, there are several single white dwarfs with known rotational periods, and about 60 rotating MWDs in cataclysmic binaries, some of which are known to have fields which deviate from simple centred dipoles. The study of such systems using the present and similar techniques promises to increase our knowledge of the end-product of magnetic stellar evolution.

## 2.9 Acknowledgements

We thank Torsten Rahn for his contributions to the Kiel fraction of this program and Klaus Reinsch for fruitful discussions. FE acknowledges a grant from Graduiertenförderung des Landes Niedersachsen. This work was supported in part by BMBF/DLR grant 50 OR 9903 6.

## 2.10 Appendix: Table of best-fit parameters

(see next page)

**Table 2.1:** Reconstructed magnetic parameters for the configurations (A)–(F). Each model is introduced by a boldface line which lists the input parameters. The subsequent numbered lines represent the individual reconstructions. In the ‘flag’ column, ‘fp’ denotes simultaneous fits to flux and polarization spectra, ‘f’ fits to flux spectra only. The last column indicates the success rate of the convergence of the multidimensional parameter search. Note that for (B) and (C),  $\Theta^q = \Theta^d$  and  $\Phi^q = \Phi^d$ .

Model	$i$ (°)	$B_{\text{pol}}^d$ (MG)	$\Theta^d$ (°)	$\Phi^d$ (°)	$B_{\text{pol}}^q$ (MG)	$\Theta^q$ (°)	$\Phi^q$ (°)	$x'_{\text{off}}$ ( $R_{\text{WD}}$ )	$y'_{\text{off}}$ ( $R_{\text{WD}}$ )	$z'_{\text{off}}$ ( $R_{\text{WD}}$ )	$\chi_{\text{red}}^2$	$S/N$	flag	conv.
<i>(A1), centred dipole viewed at <math>i = 60^\circ</math>:</i>														
	<b>60.0</b>	<b>40.0</b>	<b>60.0</b>	<b>340.0</b>	<b>0.0</b>	<b>0.0</b>	<b>0.0</b>	<b>0.0</b>	<b>0.0</b>	<b>0.0</b>	–	–	–	–
1	54.4	40.0	64.2	339.0	–	–	–	–0.001	0.000	0.000	1.07	100	fp	2/10
2	47.0	40.2	62.8	350.6	–	–	–	0.000	–0.001	–0.003	1.01	20	fp	2/10
3	55.3	40.3	64.1	339.6	–	–	–	0.007	0.000	–0.002	1.03	100	f	1/20
4	60.0	40.1	61.0	346.4	–	–	–	0.002	–0.002	0.002	0.94	20	f	6/20
5	63.0	40.0	57.4	340.7	–0.1	85.7	95.7	–	–	–	0.99	100	fp	7/20
6	70.6	40.2	49.9	345.2	–1.3	5.2	241.5	–	–	–	1.01	20	fp	13/20
7	62.3	39.9	57.1	339.7	0.0	23.2	265.3	–	–	–	1.02	100	f	2/6
8	45.5	40.0	66.0	358.0	0.5	23.5	228.6	–	–	–	1.00	20	f	2/6
9	56.2	39.8	63.9	339.6	–2.6	31.6	249.0	–0.013	–0.007	–0.004	1.02	100	fp	1/20
10	45.7	39.7	56.2	353.4	–20.9	38.8	179.8	0.075	0.001	–0.085	1.02	20	f	3/20
<i>(A2), centred dipole viewed at <math>i = 30^\circ</math>:</i>														
	<b>30.0</b>	<b>40.0</b>	<b>60.0</b>	<b>340.0</b>	<b>0.0</b>	<b>0.0</b>	<b>0.0</b>	<b>0.0</b>	<b>0.0</b>	<b>0.0</b>	–	–	–	–
1	25.6	41.5	58.1	338.6	–	–	–	0.018	0.003	–0.014	1.03	100	fp	8/20
2	29.0	39.9	56.8	345.9	–	–	–	0.000	–0.006	–0.001	1.00	20	fp	9/20
3	29.5	39.5	59.0	339.6	–7.4	22.0	300.6	–0.068	–0.024	0.020	1.02	100	fp	1/20
<i>(B), centred quadrupole viewed at <math>i = 60^\circ</math>:</i>														
	<b>60.0</b>	<b>0.0</b>	<b>60.0</b>	<b>340.0</b>	<b>40.0</b>	<b>60.0</b>	<b>340.0</b>	<b>0.0</b>	<b>0.0</b>	<b>0.0</b>	–	–	–	–
1	56.7	0.1	63.0	339.9	40.0	63.0	339.9	–	–	–	0.97	100	fp	5/10
2	58.6	–0.8	60.8	331.2	40.0	60.8	331.2	–	–	–	1.02	20	fp	5/10
3	63.7	0.0	56.6	339.3	40.0	56.6	339.3	–	–	–	1.00	100	f	2/20
4	49.1	–0.4	61.7	346.2	40.0	61.7	346.2	–	–	–	1.00	20	f	5/20

*Continued on next page*



Model	$i$ ( $^{\circ}$ )	$B_{\text{pol}}^{\text{d}}$ (MG)	$\Theta^{\text{d}}$ ( $^{\circ}$ )	$\Phi^{\text{d}}$ ( $^{\circ}$ )	$B_{\text{pol}}^{\text{q}}$ (MG)	$\Theta^{\text{q}}$ ( $^{\circ}$ )	$\Phi^{\text{q}}$ ( $^{\circ}$ )	$x'_{\text{off}}$ ( $R_{\text{WD}}$ )	$y'_{\text{off}}$ ( $R_{\text{WD}}$ )	$z'_{\text{off}}$ ( $R_{\text{WD}}$ )	$\chi^2_{\text{red}}$	$S/N$	flag	conv.
<i>(C), aligned centred dipole and quadrupole viewed at <math>i = 60^{\circ}</math>:</i>														
	<b>60.0</b>	<b>40.0</b>	<b>60.0</b>	<b>340.0</b>	<b>20.0</b>	<b>60.0</b>	<b>340.0</b>	<b>0.0</b>	<b>0.0</b>	<b>0.0</b>	–	–	–	–
1	58.8	40.0	61.3	340.1	20.1	61.3	340.1	–	–	–	0.93	100	fp	5/10
2	55.2	40.1	64.4	334.7	19.8	64.4	334.7	–	–	–	1.00	20	fp	5/10
3	58.5	40.0	64.8	340.6	20.1	64.8	340.6	–	–	–	1.05	100	f	3/20
4	51.1	40.0	65.4	338.3	20.0	65.4	338.3	–	–	–	0.99	20	f	9/20
<i>(D), shifted high-field dipole viewed at <math>i = 60^{\circ}</math>:</i>														
	<b>60.0</b>	<b>110.0</b>	<b>0.0</b>	<b>0.0</b>	<b>0.0</b>	<b>0.0</b>	<b>0.0</b>	<b>0.05</b>	<b>−0.10</b>	<b>0.15</b>	–	–	–	–
1	60.1	110.1	0.3	150.2	–	–	–	0.051	−0.101	0.149	1.01	100	fp	1/10
2	61.1	109.7	0.3	223.6	–	–	–	0.056	−0.101	0.147	1.00	20	fp	3/10
3	59.8	109.9	0.1	218.1	–	–	–	0.050	−0.099	0.150	0.97	100	f	6/20
4	59.0	110.4	2.4	160.1	–	–	–	0.045	−0.105	0.154	1.05	20	f	1/20
5	59.8	109.8	0.1	90.1	−0.7	81.1	266.9	0.050	−0.100	0.150	0.99	100	fp	2/20
6	58.8	110.0	1.0	258.8	6.0	67.4	165.5	0.053	−0.105	0.162	0.93	20	f	18/20
<i>(E), shifted dipole viewed at <math>i = 60^{\circ}</math>:</i>														
	<b>60.0</b>	<b>58.0</b>	<b>60.0</b>	<b>340.0</b>	<b>0.0</b>	<b>0.0</b>	<b>0.0</b>	<b>0.15</b>	<b>−0.10</b>	<b>0.30</b>	–	–	–	–
1	63.9	57.4	59.1	338.3	–	–	–	0.15	−0.09	0.30	1.02	100	fp	4/10
2	60.4	57.9	60.9	337.0	–	–	–	0.16	−0.08	0.30	1.05	20	fp	3/10
3	60.2	57.6	60.3	340.3	–	–	–	0.15	−0.10	0.30	1.04	100	f	10/20
4	56.4	59.1	61.3	341.0	–	–	–	0.16	−0.10	0.30	0.97	20	f	15/20
5	60.1	59.5	63.9	340.5	15.2	73.1	334.1	0.13	−0.09	0.23	1.06	100	fp	5/20
6	54.4	62.9	61.3	355.2	26.7	51.7	256.3	0.22	−0.16	0.29	1.00	20	f	11/20
<i>(F), non-aligned dipole-quadrupole combination viewed at <math>i = 60^{\circ}</math>:</i>														
	<b>60.0</b>	<b>40.0</b>	<b>60.0</b>	<b>340.0</b>	<b>40.0</b>	<b>30.0</b>	<b>250.0</b>	<b>0.0</b>	<b>0.0</b>	<b>0.0</b>	–	–	–	–
1	58.8	40.3	58.5	337.3	39.8	31.9	247.3	–	–	–	1.01	100	fp	4/20
2	58.6	39.6	51.1	350.1	41.4	26.6	233.2	–	–	–	1.05	20	fp	10/20
3	66.2	39.9	68.0	347.4	40.4	26.7	270.0	–	–	–	1.13	100	f	5/20
4	43.3	49.1	51.2	273.6	−32.2	66.1	329.8	–	–	–	0.94	20	f	10/20
5	55.4	38.6	61.5	340.6	39.2	36.4	251.6	−0.022	0.009	−0.002	1.05	100	fp	1/20
6	46.7	39.4	36.7	269.9	30.4	39.0	248.8	0.051	0.078	−0.068	1.05	20	f	1/20





# 3 The quadrupole-dominated magnetic field of HE 1045–0908

F. EUCHNER<sup>1</sup>, K. REINSCH<sup>1</sup>, S. JORDAN<sup>2</sup>, K. BEUERMANN<sup>1</sup>, & B.T. GÄNSICKE<sup>3</sup>

<sup>1</sup> Institut für Astrophysik, Universität Göttingen, Friedrich-Hund-Platz 1, D-37077 Göttingen, Germany

<sup>2</sup> Astronomisches Rechen-Institut am ZAH, Mönchhofstr. 12–14, D-69120 Heidelberg, Germany

<sup>3</sup> Department of Physics, University of Warwick, Coventry CV4 7AL, UK

Based on observations collected at the European Southern Observatory, Paranal, Chile, under programme IDs 63.P-0003(A) and 64.P-0150(C).

Published in *Astronomy & Astrophysics* (2005) **442**, 651–660, [doi:10.1051/0004-6361:20053038](https://doi.org/10.1051/0004-6361:20053038)

### 3.1 Abstract

We report time-resolved optical flux and circular polarization spectroscopy of the magnetic DA white dwarf HE 1045–0908 obtained with FORS1 at the ESO VLT. Considering published results, we estimate a likely rotational period of  $P_{\text{rot}} \simeq 2.7$  h, but cannot exclude values as high as about 9 h. Our detailed Zeeman tomographic analysis reveals a field structure which is dominated by a quadrupole and contains additional dipole and octupole contributions, and which does not depend strongly on the assumed value of the period. A good fit to the Zeeman flux and polarization spectra is obtained if all field components are centred and inclinations of their magnetic axes with respect to each other are allowed for. The fit can be slightly improved if an offset from the centre of the star is included. The prevailing surface field strength is 16 MG, but values between 10 and  $\sim 75$  MG do occur. We derive an effective photospheric temperature of HE 1045–0908 of  $T_{\text{eff}} = 10\,000 \pm 1000$  K. The tomographic code makes use of an extensive database of pre-computed Zeeman spectra (Paper I, Chapter 2 of this thesis).

### 3.2 Introduction

Until a few years ago, magnetism among white dwarfs had been considered a rare phenomenon. A fraction of  $\sim 5\%$  of all known white dwarfs had been confirmed to be magnetic, with field strengths covering the range from  $\sim 30$  kG–1000 MG<sup>1</sup> (Wickramasinghe & Ferrario 2000). Presently, the low-field tail of the known field strength distribution is established by four objects in the kilogauss range ( $B \simeq 2$ –4 kG), which is the current detection limit for 8-m class telescopes (Fabrika & Valyavin 1999; Aznar Cuadrado et al. 2004). Recent studies suggest a much higher fractional incidence of magnetic white dwarfs (MWDs) of at least 10% for objects with surface fields exceeding 2 MG, and probably even more if low-field objects are included (Liebert et al. 2003; Schmidt et al. 2003; and references therein). While a high incidence is mainly found for cool, old white dwarfs, it is interesting to note that a high incidence of (weak) magnetic fields has also been detected in central stars of planetary nebulae, which are the direct progenitors of white dwarfs (Jordan et al. 2005), and in subdwarf B and O stars (O’Toole et al. 2005). There is strong evidence that the high-field magnetic white dwarfs have evolved from main-sequence Ap and Bp stars. Low- and intermediate-field objects are thought to originate either from late A stars that fall just above the mass limit below which fossil fields are destroyed in the pre-main-sequence phase (Tout et al. 2004), or from main sequence stars of still later spectral type.

Since there is no known mechanism to generate very strong magnetic fields in white dwarf interiors, the fields are believed to be fossil remnants of previous evolutionary stages (Braithwaite & Spruit 2004). Modelling of the field evolution showed that the characteristic time for Ohmic decay of the lowest poloidal multipole components is long compared with the white dwarf evolutionary timescale (Wendell et al. 1987; Cumming 2002). Higher-order modes do not necessarily decay faster, however, since they may be enhanced by nonlinear coupling by the Hall effect if internal toroidal fields are present (Muslimov et al. 1995). This is consistent with the finding of significant deviations from pure dipole configurations (Burleigh et al. 1999; Maxted et al. 2000; Reimers et al. 2004; Euchner et al. 2005a).

---

<sup>1</sup> 1 MG =  $10^6$  Gauss = 100 Tesla

**Table 3.1:** Dates and times for the spectropolarimetric observations of HE 1045–0908 obtained at the ESO VLT ( $t_{\text{exp}}$ : exposure time, n: number of exposures).

Object	Date	UT	$t_{\text{exp}}$ (min)	n
HE 1045–0908	1999/06/09	22:55–00:21	20	4
	1999/06/10	00:23–00:37	14	1
	1999/12/06	08:27–08:44	8	2

The present Zeeman tomographic analysis of phase-resolved circular spectropolarimetry of the white dwarf HE 1045–0908 provides further evidence for strongly non-dipolar fields. In the first paper of this series, we have demonstrated the ability of our code to derive the field configuration of rotating MWDs using phase-resolved flux and circular polarization spectra (Euchner et al. 2002, henceforth referred to as Paper I). In this and follow-up papers, we apply our code to individual objects.

HE 1045–0908 was discovered in the Hamburg/ESO objective prism survey for bright quasars (Wisotzki et al. 1996). Subsequent optical spectroscopy at the ESO 3.6-m telescope revealed a rich spectrum of Zeeman-split Balmer absorption lines and confirmed the object as a magnetic DA white dwarf (Reimers et al. 1994). By fitting theoretical Zeeman spectra for a centred dipole with a trial-and-error method, the best match was found by these authors for  $T_{\text{eff}} = 9200$  K,  $B_{\text{pol}}^{\text{d}} = 31$  MG, and a nearly equator-on view. Schmidt et al. (2001) subsequently obtained a sequence of five flux and circular polarization spectra of HE 1045–0908 over a duration of 1 h. The shape of the flux spectra in their observation sequence changes monotonically from almost vanishing to strong Zeeman features, whereas the variation in circular polarization is less pronounced. They estimated that the 1-h interval represented either one-quarter or one-half of a complete rotation cycle with a probable rotational period of  $P_{\text{rot}} \simeq 2\text{--}4$  h.

### 3.3 Observations

We obtained rotational-phase resolved circular spectropolarimetry for the magnetic DA white dwarf HE 1045–0908 with FORS1 at the ESO VLT UT1/Antu in June and December 1999. The dates and times of the observations as well as the number of exposures and exposure times are given in Table 3.1. The spectrograph was equipped with a thinned, anti-reflection coated  $2048 \times 2048$ -pixel Tektronix TK-2048EB4-1 CCD detector. For all observations, the GRIS\_300V+10 grism with order separation filter GG 375 covering the wavelength range  $\sim 3850\text{--}7500$  Å was used with a slit width of  $1''$  yielding a FWHM spectral resolution of  $13$  Å at  $5500$  Å. We were able to reach a signal-to-noise ratio  $S/N \simeq 100$  per resolution bin for the individual flux spectra. The instrument was operated in spectropolarimetric (PMOS) mode. The polarization optics consists of a Wollaston prism for beam separation and two superachromatic phase retarder plate mosaics. Since both plates cannot be used simultaneously, only the circular polarization has been recorded using the quarter wave plate. Spectra of the target star and comparison stars in the field have been obtained simultaneously by using the multi-object spectroscopy mode of FORS1. This allows us to derive individual correction functions for the

atmospheric absorption losses in the target spectra and to check for remnant instrumental polarization.

### 3.3.1 Data reduction

The observational data have been reduced according to standard procedures (bias, flat field, night sky subtraction, wavelength calibration, atmospheric extinction, flux calibration) using the context MOS of the ESO MIDAS package. In order to eliminate observational biases caused by Stokes parameter crosstalk, the wavelength-dependent degree of circular polarization  $V/I$  has been computed from two consecutive exposures recorded with the quarter wave retarder plate rotated by  $\pm 45^\circ$  according to

$$\frac{V}{I} = \frac{1}{2} \left[ \left( \frac{f^o - f^e}{f^o + f^e} \right)_{\theta=45^\circ} - \left( \frac{f^o - f^e}{f^o + f^e} \right)_{\theta=-45^\circ} \right], \quad (3.1)$$

where  $f^o$  denotes the ordinary and  $f^e$  the extraordinary beam (see the FORS User Manual for additional information, [Jehin et al. 2004](#)).

Since there were noticeable seeing variations during the observing run, we applied a correction for the flux loss due to the finite slit width of  $1''$ , using the measured FWHM of the object spectrum at  $5575 \text{ \AA}$  to estimate the effect of seeing and assuming a Gaussian intensity distribution across the slit.

### 3.3.2 Data analysis

In June 1999, we obtained a sequence of five exposures of HE 1045–0908 covering a time interval of 1.7 h, terminated by bad weather. This run yielded two independent circular polarization spectra (Eq. 3.1). In December 1999, another “snapshot” of two additional exposures was secured, yielding another polarization spectrum. All flux spectra are shown in Fig. 3.1 (left panel). The temporal change in the five June 1999 spectra is similar to that seen in the data set of [Schmidt et al. \(2001\)](#). In our data, the Zeeman features are most prominent at the beginning of the observations, in the [Schmidt et al.](#) data at the end. The features at the beginning and at the end of our run resemble those at the end and the beginning of the [Schmidt et al.](#) run, respectively, i.e. the variation of the Zeeman features in our run is reversed with respect to the [Schmidt et al.](#) data. Our isolated observation in December 1999 also fits into this pattern. We estimate that the phase of the strongest Zeeman features occurs between our spectra 1 and 2 in Fig. 3.1. Spectrum 5 approximately corresponds to the phase with the weakest Zeeman features. The implied rotational period is  $P_{\text{rot}} \simeq 2.7 \text{ h}$  if the combined [Schmidt et al.](#) and present observations cover a full rotational period. While the substantial variation of the Zeeman features suggests this might be true, there is unfortunately no proof of such a connection of the phase intervals covered in the separate observations. Alternatively, it is possible that the [Schmidt et al.](#) and our data do not cover a full rotational period and  $P_{\text{rot}} > 2.7 \text{ h}$ . We refer to the former as case (i) and to the latter as case (ii). In case (ii), there are several possibilities for the phase intervals covered by our and the [Schmidt et al.](#) data which we discuss below. The large variation in the strength of the Zeeman features cannot arise in too short a phase interval, however, and we find that for periods in excess of 9 h an acceptable solution is no longer obtained.

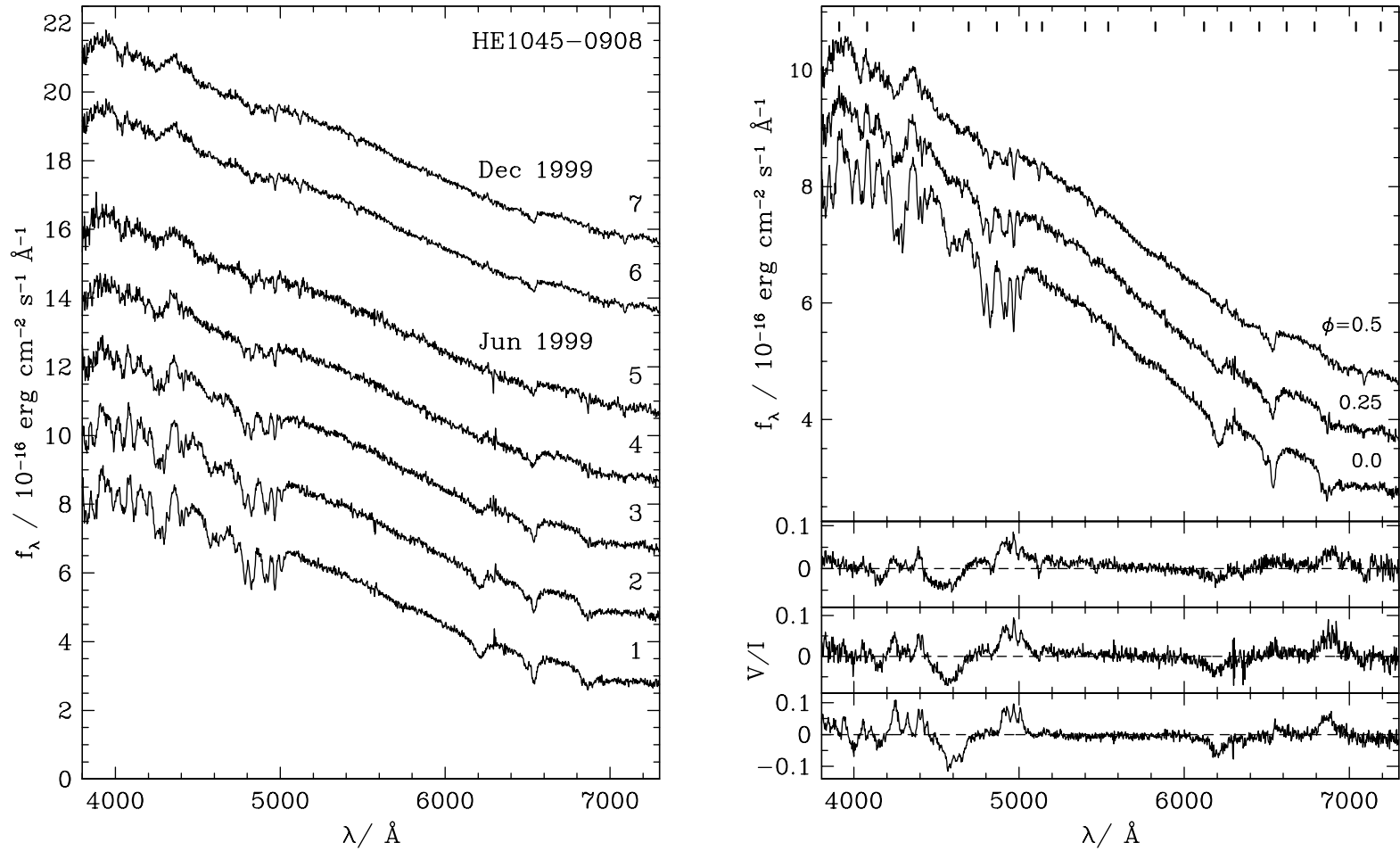


**Figure 3.1:** *Left panel:* Flux spectra of HE 1045–0908 from June 1999 (1–5) and December 1999 (6–7). Spectra 2–7 have been shifted upwards by two flux units each with an additional unit between spectra 5 and 6. *Right panel:* Combined flux and circular polarization spectra of HE 1045–0908 from the June/December 1999 observations, covering approximately one-half of the rotation cycle. These spectra, which have been collected into three phase bins, have been used as input spectra for the Zeeman tomographic procedure. For clarity, the uppermost two curves have been shifted upwards by one and two flux units, respectively. The quoted phases refer to case (i) with  $P_{\text{rot}} = 2.7$  h.

We follow the suggestion of [Schmidt et al.](#) of a period in the 2–4 h range and adopt 2.7 h as the preferred period, but report on the consequences of assuming a longer period below.

In preparation of the analysis, we note that the flux spectra of December 1999 (spectra 6 and 7 in Fig. 3.1) are very similar in shape to spectrum 5 and provide an additional independent circular polarization spectrum which connects in phase to the June 1999 run. We collect spectra 1/2, 3/4, and 6/7 into three flux and circular polarization rotational phase bins. For case (i) with  $P_{\text{rot}} \simeq 2.7$  h, these bins are approximately centred at rotational phases  $\phi = 0.0$ , 0.25, and 0.5, where  $\phi = 0$  refers to the phase of maximum strength of the Zeeman features in our June 1999 observation. The case (i) concatenation of our and the [Schmidt et al.](#) data requires that the flux spectrum at  $\phi = 0.75$  resembles that at  $\phi = 0.25$ . As a representative case (ii), we consider twice the rotational period and tentatively assign the three spectra to  $\phi = 0.0$ , 0.125, and 0.25. Our observations now cover a phase interval of only  $\Delta\phi = 0.25$ . Furthermore, we adopt  $P_{\text{rot}} \simeq 7.5$  h or even 11.3 h and assign the spectra to  $\phi = 0.0$ , 0.09, and 0.18 or 0.0, 0.06, and 0.12 with  $\Delta\phi = 0.18$  or 0.12, respectively.

In Fig. 3.1 (right panel), we present the three flux and circular polarization spectra which form the basis of our tomographic analysis. We refer to the mean of spectra 1 and 2 as “Zeeman maximum” ( $\phi = 0.0$ ) and to the mean of spectra 6 and 7 as “Zeeman minimum”, which corresponds to  $\phi = 0.5$  for case (i) and to the smaller values given above for case (ii).

### 3.4 Qualitative analysis of the magnetic field geometry

The rich Zeeman spectra of HE 1045–0908 allow us to obtain insight into the magnetic field geometry already by the simple means of comparing the spectra with the expected field-dependent wavelengths of the hydrogen transitions  $\lambda^{\text{H}}(B)$ , henceforth referred to as  $\lambda$ – $B$  curves ([Forster et al. 1984](#); [Rösner et al. 1984](#); [Wunner et al. 1985](#)). Fig. 3.2 shows the wavelength range around H $\beta$  of the Zeeman maximum spectrum ( $\phi = 0.0$ ) along with the  $\lambda$ – $B$  curves. Several transitions that can be immediately identified are marked by filled grey circles. This holds for the  $\sigma$  and  $\pi$  components in the flux spectrum and the  $\sigma$  components in the polarization spectrum, while the circular polarization of the  $\pi$  component vanishes, indicating a small viewing angle  $\psi$  between the magnetic field direction and the line of sight. The distribution of field strengths is sharply concentrated at  $\sim 16$  MG, as demonstrated also by the fair agreement between the observed and the model polarization spectrum shown at the very top of Fig. 3.2. This model spectrum is calculated for a *single* value  $B = 16$  MG,  $\psi = 29^\circ$ , and  $T_{\text{eff}} = 10\,000$  K. Hence, the field over the visible hemisphere at this phase is  $\sim 16$  MG and directed towards us.

The identification of Zeeman transitions is not as easily possible in the Zeeman minimum spectrum ( $\phi = 0.5$ ), and we do not show the corresponding attempt of a quick analysis. Four transitions can definitely be identified, however, from almost stationary parts of the  $\lambda$ – $B$  curves in H $\alpha$  and H $\beta$   $\sigma^+$ , and the corresponding field strengths span a range from 20 to 60 MG. This simple analysis proves already that the field strength over the stellar surface varies by about a factor four, excluding simple field configurations like a centred or a moderately offset dipole.

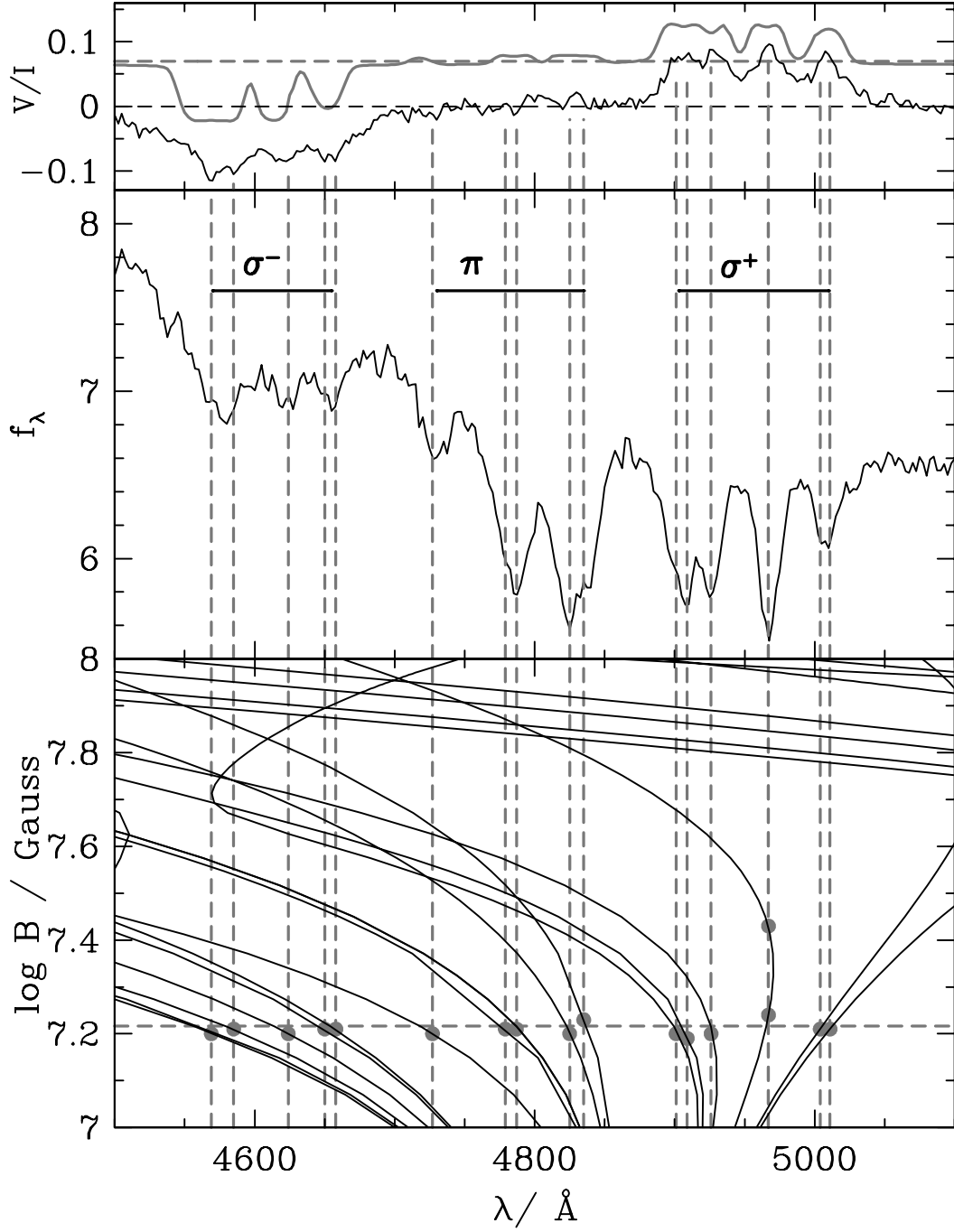


**Figure 3.2:** Zeeman maximum ( $\phi = 0$ ) flux  $f_\lambda$  (in units of  $10^{-16} \text{ erg cm}^{-2} \text{ s}^{-1} \text{ \AA}^{-1}$ ) and circular polarization  $V/I$  of HE 1045–0908, plotted along with the theoretically predicted field-dependent transition wavelengths ( $\lambda$ – $B$  curves) for Balmer absorption lines. The top panel also shows a theoretical circular polarization spectrum for a model atmosphere permeated by a homogeneous field of  $B = 16 \text{ MG}$  (shifted upwards by 0.07 units, with the horizontal dashed grey line denoting the zero polarization level). In the bottom panel, filled circles denote unambiguous identifications of transitions.



### 3.5 Zeeman tomography of the magnetic field

Theoretical wavelength-dependent Stokes  $I$  and  $V$  profiles of magnetized white dwarf atmospheres can be computed by solving the radiative transfer equations for given  $B$ ,  $\psi$ ,  $T_{\text{eff}}$ ,  $\log g$ , and the direction cosine  $\mu = \cos \vartheta$ , where  $\vartheta$  denotes the angle between the normal to the surface and the line of sight. A synthetic spectrum for a given magnetic topology can be described by a superposition of model spectra computed for different parameter values. Our three-dimensional grid of 46 800  $I$  and  $V$  model spectra covers 400  $B$  values (1–400 MG, in 1 MG steps), nine  $\psi$  values (equidistant in  $\cos \psi$ ), and 13 temperatures (8000–50 000 K) for fixed  $\log g = 8$  and  $\mu = 1$  (Paper I). This database allows fast computations of synthetic spectra for any given magnetic field configuration without the need to solve the radiative transfer equations each time. Limb darkening is accounted for in an approximate way by the linear interpolation

$$I_{\lambda}(\mu)/I_{\lambda,\mu=1} = a + b\mu. \quad (3.2)$$

For the sake of simplicity, the temperature- and wavelength-dependencies of  $a$  and  $b$  have been neglected (see the discussion in Paper I). Fitting the measured absolute flux distribution of HE 1045–0908 with model spectra computed using the full radiative transfer method, we find an effective temperature of  $T_{\text{eff}} = 10\,000 \pm 1000$  K. For this temperature, model spectra computed as a function of  $\mu$  suggest  $a = 0.53$  and  $b = 0.47$ . In the subsequent tomographic analysis, these values of  $T_{\text{eff}}$ ,  $a$ , and  $b$  were employed and kept constant.

Our Zeeman tomographic code requires an appropriate parametrization of the magnetic field, such that for every location  $\vec{r}$  on the stellar surface the magnetic field vector  $\vec{B}(\vec{r}, \vec{a})$  can be computed depending on a parameter vector  $\vec{a} = (a_1, \dots, a_M)$  of  $M$  free parameters describing the field geometry. Best-fit parameters are determined by minimizing a penalty function as a measure for the misfit between model and observation. For that purpose, we employed the C programming language library `evoC` by Trint & Utecht (1994)<sup>2</sup> which implements an evolutionary minimization strategy. The penalty function we used is the classical reduced  $\chi^2$

$$\chi_{\text{red}}^2(\vec{a}) = \frac{1}{N - M} \sum_{j=1}^N \frac{(f_j - s_j(\vec{a}))^2}{\sigma_j^2} \quad (3.3)$$

with the input data pixels  $f_j$ , the model data pixels  $s_j$ , and the standard deviations  $\sigma_j$ . We used 1321 pixels per phase for the individual flux and polarization spectra each, yielding  $N = 7926$  pixels in total ( $\lambda = 3900\text{--}7200$  Å,  $\Delta\lambda = 2.5$  Å). All phases have been equally weighted, and flux and circular polarization have also been given equal weight. In order to estimate the statistical noise, a Savitzky-Golay filter with a width of nine pixels (corresponding to 20 Å) has been applied to the observed spectra. Subsequently, the standard deviations  $\sigma_j$  entering Eq. (3.3) have been computed from the differences between the filtered and original spectra for wavelength intervals of 250 Å. The standard form of  $\chi_{\text{red}}^2$  was used as a suitable relative goodness-of-fit measure, but the unavoidable systematic differences between the observed and theoretical spectra prevent that anything near  $\chi_{\text{red}}^2 \simeq 1$  can be achieved.

In order to avoid that such systematic differences influence the analysis of the narrower Zeeman structures, we adjusted the model flux spectra to the observed spectra at a number of wavelengths

<sup>2</sup> <ftp://biobio.bionik.tu-berlin.de/pub/software/evoC/>



outside obvious Zeeman features. This procedure improves the fit of the flux spectra to the data but does not affect the polarization spectra. The wavelengths in question are marked by ticks at the top of Fig. 3.1 (right panel). Due to the finite exposure times, a model spectrum corresponding to a given observed spectrum should in principle be computed from several model spectra covering the respective phase interval. Our code is able to account for this “phase smearing” effect, but the need to compute the additional spectra slows down the minimization procedure so much that we decided against this approach. After having obtained best-fit parameters, we computed spectra including the effect and found no significant differences. The statistical errors of the best-fit parameters have been computed using the method described in Zhang et al. (1986).

Details of the radiative transfer calculations, the synthesis of model spectra, the geometry adopted for the description of the magnetic field configuration, and the fitting strategy are given in Paper I.

### 3.5.1 Field parametrization

In theoretical terms, a magnetic field of very general shape (with the constraints that it is curl-free and generated only in the stellar interior) can be described by expanding the scalar magnetic potential in spherical harmonics depending on the indices  $l$  and  $m$  for the degree and order of the expansion (Gauß 1838; Langel 1987). For each  $(l, m)$ -combination, two free parameters  $g_l^m$  and  $h_l^m$  are assigned, while only one parameter,  $g_l^0$ , describes the zonal components with  $m = 0$ . Thus, the number of free parameters for an expansion up to degree  $l$  is  $l(l + 2) = 15$  (24, 35) for  $l = 3$  (4, 5), increasing rapidly with the maximum degree  $l$ . Another property of multipole expansions is the dependence of the degree  $l$  required for an adequate description on the choice of the reference axis. Consider, e.g., a non-aligned superposition of a dipole and a quadrupole, which can be described exactly by four parameters ( $g_1^0, g_1^1, h_1^1, g_2^0$ ) if the reference axis coincides with the axis of symmetry of the quadrupole. If the reference axis points in a different direction, a finite  $l$  allows only an approximate description.

In order to ensure stable and fast convergence of our optimization scheme, it is necessary to minimize the number of free parameters. We adopt, therefore, a hybrid model which implements a superposition of zonal ( $m = 0$ ) harmonics only, disregarding the other tesseral components with  $m \neq 0$ . We allow for arbitrary tilt angles of the zonal components and also for off-centre shifts. With this configuration, it is possible to describe fairly complex geometries with fewer parameters than in the truncated multipole expansion which includes all tesseral components (see Paper I for a detailed description).

### 3.5.2 Results

#### Case (i): $P_{\text{rot}} = 2.7 \text{ h}$

In an attempt to find the best-fitting field geometry for HE 1045–0908, we considered a sequence of parametrizations with increasing complexity. In Fig. 3.3, we compare the observed circular polarization spectra at  $\phi = 0.0$  and  $\phi = 0.5$  with such a sequence of model spectra. The best-fit parameters and the corresponding  $\chi_{\text{red}}^2$  values are listed in Table 3.2 (Sect. 3.8). For the two simplest configurations (centred dipole and centred quadrupole) we obtained no satisfactory fit to the observations. This can be easily explained by the range of field strengths generated by

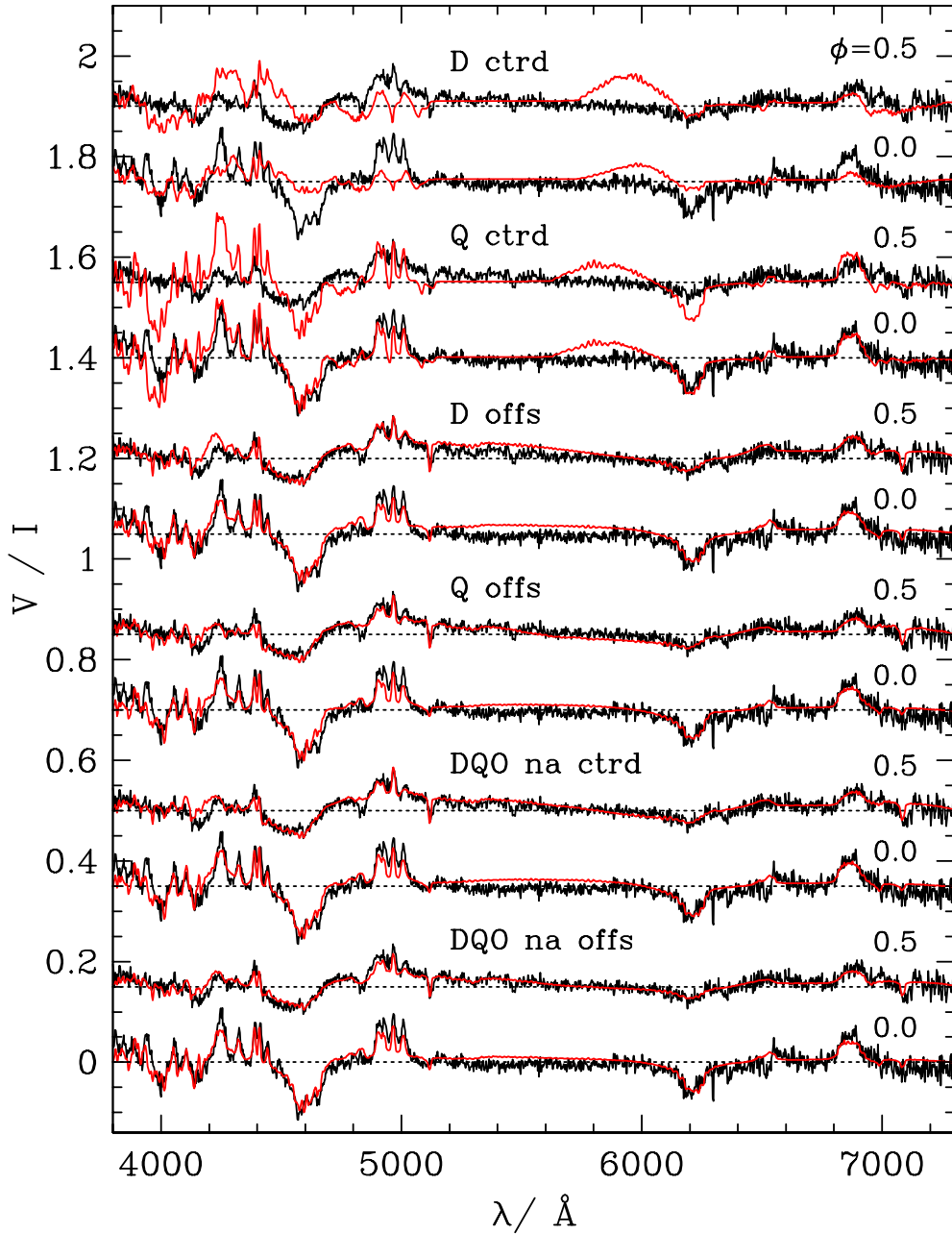


**Figure 3.3:** Observed circular polarization spectra for phases  $\phi = 0.0$  and  $0.5$  (black curves) and best-fit synthetic spectra (red curves) for different parametrizations of the magnetic field geometry. From top to bottom: centred dipole (D ctrd); centred quadrupole (Q ctrd); off-centred dipole (D offs); off-centred quadrupole (Q offs); centred, non-aligned combination of dipole, quadrupole, and octupole (DQO na ctrd); off-centred, non-aligned combination of dipole, quadrupole, and octupole (DQO na offs). All curves except for the bottom one have been shifted vertically by suitable amounts in  $V/I$ , with the horizontal dashed lines indicating the respective levels of zero polarization. The quoted phases refer to case (i) with  $P_{\text{rot}} = 2.7$  h.

these configurations, which is too large for  $\phi = 0.0$  and too small for  $\phi = 0.5$ . It is interesting to note that the centred dipole, which obviously provides the least adequate description, is the only configuration that yields an inclination of  $i > 20^\circ$ , whereas for all other configurations an inclination of  $i \simeq 10^\circ\text{--}20^\circ$  is obtained.

If an appropriate offset from the stellar centre is introduced for the dipole and quadrupole configurations, the possible range of surface field strengths increases and an extended region with a nearly constant field strength of 16 MG can be generated. Simultaneously, on the opposite stellar hemisphere a smaller high-field region with a steeper field gradient is created. As expected, the off-centred dipole and quadrupole models match the observations better than the centred configurations, with the quadrupole model fitting better than the dipole. In general, however, these simple models are unable to produce adequate fits to all details at all phases simultaneously.<sup>3</sup>

The next steps in complexity of the field configuration are represented by the superposition of dipole, quadrupole, and octupole and the introduction of an off-centre shift. Dipole-quadrupole combinations were not successful and the inclusion of the octupole is essential.

In a first attempt, we allowed the three individual components to be inclined with respect to each other, but not to be offset from the centre. The best fit with this field parametrization matches the observed flux and polarization spectra well for all rotational phases (Fig. 3.4, top panel). The frequency distribution of field strengths extends from 10 to 70 MG and peaks at 16 MG. At  $\phi = 0.0$  the distribution of field strengths drops steeply towards lower *and* higher fields, while at  $\phi = 0.5$  the peak is less pronounced and the distribution is much broader, implying that fields up to 70 MG contribute significantly to the Zeeman spectra. The  $B$ – $\psi$  diagram (Fig. 3.4, bottom left panel) shows that for the fields above 30 MG the sign of  $\cos \psi$  is reversed compared with the most frequent field of 16 MG. The picture of the field geometry (Fig. 3.4, bottom right panel) shows a high-field spot with  $B$  up to 70 MG superimposed on a low-field background of 10–20 MG. The field geometry on the visible part of the stellar surface is quadrupole-like with field lines leading from the high-field pole to an “equatorial” band. The field strengths and orientations of the individual components are given in line (5) of Table 3.2 (see also Eq. 7 in Paper I). With  $45 \pm 4$  MG, the quadrupole is more than three times as strong as the dipole with  $12 \pm 2$  MG. The three field components are more or less aligned, with the quadrupole inclined by only  $11^\circ$ , and the octupole by  $22^\circ$  with respect to the dipole. The slight inclinations of the individual components with respect to each other produce the required widening of the high-field spot. Basically, the field structure is that of an oblique rotator with an angle of  $\sim 40^\circ$  between field and rotational axes. The lower right panel, labelled  $R_{\max}/R_{\text{WD}}$ , indicates the maximum radial distances to which field lines extend in units of the white dwarf radius. Distances beyond  $10 R_{\text{WD}}$  (black) may denote open field lines<sup>4</sup>.

A slightly better fit is obtained if we allow for a common offset from the centre for all three components. As can be seen from Fig. 3.5 (top panel), this additional freedom leads, in particular, to improvements in the model circular polarization which we consider significant: (i) the steep rise at 4170–4220 Å for  $\phi = 0.0$ ; (ii) the dips at 4790–4870 Å and at 5300 Å for  $\phi = 0.5$ ; and (iii) the

<sup>3</sup> In Appendix A, plots of the best-fitting spectra,  $B$ – $\psi$  diagrams, and surface field distributions for the four models discussed so far are shown in Figs. A.1–A.4. These figures have not been included in the published version of this Chapter.

<sup>4</sup> This information may not be relevant for HE 1045–0908 but is useful in studies of accreting white dwarfs, because it allows the identification of regions that are potential foot points of field lines involved in channeled accretion. Accreting white dwarfs form a part of our programme and will be dealt with in forthcoming publications.

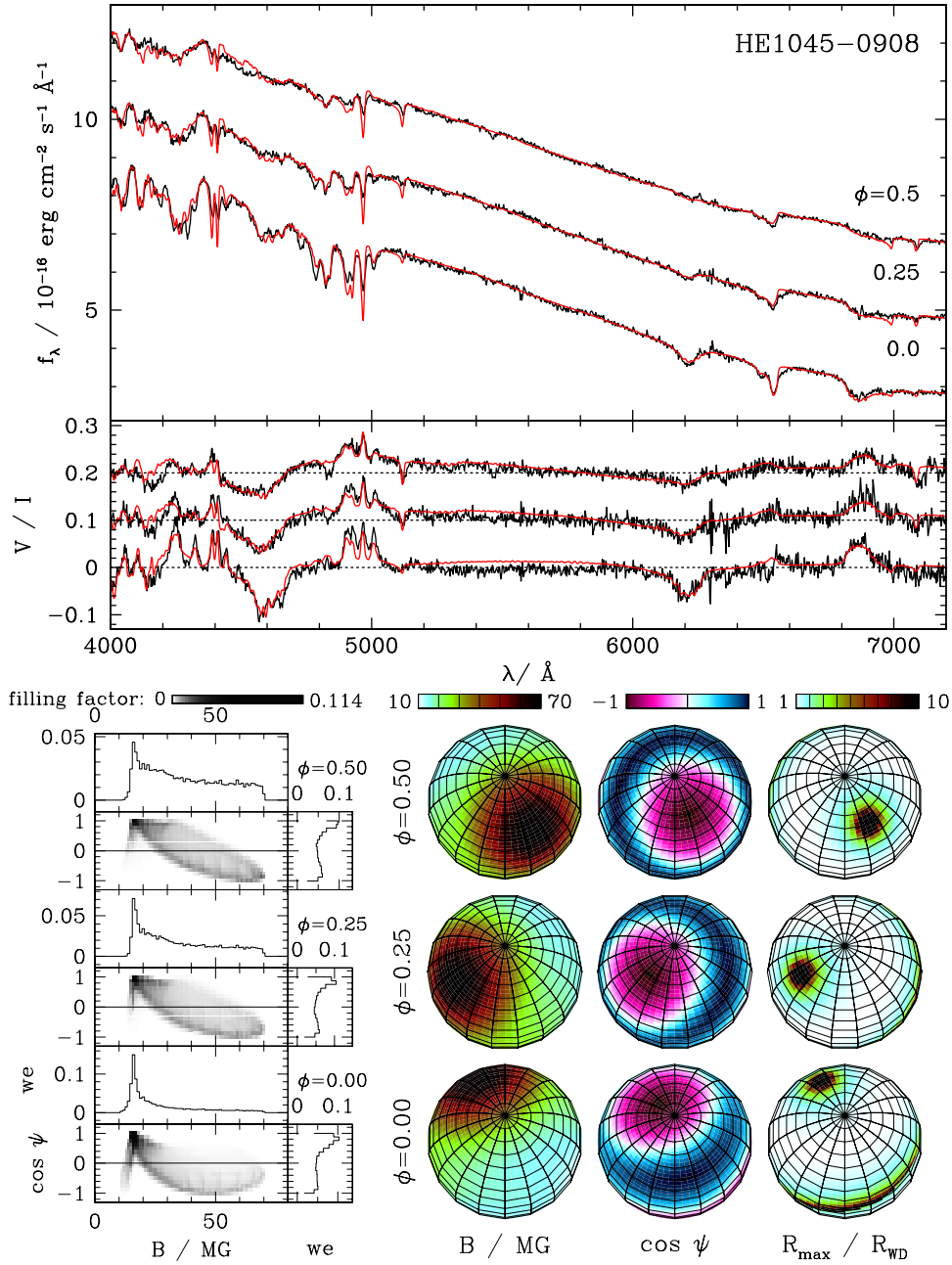


**Figure 3.4:** Zeeman tomographic analysis of the magnetic field configuration of HE 1045–0908 using a centred, non-aligned combination of dipole, quadrupole, and octupole. *Top:* Observed (black curves) and best-fit synthetic spectra (red curves). The uppermost two flux (circular polarization) spectra have been shifted for clarity by 2 and 4 (0.1 and 0.2) units in  $f_\lambda$  ( $V/I$ ). The quoted phases refer to case (i) with  $P_{\text{rot}} = 2.7 \text{ h}$ . *Bottom left:*  $B$ - $\psi$  diagram, *bottom right:* absolute value of the surface magnetic field, cosine of the angle  $\psi$  between the magnetic field direction and the line of sight, and maximum radial distance reached by field lines in units of the white dwarf radius (see text).

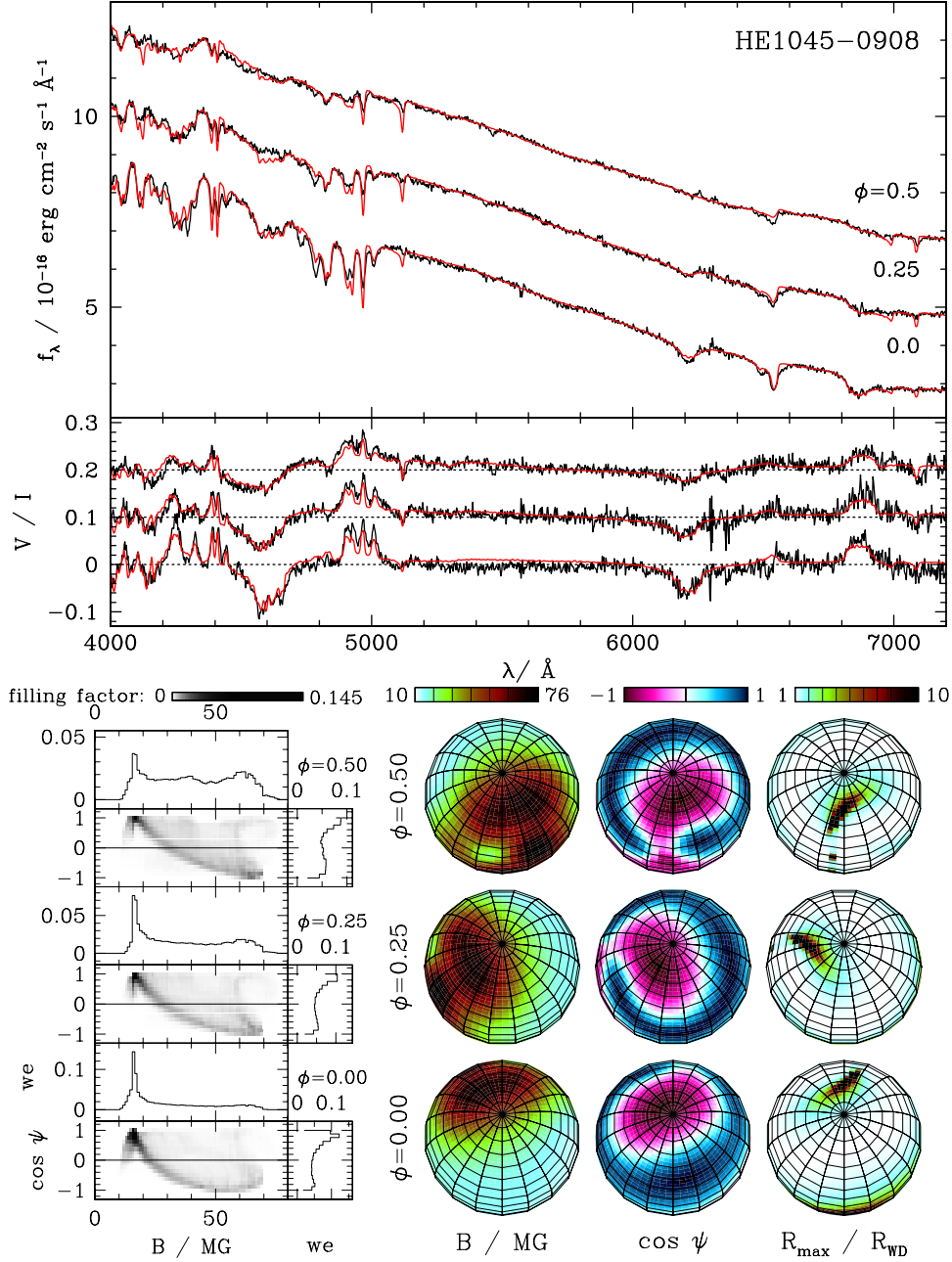


**Figure 3.5:** Zeeman tomographic analysis of the magnetic field configuration of HE 1045–0908 using an off-centred, non-aligned combination of dipole, quadrupole, and octupole. *Top:* Observed (black curves) and best-fit synthetic spectra (red curves). The uppermost two flux (circular polarization) spectra have been shifted for clarity by 2 and 4 (0.1 and 0.2) units in  $f_\lambda$  ( $V/I$ ). The quoted phases refer to case (i) with  $P_{\text{rot}} = 2.7 \text{ h}$ . *Bottom left:*  $B$ - $\psi$  diagram, *bottom right:* absolute value of the surface magnetic field, cosine of the angle  $\psi$  between the magnetic field direction and the line of sight, and maximum radial distance reached by field lines in units of the white dwarf radius (see text).



continuum polarization in the 5200–6000 Å range. The  $B$ – $\psi$  diagram (Fig. 3.5, bottom left panel) shows an enhanced frequency of field strengths around 60 MG for all three phases. For  $\phi = 0.5$  we still see a pronounced decrease at 70 MG, but, in contrast to the previous configuration, there is a small but significant contribution from fields of 70–76 MG and the same direction as the prevailing field of 16 MG. Figure 3.5 (bottom right panel) shows a field geometry that is similar from a global point of view, but reveals a more complex structure in the high-field region with two separate areas of opposite field direction. This general similarity is produced, however, by an arrangement of the field components which is entirely different from the previous model (see also the examples given in Paper I). The quadrupole is now inclined by  $90^\circ$  with respect to the dipole, and the octupole is not far from orthogonal to both. The shift is primarily in the direction of the dipole ( $z'$ -axis), and, hence, shifts the quadrupole perpendicularly to its axis. The field strengths quoted for this model in line (6) of Table 3.2 refer to the unshifted components, and the final surface values can be calculated with some additional algebra. The shape of the region with field lines reaching beyond  $10 R_{\text{WD}}$  (black) has changed from a circular spot to an arc. Field lines still end in a linearly extended region just visible at the stellar limb for  $\phi = 0.0$ .

All models in lines (1) through (6) of Table 3.2 have the property that the  $\phi = 0.75$  Zeeman spectra resemble those at  $\phi = 0.25$ , as required by the proposed concatenation of the Schmidt et al. and our data. Hence, although the Schmidt et al. data have not been used in the fit, they are approximately reproduced by the models.

The models of lines (5) and (6) of Table 3.2 with 9 and 12 free field parameters, respectively, fit better than the 17-parameter model of the full multipole expansion up to  $l = 3$  presented in a preliminary report (Euchner et al. 2005a). While this multipole expansion provides a better fit, e. g., to the 5200–6000 Å continuum polarization at  $\phi = 0.0$ , it fails more seriously in other places. It seems that the choice of the arbitrarily oriented zonal components is more adequate for the case of HE 1045–0908. Models with about a dozen free magnetic field parameters represent the present limit of our code at which a stable convergence to the global minimum in the  $\chi^2$  landscape can be achieved.

The general agreement between the observed and synthetic flux and polarization spectra has reached a high level which indicates that the theoretical spectra describe the underlying physics of magnetic atmospheres more or less correctly by now. The remaining differences can be traced back to a number of sources. On the theoretical side these are: (i) uncertainties in the absorption coefficients and approximations in the treatment of the line broadening, in particular, the treatment of Stark broadening in magnetic atmospheres; (ii) the finite resolution of the database, currently limited to 1 MG, which causes small wiggles in the spectra. On the observational side these are: (iii) remaining problems with the flux calibration, i.e. in the observationally derived response functions, which we have attempted to correct for by re-normalizing the observed and model spectra relative to each other; (iv) small errors in the flat fielding procedure; and (v) uncertainties in the definition of the standard deviations  $\sigma_j$  of spectral flux and polarization which enter Eq. (3.3) and determine  $\chi^2_{\text{red}}$ .

### Case (ii): $P_{\text{rot}} > 2.7 \text{ h}$

We have repeated the analysis for rotational periods exceeding the preferred value of 2.7 h, in order to investigate whether the assumption of a longer period, which implies incomplete phase coverage, leads to a different field structure. The somewhat surprising, but also fortunate result

is that none of the investigated models yields a field structure which deviates substantially from the one derived above.

We replace the assumed value 0.50 of the phase interval  $\Delta\phi$  covered by our data by 0.25, 0.18, and 0.12, corresponding to rotational periods of 5.4 h, 7.5 h, and 11.3 h. We consider first the case of  $P_{\text{rot}} = 5.4$  h. The important finding is that the assumption  $\Delta\phi = 0.25$  does not imply the occurrence of a double wave of full period 5.4 h in the Zeeman features, but rather a field structure similar to case (i) seen at the larger inclination of  $i \simeq 32^\circ$ . At least, this is true for our models which lack multipole components higher than the octupole. As an example, we list in Table 3.2, line (7), the parameters for a non-aligned, off-centred dipole-quadrupole-octupole combination with an assumed period of 5.4 h, which should be compared with the model in line (6) for our preferred period of 2.7 h. For both models, the Schmidt et al. and our data are concatenated at the phase of Zeeman maximum, but in line (6) the combined data cover a full rotational period, and in line (7) only half a period. We conclude that the dominance of the quadrupole and octupole over the dipole is not affected by the different choice of the rotational period.

The case (ii) model with  $\Delta\phi = 0.18$  requires an inclination of  $i = 34^\circ$ , whereas for  $\Delta\phi = 0.12$  (with  $i = 53^\circ$ ) a satisfactory fit could no longer be obtained. This suggests a maximum value of the rotational period of about 9 h. It is not surprising that for decreasing  $\Delta\phi$  the necessary field variation between Zeeman maximum and minimum can only be produced by larger inclinations which allow for a more rapid variation of the Zeeman features.

### 3.6 Discussion

In this study, we have fitted model Zeeman spectra to high-quality spectropolarimetric data of HE 1045–0908 using our Zeeman tomography code (Paper I), assuming a *bona fide* rotational period of about 2.7 h. We have achieved a good fit which reveals a dominant quadrupole component with additional dipole and octupole contributions. HE 1045–0908 is the first white dwarf in which a quadrupole component has been detected so clearly. This result is found to be robust against the assumption of a longer rotational period with an upper limit at about 9 h. In our model, the orientations of the axes of dipole, quadrupole, and octupole have been treated as free parameters, and it turned out that this freedom is important in obtaining the best fit. This assumption deviates from a truncated multipole expansion with all  $m \neq 0$  components and is justified by its simplicity and ease of visualization. We are confident that we have reached a reliable reconstruction of the general field structure of HE 1045–0908.

The most frequent photospheric field strength and direction is represented by the maximum in the  $B$ - $\psi$  diagram at 16 MG and positive  $\cos\psi$ . This is also the field which appears most prominently in the Zeeman spectra, and a cursory analysis would catalogue this star as “having a field strength of 16 MG”. Other sections of the star display field strengths up to  $\sim 75$  MG, however, which are less conspicuous in the observed spectra. Considering the complete information on the field distribution, we find it difficult to assign either a “characteristic field strength” or a “polar field strength” to HE 1045–0908. More appropriate would be quotations like: (i) the most frequent field is 16 MG; (ii) the mean field over the visible surface averaged by the surface area is 34 MG; and (iii) the range of field strengths is 10–75 MG. Our general experience is, however, that a quotation of type (iii) is model-dependent because models for some stars studied by us imply

a high-field extension in the  $B$ – $\psi$  diagram, which covers only a small area near the limb of the visible surface and has little statistical significance.

The derived field structure of HE 1045–0908 is primarily defined by the  $B$ – $\psi$  diagram rather than by the strengths and angles of the individual components. As pointed out in Paper I, different parameter combinations of the individual components could lead to a similar  $B$ – $\psi$  diagram. This is why Donati et al. (1994) refrained from specifying multipole components and suggested to directly optimize the  $B$ – $\psi$  diagram. The approach of Donati et al. does not guarantee, however, that the derived  $B$ – $\psi$  diagram corresponds to a physically possible field. This potential trap is avoided in our approach, which has the additional advantage that we can specify the contributions of individual multipole components. Furthermore, since we have gradually increased the level of complexity of our field parametrization starting from the elementary case of a centred dipole, we can be sure to have found the *simplest* configuration compatible with the observations. We cannot exclude additional small scale structure of the surface field, but suggest that such a structure cannot dominate HE 1045–0908 because it would destroy the remarkably high degree of circular polarization of up to  $\sim 10\%$ .

Due to the small inclination ( $i = 17^\circ$ ) found for the best-fitting model geometry, a fraction of 35% of the stellar surface is permanently hidden from view. In Paper I we have shown that this lack of information does not affect the accuracy of the derived field structure on the visible part of the surface. The field structures predicted by all our models for the hidden part of the surface are reasonable and “well-behaved”, i.e. there are no extreme field values or gradients. For instance, for the case (i) model of Fig. 3.5 and line (6) of Table 3.2, the range of field strengths encountered on the visible fraction of the surface is 10–76 MG, while for the whole star it is 9–76 MG. Our simulations had shown that reconstruction artefacts can arise if the field parametrization involves more free parameters than needed to describe the field structure adequately (cf. Fig. 10 in Paper I)<sup>5</sup>. This does not happen in our stepwise approach with a limited number of parameters.

It goes without saying that the final determination of the field structure of HE 1045–0908 would greatly benefit from a measurement of its rotational period and full phase coverage of the Zeeman spectropolarimetry.

With  $T_{\text{eff}} \simeq 10^4$  K, HE 1045–0908 is  $\sim 0.5$  Gyr old, less than the Ohmic decay times of the detected multipole components (Wendell et al. 1987; Cumming 2002). Hence, the strong quadrupole component could be a remnant from the main-sequence (or pre-main-sequence) evolution of the progenitor star. Alternatively, it could be produced by field evolution in the white dwarf stage as suggested by Muslimov et al. (1995). Now that tomographic methods have reached a high accuracy thanks to advanced spectropolarimetric instruments at 8-m class telescopes, it would be interesting to follow up this question by a detailed field analysis of white dwarfs of different ages, supplemented by more extensive theoretical calculations of the evolution of white dwarf magnetic fields over their cooling times.

---

<sup>5</sup> Fig. 2.10 in this thesis.



### 3.7 Acknowledgements

The referee G. Mathys provided helpful and valuable comments and suggested, in particular, to investigate rotational periods larger than 2.7 h. This work was supported in part by BMBF/DLR grant 50 OR 9903 6. BTG was supported by a PPARC Advanced Fellowship.

### 3.8 Appendix: Table of best-fit parameters

(see next page)

**Table 3.2:** Best-fit magnetic parameters for the different parametrizations of the magnetic field shown in Fig. 3.3. The uncertainties in the last digit are denoted by the values in brackets. A short description of the individual models is followed by the formal value of the reduced  $\chi^2$  (see text). All models assume a rotational period of 2.7 h, except for model (7), which has been computed for 5.4 h.

$i$ ( $^\circ$ )	$B_{\text{pol}}^{\text{d}}$ (MG)	$\Theta^{\text{d}}$ ( $^\circ$ )	$\Phi^{\text{d}}$ ( $^\circ$ )	$B_{\text{pol}}^{\text{q}}$ (MG)	$\Theta^{\text{q}}$ ( $^\circ$ )	$\Phi^{\text{q}}$ ( $^\circ$ )	$B_{\text{pol}}^{\text{o}}$ (MG)	$\Theta^{\text{o}}$ ( $^\circ$ )	$\Phi^{\text{o}}$ ( $^\circ$ )	$x'_{\text{off}}$ ( $R_{\text{WD}}$ )	$y'_{\text{off}}$ ( $R_{\text{WD}}$ )	$z'_{\text{off}}$ ( $R_{\text{WD}}$ )
<i>(1) D ctrd (centred dipole, <math>\chi_{\text{red}}^2 = 121.9</math>)</i>												
57 (3)	−32 (1)	14 (1)	30 (1)	—	—	—	—	—	—	—	—	—
<i>(2) Q ctrd (centred quadrupole, <math>\chi_{\text{red}}^2 = 104.9</math>)</i>												
11 (2)	—	—	—	−36 (1)	14 (1)	18 (1)	—	—	—	—	—	—
<i>(3) D offs (off-centred dipole, <math>\chi_{\text{red}}^2 = 29.7</math>)</i>												
20 (3)	−27 (3)	41 (5)	29 (2)	—	—	—	—	—	—	0.08 (1)	0.02 (1)	0.27 (1)
<i>(4) Q offs (off-centred quadrupole, <math>\chi_{\text{red}}^2 = 27.2</math>)</i>												
18 (3)	—	—	—	−49 (4)	20 (1)	20 (2)	—	—	—	−0.13 (1)	0.01 (1)	0.06 (1)
<i>(5) DQO na ctrd (non-aligned, centred combination of dipole, quadrupole, and octupole, <math>\chi_{\text{red}}^2 = 26.8</math>)</i>												
20 (3)	−12 (2)	39 (4)	17 (2)	−45 (4)	36 (3)	34 (6)	−19 (1)	60 (5)	27 (3)	—	—	—
<i>(6) DQO na offs (non-aligned, off-centred combination of dipole, quadrupole, and octupole, <math>\chi_{\text{red}}^2 = 24.5</math>)</i>												
17 (3)	−16 (2)	71 (5)	344 (2)	−36 (3)	21 (3)	138 (6)	−18 (2)	70 (9)	115 (7)	0.07 (1)	−0.08 (1)	0.31 (2)
<i>(7) DQO na offs (non-aligned, off-centred combination of dipole, quadrupole, and octupole, <math>P_{\text{rot}} = 5.4</math> h, <math>\chi_{\text{red}}^2 = 26.3</math>)</i>												
32 (4)	−13 (1)	31 (4)	1 (1)	−37 (3)	24 (3)	209 (4)	−25 (3)	69 (12)	245 (10)	−0.08 (1)	0.07 (1)	0.27 (2)

# 4 The 70–80 Megagauss magnetic field of PG 1015+014

F. EUCHNER<sup>1</sup>, S. JORDAN<sup>2</sup>, K. BEUERMANN<sup>1</sup>, K. REINSCH<sup>1</sup>, & B.T. GÄNSICKE<sup>3</sup>

<sup>1</sup> Institut für Astrophysik, Universität Göttingen, Friedrich-Hund-Platz 1, D-37077 Göttingen, Germany

<sup>2</sup> Astronomisches Rechen-Institut am ZAH, Mönchhofstr. 12–14, D-69120 Heidelberg, Germany

<sup>3</sup> Department of Physics, University of Warwick, Coventry CV4 7AL, UK

Based on observations collected at the European Southern Observatory, Paranal, Chile, under programme ID 63.P-0003(A).

Published in *Astronomy & Astrophysics* (2006) **451**, 671–681, [doi:10.1051/0004-6361:20064840](https://doi.org/10.1051/0004-6361:20064840)

## 4.1 Abstract

**Aims:** We analyse the magnetic field geometry of the magnetic DA white dwarf PG 1015+014 with our Zeeman tomography method.

**Methods:** This study is based on rotation-phase resolved optical flux and circular polarization spectra of PG 1015+014 obtained with FORS1 at the ESO VLT. Our tomographic code makes use of an extensive database of pre-computed Zeeman spectra. The general approach has been described in Papers I and II of this series (Chapters 2 and 3 of this thesis).

**Results:** The surface field strength distributions for all rotational phases of PG 1015+014 are characterised by a strong peak at 70 MG. A separate peak at 80 MG is seen for about one third of the rotation cycle. Significant contributions to the Zeeman features arise from regions with field strengths between 50 and 90 MG. We obtain equally good simultaneous fits to the observations, collected in five phase bins, for two different field parametrizations: (i) a superposition of individually tilted and off-centred zonal multipole components; and (ii) a truncated multipole expansion up to degree  $l = 4$  including all zonal and tesseral components. The magnetic fields generated by both parametrizations exhibit a similar global structure of the absolute surface field values, but differ considerably in the topology of the field lines. An effective photospheric temperature of  $T_{\text{eff}} = 10\,000 \pm 1000$  K was found.

**Conclusions:** Remaining discrepancies between the observations and our best-fit models suggest that additional small-scale structure of the magnetic field exists which our field models are unable to cover due to the restricted number of free parameters.

## 4.2 Introduction

In about 170 of the 5448 white dwarfs (WDs) listed in the Web Version<sup>1</sup> of the Villanova White Dwarf Catalog magnetic fields between 2 kG–1000 MG have been detected, corresponding to a fraction of  $\simeq 3\%$  (McCook & Sion 1999; Wickramasinghe & Ferrario 2000; Vanlandingham et al. 2005). Most of the WDs have not been scrutinisingly examined for the presence of a magnetic field, however, and a statistical study suggests that the true fractional incidence could be as high as 20% (Liebert et al. 2003; Schmidt et al. 2003). The magnetic white dwarfs (MWDs) are widely believed to be the successors of the chemically peculiar magnetic Ap stars, which are the only main sequence stars to show substantial globally organised magnetic fields. However, this scenario is challenged by the recent detections of kilogauss-size fields in several MWDs as well as in their direct progeny (central stars of planetary nebulae and hot subdwarfs, Aznar Cuadrado et al. 2004, Jordan et al. 2005, O’Toole et al. 2005). Undoubtedly, further theoretical and observational efforts are required in order to shed more light on the role magnetic fields play in the key stages of post-main sequence evolution. For the present purpose, we consider MWDs as stars displaying a field strength  $B \gtrsim 1$  MG.

Due to the intrinsic faintness of WDs, 8-m class telescopes are required in order to record high-quality spectropolarimetric data with sufficient time resolution as a basis for studies of the magnetic field geometry. In the course of our Zeeman tomography programme we have conducted observations for a number of isolated (non-accreting) and accreting MWDs at the ESO VLT with FORS1 in the spectropolarimetric mode.

<sup>1</sup> <http://www.astronomy.villanova.edu/WDCatalog/index.html>, January 2006.

In the present work – the third paper of our series on Zeeman tomography – we present an application of our code to observations of the non-accreting white dwarf PG 1015+014 and find a field geometry that deviates strongly from centred dipoles or quadrupoles. In the first paper of the series, we have demonstrated that Zeeman tomography is a suitable method to recover field geometries by analysing synthetically generated spectra (Euchner et al. 2002, hereafter Paper I). In a first application of this theory, we have derived a quadrupole-dominated field structure with a prevailing field of  $\simeq 16$  MG for HE 1045–0908 (Euchner et al. 2005b, hereafter Paper II).

The magnetic DA white dwarf PG 1015+014, discovered in the Palomar Green survey (Green et al. 1987), was observed by Wickramasinghe & Cropper (1988, hereafter WC88) with the RGO spectrograph at the AAT in the wavelength range 4000–7000 Å. Their phase-resolved spectroscopy and low-resolution circular polarimetry revealed significant modulations in flux and circular polarization ( $V/I$ ) over the rotation cycle. From nearly sinusoidal oscillations of the wavelength-averaged degree of circular polarization between  $-1.5\%$  and  $1.5\%$  the authors derived a rotational period of  $P_{\text{rot}} = 98.7$  min, which was later confirmed with higher accuracy by Schmidt & Norsworthy (1991) who used white-light circular polarimetry. In the individual polarization spectra of WC88,  $|V/I|$  is  $\simeq 5\%$  in the continuum and up to  $\simeq 10\%$  in individual features. They fitted theoretical MWD model spectra to the observations and found an obliquely rotating magnetic dipole model with a polar field strength of  $B_{\text{pol}}^{\text{d}} = 120 \pm 10$  MG and an almost equator-on view to be the best-fitting field geometry. Remaining discrepancies between observations and model spectra were attributed to higher-field regions superimposed on the dipolar field structure. Our analysis provides a substantially improved insight into the field structure of PG 1015+014.

### 4.3 Observations

We have obtained spin-phase resolved circular spectropolarimetry of PG 1015+014 with FORS1 at the ESO VLT on May 15, 1999. The spectrograph was operated in spectropolarimetric (PMOS) mode, with the GRIS\_300V+10 grism and an order separation filter GG 375, yielding a usable wavelength range  $\sim 3850$ – $7900$  Å. With a slit width of  $1''$  the FWHM spectral resolution was  $13$  Å at  $5500$  Å. The observational data have been reduced according to standard procedures (bias, flat field, night sky subtraction, wavelength calibration, atmospheric extinction, flux calibration) using the context MOS of the ESO MIDAS package. The instrumental setup and the data reduction are analogous to those employed for our analysis of HE 1045–0908 (Paper II).

We secured a sequence of 12 exposures with an exposure time of 8 min each, covering a full rotation cycle. We were able to reach a signal-to-noise ratio  $S/N \simeq 100$  for the individual flux spectra (Fig. 4.1, left panel). The wavelength-dependent degree of circular polarization ( $V/I$ ) was computed from two consecutive exposures – with the retarder plate positions differing by  $90^\circ$  – in order to eliminate Stokes parameter crosstalk, thus yielding six independent phase bins. The flux spectra do not show the typical absorption signature of low- and intermediate-field MWDs with the  $\text{H}\alpha$   $\pi$  component at the zero-field wavelength surrounded by broader  $\sigma^-$  and  $\sigma^+$  troughs, but exhibit a variety of distinct sharp lines scattered over the whole optical range which vary in strength, position, and shape with the rotational phase. The continuum circular polarization differs significantly from zero for most phases. Both phenomena are characteristic of a high-field object with  $B \gtrsim 50$  MG (e.g. Wickramasinghe & Ferrario 2000).

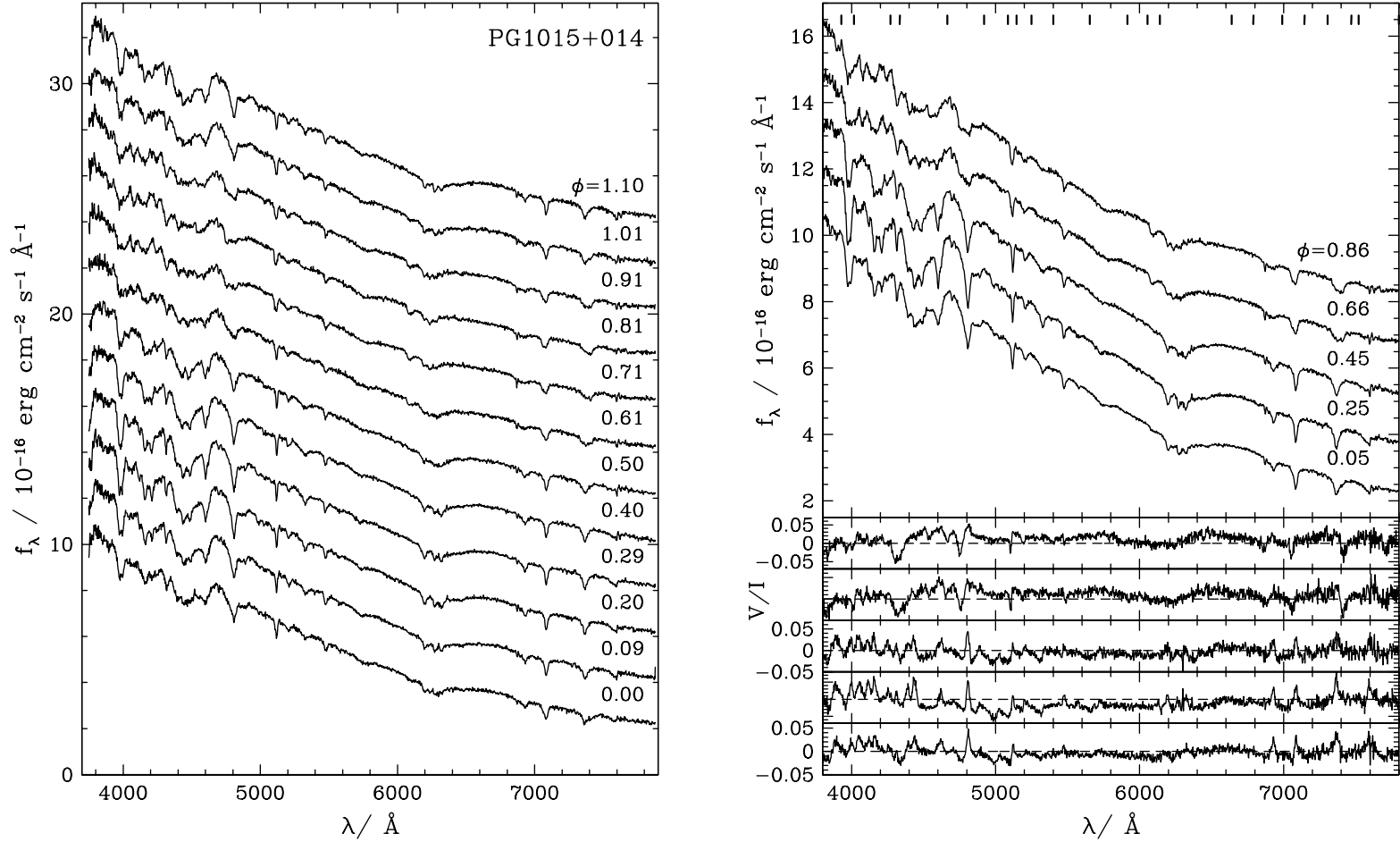


**Figure 4.1:** *Left panel:* Flux spectra of PG 1015+014 from May 1999. The uppermost 11 spectra have been shifted upwards by 2 flux units, respectively. *Right panel:* Combined flux and circular polarization spectra of PG 1015+014 from the May 1999 observations. These spectra, which have been collected into five phase bins, will be used as input spectra for the Zeeman tomography procedure. For clarity, the uppermost four flux spectra have been shifted upwards by 1.5 flux units, respectively. The tick marks below the top axis indicate the wavelengths that were used to adjust the continuum flux level of the the model spectra to the observations.

We collect the observed flux and circular polarization spectra into five nearly-equidistant phase bins ( $\phi = 0.05, 0.25, 0.45, 0.66, 0.86$ ). The phases refer to the ephemeris of Schmidt & Norsworthy (1991) with  $\phi = 0$  denoting the change from positive to negative continuum polarization<sup>2</sup>. These flux and polarization spectra (Fig. 4.1, *right panel*) form the basis of our tomographic analysis. We investigate two particular phases in greater detail:  $\phi = 0.25$ , when the Zeeman features are strongest (“Zeeman maximum”); and  $\phi = 0.86$ , when they are weakest (“Zeeman minimum”).

## 4.4 Qualitative analysis of the magnetic field geometry

As a first step of the analysis, we compare the positions and strengths of the most prominent features in the observed spectra with the expected field-dependent wavelengths of the hydrogen transitions  $\lambda^H(B)$ , henceforth referred to as  $\lambda$ - $B$  curves (Forster et al. 1984; Rösner et al. 1984; Wunner et al. 1985). In Fig. 4.2, we show the observed flux and circular polarization spectra along with the  $\lambda$ - $B$  curves for  $\phi = 0.25$  (*left panel*) and  $0.86$  (*right panel*). Transitions that could be unambiguously identified with specific spectral features have been marked with filled grey circles and are listed in Table 4.1. Possible or unlikely identifications are displayed as open circles. In the presence of an electric field additional transitions can occur which formally correspond to  $|\Delta l| = 0, 2, 4, \dots$ , with  $l$  being the angular momentum quantum number in the zero-field nomenclature. These components have been plotted as dashed curves in the bottom parts of Fig. 4.2.

In the Zeeman maximum spectrum ( $\phi = 0.25$ ), three  $H\alpha$   $\pi$  and four  $H\alpha$   $\sigma^+$  transitions with  $\lambda > 6000 \text{ \AA}$  are clearly visible as positive peaks superimposed on a negative polarization continuum. In particular, the narrow feature at  $7085 \text{ \AA}$  which corresponds to a local extremum of the  $2s_0 \rightarrow 3p_{-1}$   $\lambda$ - $B$  curve allows a reliable estimation of the prevailing field strength. For  $\lambda < 6000 \text{ \AA}$ , we identify three strong features showing positive polarization (at  $4610, 4805$ , and  $5117 \text{ \AA}$ ) with  $H\beta$   $\sigma^+$  transitions. Our identifications of several line features differ from those suggested by WC88 for the same rotational phase. The feature at  $5326 \text{ \AA}$  shows a noticeable negative polarization and is interpreted as a blend of a  $H\alpha$   $\sigma^-$  and a  $H\beta$   $\sigma^+$  component, with the  $2p_{-1} \rightarrow 3d_0$  transition dominating. The strong line at  $5475 \text{ \AA}$  with positive polarization probably arises from the  $H\alpha$   $\pi$  transition  $2p_0 \rightarrow 3s_0$ . The feature at  $5930 \text{ \AA}$  reported by WC88 is not present in our data. Furthermore, there is a distinct feature with a positive peak in polarization at  $5200 \text{ \AA}$  which they attribute to the  $H\alpha$   $\sigma^-$  transition  $2p_{+1} \rightarrow 3d_{+2}$ . We question this identification because the  $H\alpha$   $\sigma^-$  components produce lines with strong negative polarization. However, no obvious match with a specific  $\lambda$ - $B$  curve can be found in Fig. 4.2, so the origin of this feature remains unclear. We do not attempt to identify spectral features at wavelengths  $\lambda < 4600 \text{ \AA}$  because the number of candidate transitions from the overlapping  $H\beta$  and  $H\gamma$  manifolds is too large. Taking into account all these identifications, we conclude that the distribution of the corresponding field strengths must be centred quite sharply at  $\simeq 70 \text{ MG}$ . To illustrate this, we show in the top part of Fig. 4.2 (*left panel*) a theoretical circular polarization spectrum for a *single* value  $B = 69 \text{ MG}$  with  $\psi = 51^\circ$ , and  $T_{\text{eff}} = 10\,000 \text{ K}$ , where  $\psi$  denotes the viewing angle between the magnetic field direction and the line of sight.

<sup>2</sup> These authors used a different convention for the sign of the circular polarization than we did, since in their data  $V/I$  changes from negative to positive values at  $\phi = 0$ .

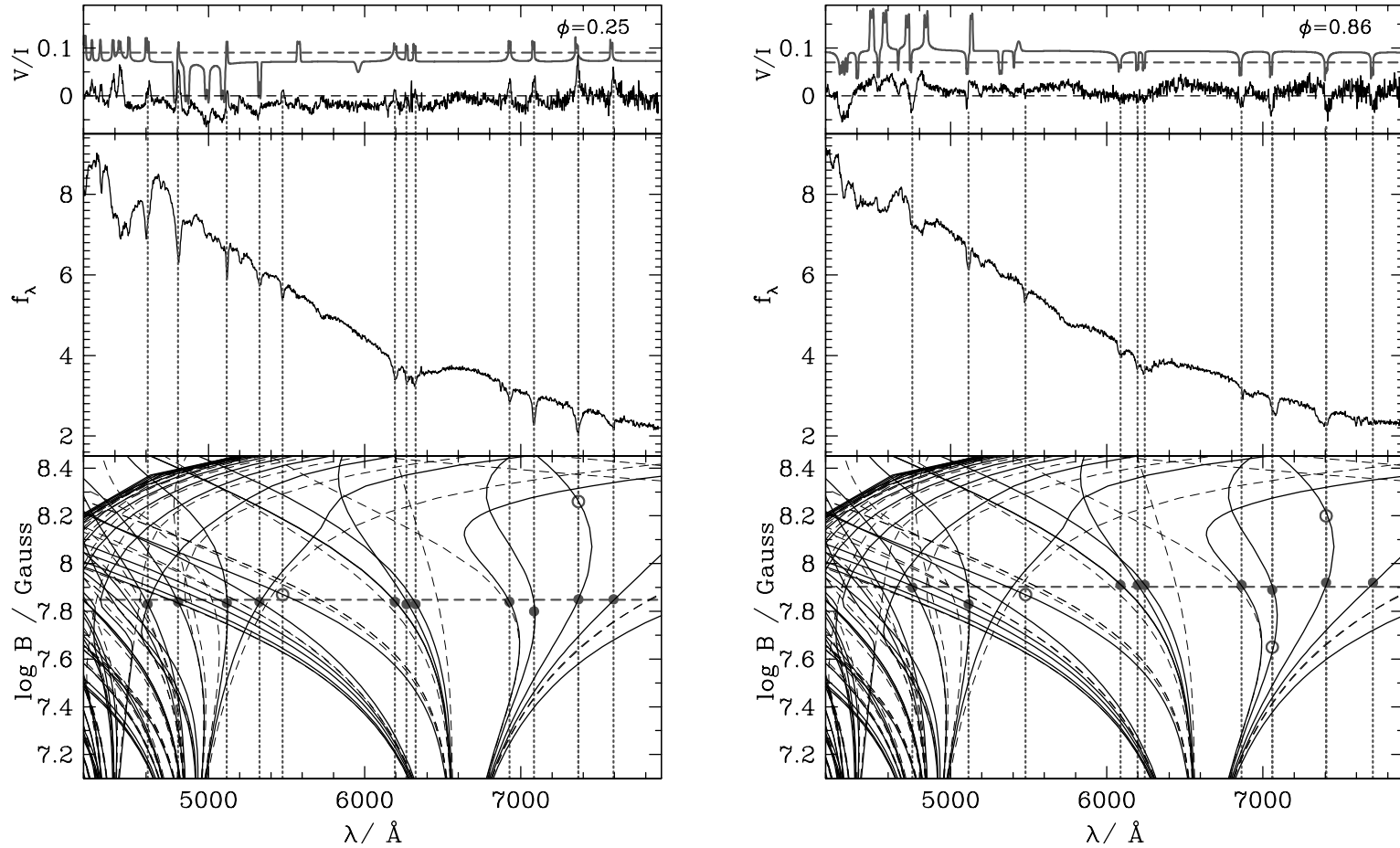


**Figure 4.2:** Zeeman maximum ( $\phi = 0.25$ , *left panel*) and minimum ( $\phi = 0.86$ , *right panel*) flux ( $f_\lambda$ ) and circular polarization ( $V/I$ ) spectra for PG 1015+014, plotted along with the theoretically predicted field-dependent transition wavelengths for Balmer absorption lines ( $\lambda$ – $B$  curves). Transitions corresponding formally to  $|\Delta l| = 0, 2, 4, \dots$  with the zero-field angular momentum quantum number  $l$  have been plotted as dashed curves in the bottom parts of the figures. Filled circles denote unambiguous identifications of transitions, open circles less certain ones. In the top parts, theoretical circular polarization spectra are shown for comparison (shifted upwards for clarity, see the text for the adopted model parameters).  $f_\lambda$  is given in units of  $10^{-16} \text{ erg cm}^{-2} \text{ s}^{-1} \text{ \AA}^{-1}$ .



**Table 4.1:** Positions of observed Zeeman features and corresponding Balmer transitions. A colon denotes a less certain identification.

$\lambda / \text{\AA}$	Transition	$\lambda / \text{\AA}$	Transition
$(\phi = 0.25)$		$(\phi = 0.86)$	
4610	H $\beta$ ( $2s_0 \rightarrow 4f_0$ )	4755	H $\beta$ ( $2p_0 \rightarrow 4d_{-1}$ )
	H $\beta$ ( $2p_{+1} \rightarrow 4s_0$ )	5115	H $\beta$ ( $2s_0 \rightarrow 4f_{-1}$ )
4805	H $\beta$ ( $2p_0 \rightarrow 4d_{-1}$ )	5480	H $\alpha$ ( $2p_0 \rightarrow 3s_0$ ):
5117	H $\beta$ ( $2s_0 \rightarrow 4f_{-1}$ )	6088	H $\alpha$ ( $2p_{\pm 1} \rightarrow 3d_{\pm 1}$ )
5326	H $\alpha$ ( $2p_{-1} \rightarrow 3d_0$ )	6198	H $\alpha$ ( $2s_0 \rightarrow 3p_0$ )
	H $\beta$ ( $2p_{+1} \rightarrow 4d_0$ )	6243	H $\alpha$ ( $2p_0 \rightarrow 3d_0$ )
5475	H $\alpha$ ( $2p_0 \rightarrow 3s_0$ ):	6864	H $\alpha$ ( $2p_{+1} \rightarrow 3s_0$ )
6193	H $\alpha$ ( $2p_{\pm 1} \rightarrow 3d_{\pm 1}$ )	7060	H $\alpha$ ( $2s_0 \rightarrow 3p_{-1}$ )
6268	H $\alpha$ ( $2s_0 \rightarrow 3p_0$ )	7405	H $\alpha$ ( $2p_{-1} \rightarrow 3d_{-2}$ )
6326	H $\alpha$ ( $2p_0 \rightarrow 3d_0$ )	7705	H $\alpha$ ( $2p_0 \rightarrow 3d_{-1}$ )
6927	H $\alpha$ ( $2p_{+1} \rightarrow 3s_0$ )		
7085	H $\alpha$ ( $2s_0 \rightarrow 3p_{-1}$ )		
7369	H $\alpha$ ( $2p_{-1} \rightarrow 3d_{-2}$ )		
7594	H $\alpha$ ( $2p_0 \rightarrow 3d_{-1}$ )		

In the Zeeman minimum spectrum ( $\phi = 0.86$ ), the absorption signature for  $\lambda > 6000 \text{\AA}$  is similar to that at Zeeman maximum, although the H $\alpha$   $\pi$  line components are not visible as separate peaks in  $V/I$ , but rather produce a broad depression of the overall positive continuum polarization. The H $\alpha$   $\sigma^+$  components are wider than those at  $\phi = 0.25$ . Both effects suggest a broader distribution of field strengths at Zeeman minimum. A theoretical circular polarization spectrum for a single value  $B = 82 \text{ MG}$ ,  $\psi = 129^\circ$ , and  $T_{\text{eff}} = 10\,000 \text{ K}$  provides a good indication for the prevailing field strength and direction. As can be seen from the change of polarity in the continuum circular polarization, the net magnetic field direction has changed sign along the line of sight. The fact that for both phases, which are separated by about half a rotation cycle ( $\Delta\phi = 0.39$ ), the field distributions seem to be clearly peaked at values differing by only  $\simeq 20\%$  indicates a field geometry more complex than centred or off-centred dipoles or quadrupoles.

## 4.5 Zeeman tomography of the magnetic field

Our Zeeman tomography synthesises the observed spectra in a best-fit approach. It makes use of an extensive pre-computed database of theoretical flux and circular polarization spectra of magnetic white dwarf atmospheres, with  $B$ ,  $\psi$ ,  $T_{\text{eff}}$ ,  $\log g$ , and the direction cosine  $\mu = \cos \vartheta$  as free parameters, where  $\vartheta$  denotes the angle between the normal to the surface and the line of sight. The three-dimensional grid of 46 800 Stokes  $I$  and  $V$  profiles covers 400  $B$  values (1–400 MG, in 1 MG steps), nine  $\psi$  values (equidistant in  $\cos \psi$ ), and 13 temperatures (8000–50 000 K) for fixed  $\log g = 8$  and  $\mu = 1$ . Limb darkening is accounted for in an approximate way by the linear interpolation law  $I_\lambda(\mu)/I_{\lambda,\mu=1} = a + b\mu$  with constant coefficients  $a = 0.53$  and  $b = 0.47$ . The best fit to the absolute flux distribution of PG 1015+014 was obtained with an effective temperature of  $T_{\text{eff}} = 10\,000 \pm 1000 \text{ K}$ . We adopt this value in the subsequent analysis.

In order to determine the misfit between the observations and the model spectra for a given set of magnetic parameters, we use the classical reduced  $\chi^2$  as our penalty function. The optimisation problem of finding the best-fitting parameters is solved using an evolutionary strategy, implemented by the *evoC* library (Trint & Utecht 1994)<sup>3</sup>. We assign equal statistical weight to the flux and polarization spectra for all five rotational phases and to all wavelengths within the individual spectra. The statistical noise of the observations entering the  $\chi^2$  function has been estimated by comparing the observed spectra after the application of a Savitzky-Golay filter of 20 Å width with the unprocessed versions. The flux level of the model spectra has been adjusted to the observations at the wavelengths marked with ticks at the top of Fig. 4.1 (*right panel*). This is an attempt to remove differences between observed and model flux spectra with wavelengths  $\gtrsim 100$  Å, as expected from the remaining uncertainties in the detector response function. We do not correct either for differences between the spectra on shorter wavelengths, nor do we apply any correction to the polarization spectra. The resulting  $\chi_{\text{red}}^2$  values are of the order of 80 indicating a gross underestimation of the errors which enter the  $\chi^2$  computation. Larger observational errors and remaining systematic uncertainties in the model spectra probably both contribute to this result. We have experimented with different statistical weights assigned to different wavelength regions – as specific line features or subsections of the continuum – but found no convincing way to better define the goodness of fit. We compromise on using the formal  $\chi_{\text{red}}^2$ , even if large, as a guide line and decide by an admittedly subjective ‘by eye’ process which individual of similarly good fits to accept.

#### 4.5.1 Field parametrization

We have embarked on two different strategies in order to find an adequate parametrization of the magnetic field geometry (see also Paper I). The classical approach is that of an expansion of the scalar magnetic potential into a series of spherical harmonics, characterised by degree  $l$  and order  $m$  with  $m = 0$  to  $l$  for each  $l$ . Given  $l$  and  $m$ , two free parameters  $g_l^m$  and  $h_l^m$  have to be specified, or one parameter  $g_l^0$  only for the zonal components with  $m = 0$  (Langel 1987). The approach is powerful, but is limited to the description of rather simple structures if one truncates the expansion at low values of  $l$ . Such a truncation is necessary in order to avoid convergence problems of the fit, given the rapid growth in the number of fit parameters which increases as  $l(l+2)$  for the full  $l, m$ -expansion. Conceptually simple structures, such as the sum of a quadrupole and octupole with their axes inclined relative to each other, cannot be realised if the series is truncated at low  $l \geq 3$ . As an alternative approach, we adopt a hybrid model consisting only of zonal ( $m = 0$ ) harmonics with independent tilt angles and off-centre shifts. All tesseral components ( $m \neq 0$ ) are ignored in this case. Examples are, e.g., a combination of dipole, quadrupole and octupole, and also a combination of three dipoles independently inclined and offset from the centre. Further details on the field parametrizations are given in Papers I and II.

In the following Section, we proceed systematically from simple structures, as centred or off-centred single zonal components, over the sum of such components, individually tilted and/or offset, to a full multipole expansion truncated at  $l = 4$ . The number of free parameters varies between 4 and 27. In the case of the hybrid model, the fit parameters for each component are the polar field strength  $B_{\text{pol}}$ , the tilt  $\Theta$  and azimuth  $\Phi$  of the magnetic axis, and, if applicable, the offsets  $x'_{\text{off}}$ ,  $y'_{\text{off}}$ , and  $z'_{\text{off}}$  from the centre plus the inclination of the rotational axis relative to

<sup>3</sup> <ftp://biobio.bionik.tu-berlin.de/pub/software/evoC/>

the line of sight. For the truncated multipole model, we fit the  $l(l+2)$  parameters of the model, the two angles of the reference axis, and the inclination.

### 4.5.2 Results

For single centred dipoles, quadrupoles, or octupoles no satisfactory fits could be obtained. Nevertheless, we note that the best fit with a centred dipole to the single phase  $\phi = 0.25$  yielded a value of  $B_{\text{pol}}^{\text{d}} = 131 \pm 1$  MG and an angle of  $\alpha = 83^\circ$  between the magnetic dipole axis and the line of sight, which is compatible with the values quoted by Wickramasinghe & Cropper (1988). The model is far from optimal, however, in particular for the other phases.

In Fig. 4.3 we show the observed and best-fitting model circular polarizations at  $\phi = 0.25$  and 0.86 for selected hybrid and multipole parametrizations with increasing complexity. The simplest configuration is that of an offset dipole (denoted by D offs in Fig. 4.3). The corresponding values of the magnetic parameters are listed in Table 4.2. The overall shape of the continuum polarization is reproduced fairly well for all phases, but the model fails seriously in the spectral lines, especially for  $\phi = 0.86$ . For an offset quadrupole, the result was comparably poor. An offset octupole fared slightly better, but still was considered unsatisfactory. While acceptable fits could be obtained with offset dipoles and quadrupoles for HE 1045–0908 (Paper II), the magnetic field geometry of PG 1015+014 seems to be significantly more complex.

As a next step, we proceed to the same hybrid field models that yielded successful fits for HE 1045–0908. These are produced by the superposition of dipole, quadrupole, and octupole components and the introduction of a *common* off-centre shift. For the nonaligned centred dipole–quadrupole–octupole combination (DQO na ctrd in Fig. 4.3), the polarization spectrum at  $\phi = 0.86$  is reproduced remarkably well, in particular the broad negative dips in polarization at 4310 and 4740 Å, and the  $2s_0 \rightarrow 3p_{-1}$  transition at 7085 Å. The frequency distribution of magnetic field strengths and directions ( $B$ – $\psi$  diagram, Fig. B.4)<sup>4</sup> is double-peaked at fields of 69 and 81 MG in accordance with the considerations of Sect. 4.4. The essence, however, is that the reproduction is poor for the other phases, including  $\phi = 0.25$ , although  $\phi = 0.86$  fits well. Introducing a common offset to the model (DQO na offs in Fig. 4.3) improves the fit at  $\phi = 0.25$ , but shows significant deviations at  $\phi = 0.86$ . As can be seen from the best-fit magnetic parameters in lines (2) and (3) of Table 4.2, both the centred and the shifted hybrid model are dominated by the octupole component, again suggesting a rather complex geometry. We conclude that the models considered so far still do not suffice to achieve a fair reproduction at all phases.<sup>5</sup>

In an attempt to improve the fits, we stayed with hybrid models and tried to model a star with several field concentrations by adding three dipoles which are *individually* tilted and off-centred. The model fares surprisingly well despite the absence of quadrupole and octupole components. We conclude that the ability to place and adjust three spots meets reality rather closely. The fit results for this ‘triple dipole’ model are displayed in Fig. 4.4, Fig. 4.5, and Table 4.3 and are discussed below.

<sup>4</sup> Not shown in the version published in *Astronomy & Astrophysics*.

<sup>5</sup> In Appendix B, plots of the best-fitting spectra,  $B$ – $\psi$  diagrams, and surface field distributions for the three models discussed so far are shown in Figs. B.1–B.6. These figures have not been included in the version published in *Astronomy & Astrophysics*.

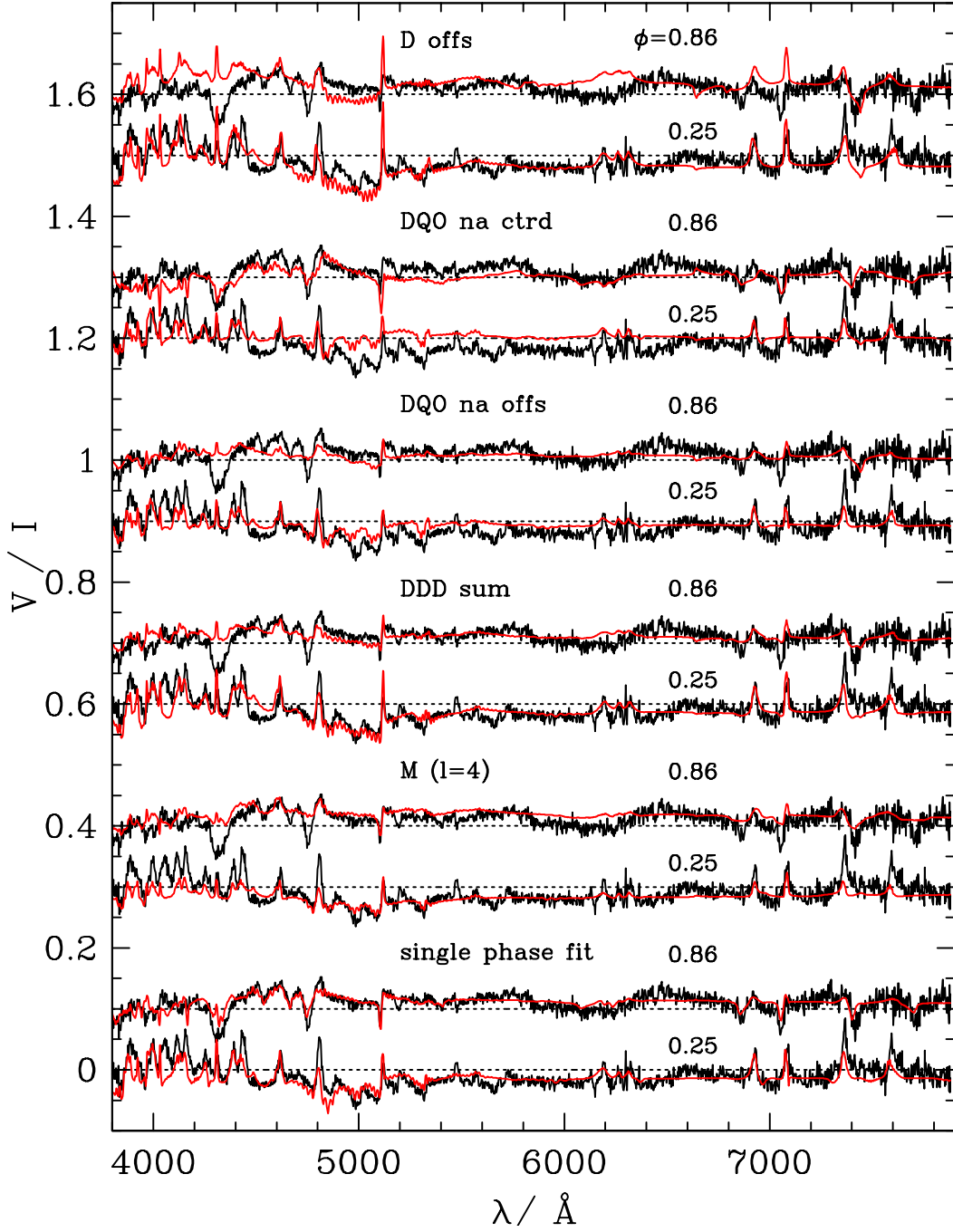


**Figure 4.3:** Observed circular polarization spectra for phases  $\phi = 0.25$  and  $0.86$  (black curves) and best-fit synthetic spectra (red curves) for different parametrizations of the magnetic field geometry. From top to bottom: off-centred dipole (D offs); centred, non-aligned combination of dipole, quadrupole, and octupole (DQO na ctrd); off-centred, non-aligned combination of dipole, quadrupole, and octupole (DQO na offs); superposition of three individually off-centred, non-aligned dipoles (DDD sum); truncated multipole expansion up to degree  $l = 4$ . The lowermost two curves show individual fits to single phases with a truncated multipole expansion up to  $l = 5$  ( $\phi = 0.25$ ) and  $l = 4$  ( $\phi = 0.86$ ). All curves except for the bottom one have been shifted vertically by suitable amounts in  $V/I$ , with the horizontal dashed lines indicating the respective levels of zero polarization.

**Table 4.2:** Best-fit magnetic parameters for the different parametrizations of the magnetic field shown in Fig. 4.3. The uncertainties in the last digit are denoted by the values in brackets. For each model, a short description is given in the first line. The best-fit inclinations are  $24^\circ \pm 3^\circ$  (model 1),  $45^\circ \pm 3^\circ$  (model 2), and  $36^\circ \pm 4^\circ$  (model 3). The superscripts ‘d’, ‘q’, and ‘o’ refer to dipole, quadrupole, and octupole, the subscript ‘pol’ to the polar field strength. The last three columns give the offsets in units of the white dwarf radius. Formulae for the field structure are given in Paper I.

$B_{\text{pol}}^{\text{d}}$ (MG)	$\Theta^{\text{d}}$ ( $^\circ$ )	$\Phi^{\text{d}}$ ( $^\circ$ )	$B_{\text{pol}}^{\text{q}}$ (MG)	$\Theta^{\text{q}}$ ( $^\circ$ )	$\Phi^{\text{q}}$ ( $^\circ$ )	$B_{\text{pol}}^{\text{o}}$ (MG)	$\Theta^{\text{o}}$ ( $^\circ$ )	$\Phi^{\text{o}}$ ( $^\circ$ )	$x'_{\text{off}}$ ( $R_{\text{WD}}$ )	$y'_{\text{off}}$ ( $R_{\text{WD}}$ )	$z'_{\text{off}}$ ( $R_{\text{WD}}$ )
<i>(1) D offs (off-centred dipole)</i>											
−97 (2)	85 (3)	77 (4)	—	—	—	—	—	—	−0.113 (5)	−0.0036 (2)	0.162 (4)
<i>(2) DQO na ctrd (non-aligned, centred combination of dipole, quadrupole, and octupole)</i>											
−1.4 (1)	53 (13)	325 (6)	13.9 (6)	26 (2)	115 (5)	174 (1)	65 (3)	94 (5)	—	—	—
<i>(3) DQO na offs (non-aligned, off-centred combination of dipole, quadrupole, and octupole)</i>											
−38 (2)	85 (3)	82 (5)	−15 (3)	85 (5)	21 (3)	171 (6)	75 (6)	102 (5)	0.060 (5)	0.011 (1)	0.081 (4)

**Table 4.3:** Best-fit magnetic parameters for a superposition of three individually off-centred, non-aligned dipoles (labelled DDD sum in Fig. 4.3). The individual dipole components are denoted by D1, D2, and D3. The uncertainties in the last digit are given by the values in brackets. The best-fit inclination is  $23^\circ \pm 4^\circ$ .

	D1	D2	D3
$B_{\text{pol}}^{\text{d}}$ (MG)	−40 (2)	92 (5)	−38 (3)
$\Theta^{\text{d}}$ ( $^\circ$ )	44 (4)	63 (2)	63 (5)
$\Phi^{\text{d}}$ ( $^\circ$ )	339 (2)	276 (6)	134 (3)
$x'_{\text{off}}$ ( $R_{\text{WD}}$ )	0.04 (1)	−0.012 (2)	0.27 (1)
$y'_{\text{off}}$ ( $R_{\text{WD}}$ )	0.35 (3)	−0.136 (8)	0.080 (7)
$z'_{\text{off}}$ ( $R_{\text{WD}}$ )	0.33 (1)	−0.28 (3)	0.21 (2)

**Table 4.4:** Best-fit magnetic parameters for a truncated multipole expansion up to degree  $l = 4$  (labelled M in Fig. 4.3). The coefficients  $g_l^m$  and  $h_l^m$  are in MG. The best-fit inclination is  $47^\circ$ . The tilt and the azimuth of the multipole axis relative to the rotational axis are  $22^\circ$  and  $191^\circ$ .

$m$		$l = 1$	2	3	4
0	$g_l^m$	3.0	0.6	9.0	2.4
1	$g_l^m$	−12.5	19.0	−1.0	4.7
	$h_l^m$	−28.2	7.1	−15.6	11.0
2	$g_l^m$	−	−19.6	11.6	−10.2
	$h_l^m$	−	−15.6	−2.4	6.4
3	$g_l^m$	−	−	4.1	−1.7
	$h_l^m$	−	−	14.9	−6.9
4	$g_l^m$	−	−	−	−4.7
	$h_l^m$	−	−	−	−8.8

Finally, we considered a truncated multipole expansion up to  $l = 4$  which includes all orders with indices  $m = 0$  to  $l$ . This ‘truncated multipole’ model achieves a  $\chi_{\text{red}}^2$  value similarly good as the triple dipole model and both provide substantially better fits than the parametrizations discussed above if all rotational phases are considered. In particular, the wavelength-dependent level of the continuum circular polarization is reproduced more accurately. The results for the truncated multipole model are shown in Figs. 4.6 and 4.7 and in Table 4.4.

Although both magnetic field topologies are generated by entirely different parametrizations (Tables 4.3 and 4.4), the overall appearance of their  $B$ – $\psi$  diagrams is similar. For both configurations, the visible part of the surface field is dominated by an extended area with a rather small variation of the field strength that leads to the pronounced peaks at  $\simeq 70$  MG in the  $B$ – $\psi$  diagrams. The phases  $\phi = 0.25$  and  $0.45$  are almost entirely dominated by this region of constant (although not homogenous) field. For the remaining phases, the low- and high-field tails of the field strength distribution become more prominent. In the triple dipole model, the regions with low and high fields become manifest as small spots, one of which reaches up to  $\simeq 160$  MG. A second high-field



region appears at the stellar limb for phases  $\phi = 0.66$  and  $0.86$ . For the truncated multipole model, a similarly prominent high-field spot is not seen, but a low-field spot appears close to the stellar limb for  $\phi = 0.66$  and  $0.86$  and finds its counterpart in the hybrid model. The high-field regions are divided into two small spots with field values up to  $\simeq 90$  MG and pronounced negative  $\cos \psi$ , leading to a distinctive signature in the  $B$ - $\psi$  diagram, and two narrow areas at the stellar limb with  $B$  up to  $\simeq 150$  MG and  $245$  MG, which belong to high-field spots on the hidden part of the stellar surface. This comparison of the triple dipole model and the truncated multipole model emphasises the fact that the principal information on the field structure is contained in the  $B$ - $\psi$  diagrams. These diagrams indicate that the distributions of the magnetic field are similar, a conclusion which is impossible to draw from the numerical descriptions in Tables 4.3 and 4.4.

For both configurations substantial deviations from the observational data remain, e.g., at the broad dips in  $V/I$  at  $4310$  and  $4740 \text{ \AA}$  for phases  $\phi = 0.66$  and  $0.86$  which both models cannot reproduce correctly. While it is quite likely that a larger number of free parameters – and, hence, a still further increased complexity of the field – will improve the fits, our present optimisation procedure cannot handle more free parameters and prevents us to pursue this possibility further. As a consequence, it remains unclear what part of the remaining discrepancies, if any, may be due to systematic errors in the model spectra.

A possible way to answer the last question at least in part is to perform fits to the flux and polarization spectra for a *single* phase and abandon the requirement that the model should simultaneously fit the other phases. The resulting model may be wrong in a global sense, but will provide a more accurate description of the field distribution over the visible hemisphere at the selected phase. Figure 4.8 shows the resulting  $B$ - $\psi$  diagrams at  $\phi = 0.25$  and  $\phi = 0.86$  using the truncated multipole model with  $l = 5$  and  $l = 4$ , respectively. The corresponding polarization spectra are shown at the bottom of Fig. 4.3. The  $B$ - $\psi$  diagrams differ, in fact, from the distributions for the same phases obtained from the simultaneous fits to all five phases in Figs. 4.5 and 4.7. The most obvious new feature is the appearance of a second field maximum at  $82$  MG for  $\phi = 0.86$ . At  $\phi = 0.25$ , the distributions of the field strengths look similar, but the  $\psi$ -distributions and, hence, the field geometries differ (see Figs. 4.5, 4.7, and 4.8). We conclude that a major fraction of the misfits still present in our two best global fits is due to the disability of the models to appropriately account for the complexity of the field. The parameter-free spectral synthesis of Donati et al. (1994) would allow to optimise the fit to a single phase still further and answer the quest for the best possible fit with the present database, at the expense of a global field solution, however (see also Section 4.6).

We conclude that the field models used by us are barely sufficient to describe a single phase of the observations of PG 1015+014, and are certainly not complex enough to describe the global field configuration by fits to all five phases.

Several potential sources of deviations between observations and synthetic model spectra have been proposed in Paper II and arise both from remaining uncertainties on the observational (flat-fielding, flux calibration) and on the theoretical side. Since PG 1015+014 is dominated by substantially higher magnetic field strengths than HE 1045–0908, additional error sources for the theoretical model spectra have to be considered. With growing magnetic field strength, for instance, the influence of electric fields on line positions and strengths becomes increasingly important. For the case of arbitrarily oriented electric and magnetic fields no discrete symmetry is left, leading to slightly different transition wavelengths and oscillator strengths than those computed for the diamagnetic case, and even to the occurrence of additional dipole transitions

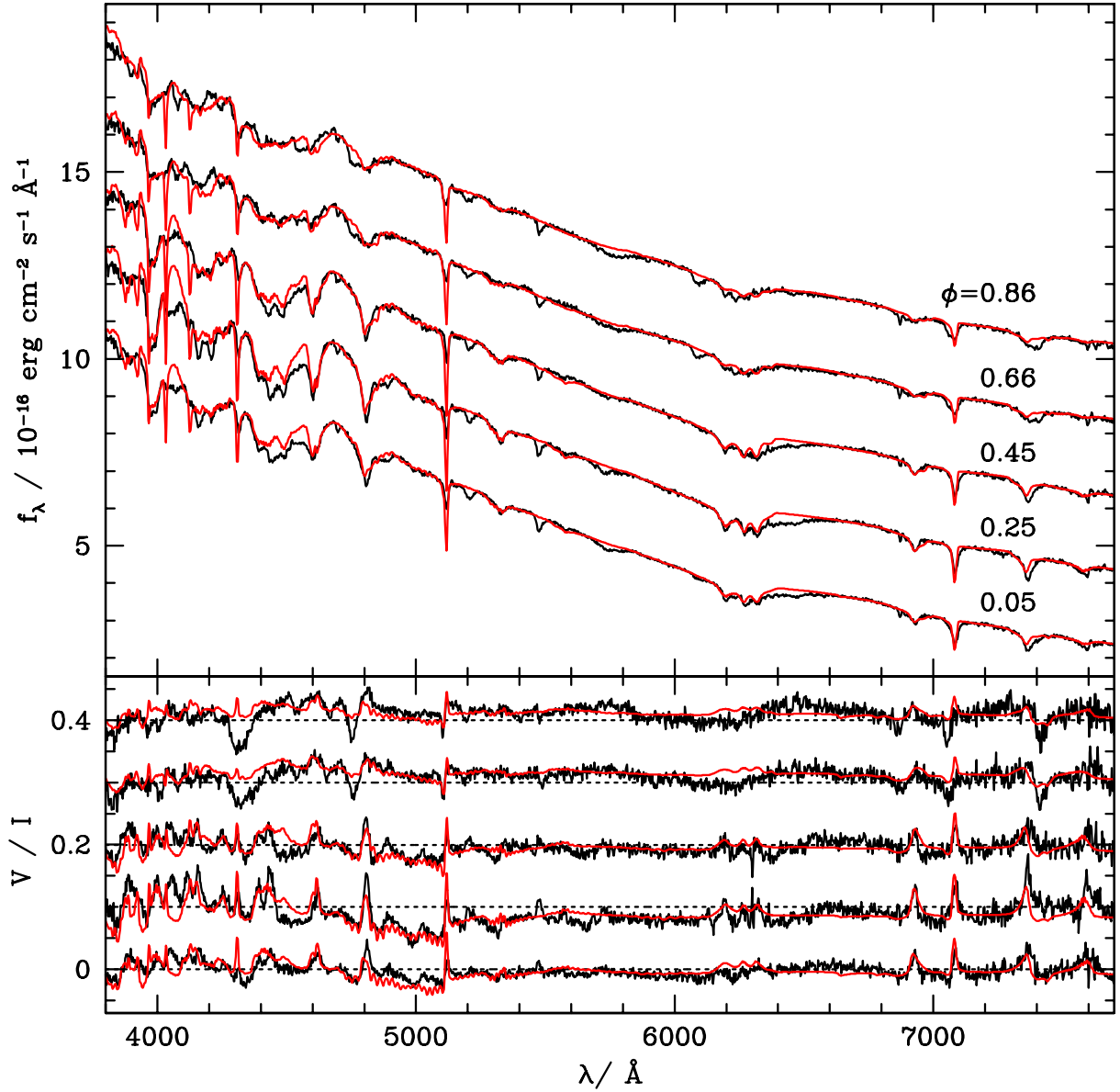


**Figure 4.4:** Observed spectra of PG 1015+014 (black curves) and best-fit synthetic spectra (red curves) using a superposition of three individually off-centred, non-aligned dipoles. The upper four flux (circular polarization) spectra have been shifted for clarity by 2, 4, 6, and 8 ( $0.1$ ,  $0.2$ ,  $0.3$ , and  $0.4$ ) units in  $f_\lambda$  ( $V/I$ ).

(Faßbinder & Schweizer 1996; Burleigh et al. 1999). Lines of such type have not been included in the atomic data tables used for the computation of our synthetic model spectra and, consequently, cannot be reproduced by our fits. They are possibly responsible for the sharp line features at  $5200 \text{ \AA}$  and  $5475 \text{ \AA}$  and the washed out feature at  $5750 \text{ \AA}$ , which are not explained by our models (Figs. 4.4 and 4.6).

Another theoretical uncertainty arises from the simplified treatment of the field-dependent bound-free and free-free transitions as described in Jordan (1992). For the case of Grw +70°8247 with



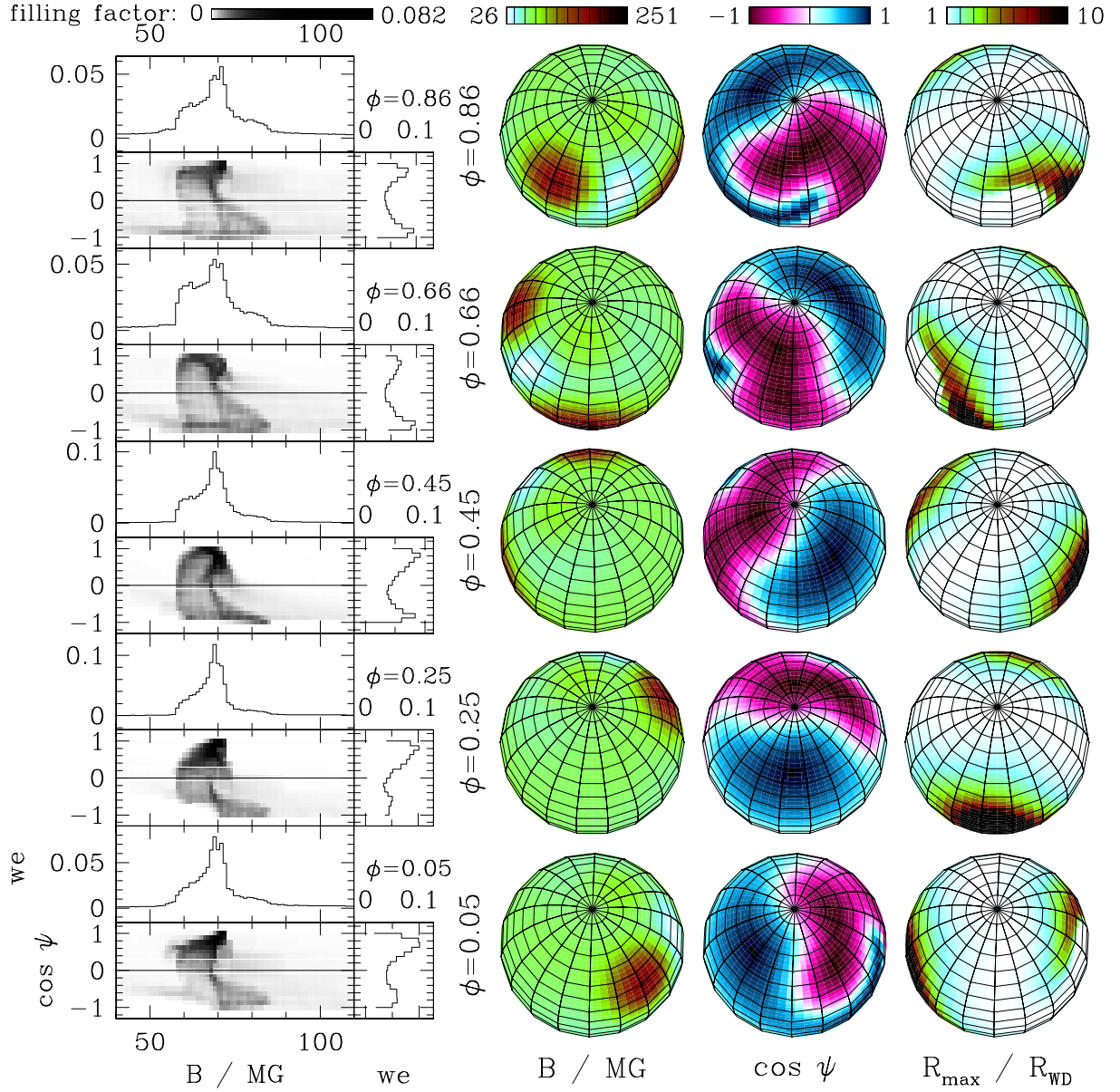


**Figure 4.5:** Zeeman tomographic analysis of the magnetic field configuration of PG 1015+014 using a superposition of three individually off-centred, non-aligned dipoles. *Left panel:*  $B$ - $\psi$  diagram, *right panel:* absolute value of the surface magnetic field, cosine of the angle  $\psi$  between the magnetic field direction and the line of sight, and maximum radial distance reached by field lines in units of the white dwarf radius.

$B \simeq 320$  MG, [Jordan & Merani \(1995\)](#) have shown that a more consistent but numerically extremely expensive treatment of the continuum opacities can yield slightly different results for the polarization. We regard the uncertainties arising from both potential error sources as relatively small at fields of  $\simeq 80$  MG, but slight deviations from our synthetic spectra cannot be ruled out.

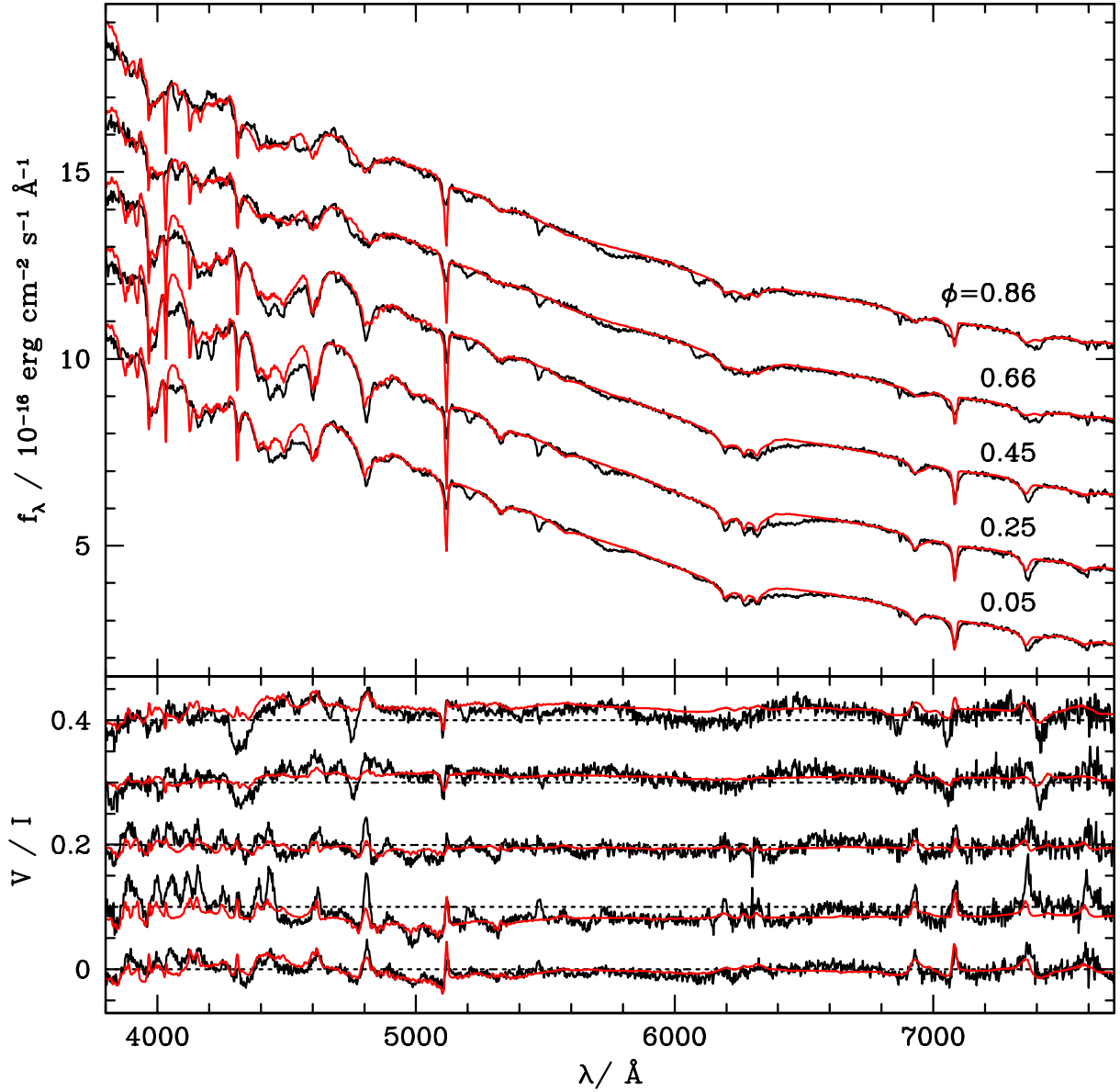


**Figure 4.6:** Observed spectra of PG 1015+014 (black curves) and best-fit synthetic spectra (red curves) for a truncated multipole expansion up to degree  $l = 4$ . For clarity, the upper four flux (polarization) spectra have been shifted upwards by 2, 4, 6, and 8 ( $0.1$ ,  $0.2$ ,  $0.3$ , and  $0.4$  units in  $f_\lambda$  ( $V/I$ )).

## 4.6 Discussion

In this work, we have analysed high-quality spectropolarimetric data of PG 1015+014 covering a whole rotational period with the Zeeman tomography code described in Papers I and II. We have achieved good fits to the observations, but require a magnetic field geometry that is significantly more complex than the popular assumption of centred or moderately offset dipoles and quadrupoles proposed by several authors in the past (Wickramasinghe & Ferrario 2000, and

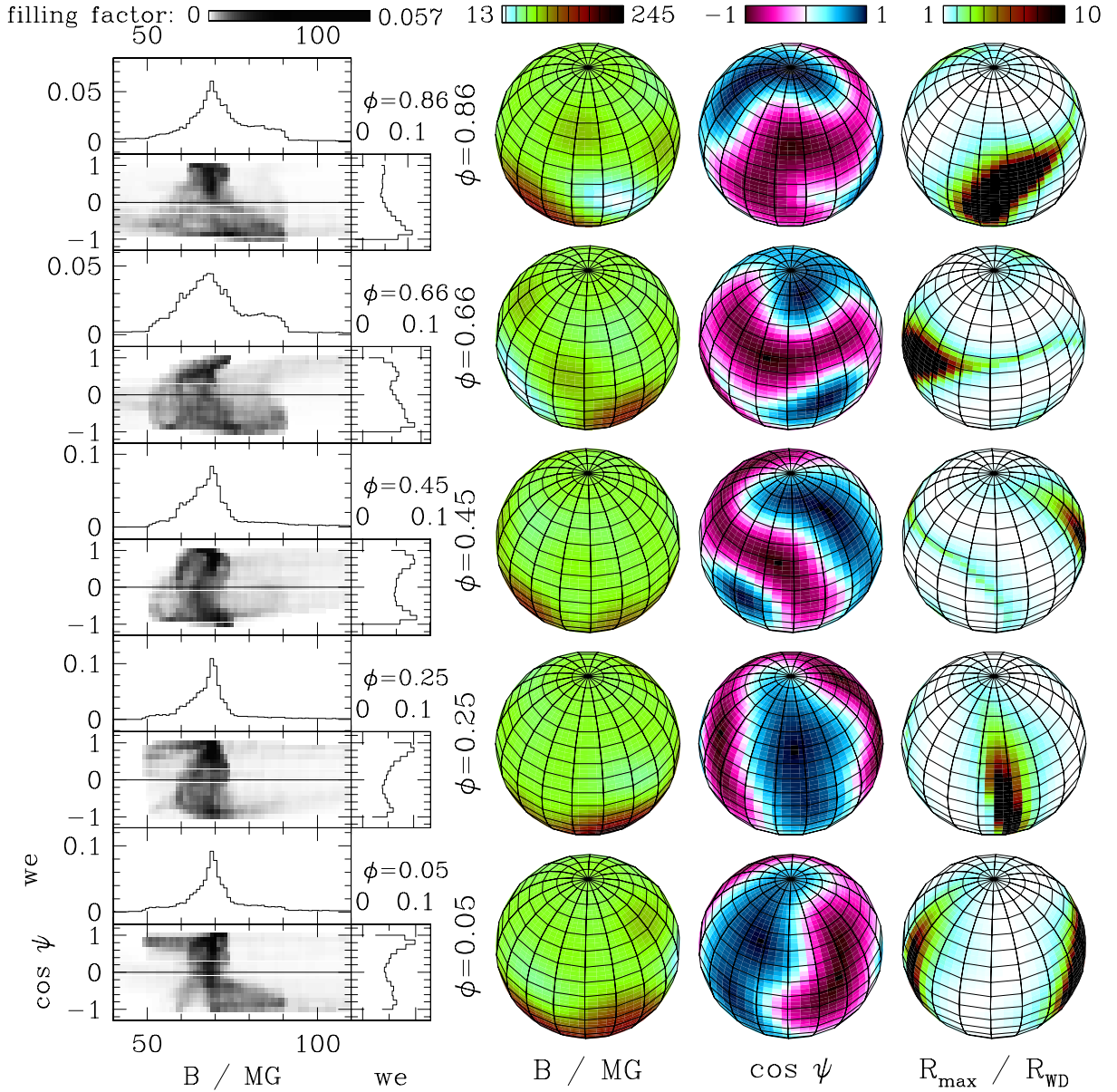


**Figure 4.7:** Zeeman tomographic analysis of the magnetic field configuration of PG 1015+014 using a truncated multipole expansion up to degree  $l = 4$ . *Left panel:*  $B$ - $\psi$  diagram, *right panel:* absolute value of the surface magnetic field, cosine of the angle  $\psi$  between the magnetic field direction and the line of sight, and maximum radial distance reached by field lines in units of the white dwarf radius.

references therein). In fact, the magnetic field structure of PG 1015+014 is even more complex than that derived for HE 1045–0908 (Paper II) and can be successfully modelled by two different parametrizations: On the one hand, we used a hybrid model of off-centred, tilted zonal ( $m = 0$ ) components, and on the other hand, a truncated multipole expansion including all  $m \neq 0$  components. Hence, our results further confirm the evidence that the magnetic field structures of MWDs are non-trivial and require higher multipole components for an accurate description. We have

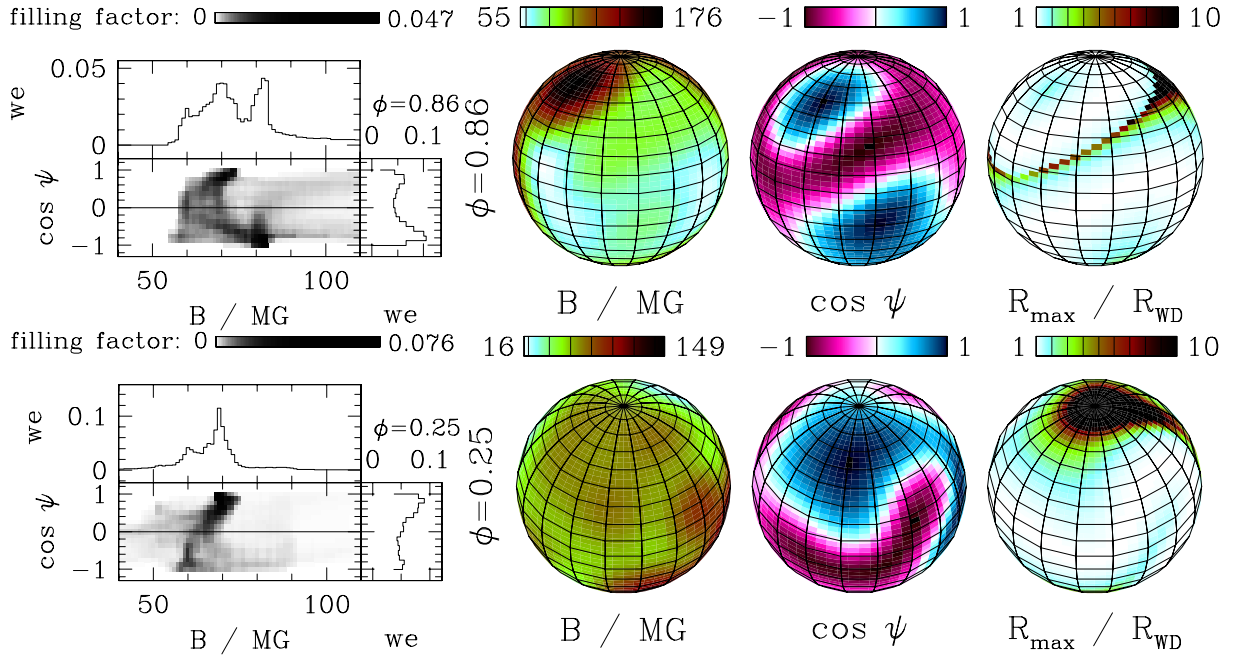


**Figure 4.8:** Best-fit results for individual single phase fits to the Zeeman maximum ( $\phi = 0.86$ , *top panels*) and minimum ( $\phi = 0.25$ , *bottom panels*) phases. The field has been parametrized by a truncated multipole expansion up to degree  $l = 5$  for  $\phi = 0.25$ , and up to  $l = 4$  for  $\phi = 0.86$ . *Left panels:*  $B$ - $\psi$  diagram, *right panels:* absolute value of the surface magnetic field, cosine of the angle  $\psi$  between the magnetic field direction and the line of sight, and maximum radial distance reached by field lines in units of the white dwarf radius.

shown, in particular, that a simple oblique dipole model as devised by Wickramasinghe & Cropper (1988) does not suffice to describe the complex Zeeman absorption features.

Our findings for PG 1015+014 show the difficulties that are inherent to the description of a star’s complex magnetic field geometry with only a few numeric parameters. For this object, an appropriate description requires to quote at least the range of field strengths that contributes effectively to the spectral shape, 50 to 90 MG, and the phase-dependent maxima of the field strength distributions at 69 and 82 MG.

For both parametrization strategies the number of free parameters required for a good fit approaches the maximum number our tomography algorithm can currently handle, and we could reach equivalent quality levels for the best fits. The fits are sufficiently good to be certain that the best-fitting field geometry comes reasonably close to reality, but we could not reach the same high quality of the fits as for HE 1045–0908 (Paper II).

We propose two explanations for the remaining differences between the observations and our best-fitting models: (i) systematic uncertainties in the model spectra arising already in the field regime at  $B \gtrsim 50$  MG, as discussed at the end of Sect. 4.5.2; (ii) insufficient spatial resolution of the magnetic field distribution provided by our field geometry models. Given the limited number of free field parameters and the corresponding limitations regarding the attainable level of complexity in the  $B$ - $\psi$  diagrams, residuals caused by both effects cannot be disentangled.



However, the fact that fits for a single phase were clearly superior to the simultaneous fits for all five phases suggests that there is room for improvement on the side of finer-grained field distributions. Hence, it would be necessary to examine the quality of fits to all phases with an increased number of free parameters before a reliable estimation of the effects of systematic errors in the synthetic model spectra becomes possible.

A different method to tackle this problem would be an approach like that of [Donati et al. \(1994\)](#), who optimised directly the frequency distribution of field strengths and directions. Such an approach has the advantage that a formal best fit to the observed spectra is found which shows the smallest residuals of all possible combinations of database spectra, but a few potential traps should be kept in mind: (i) there is no unique relation between the  $B$ - $\psi$  diagram and the field topology (see Paper I for an example of ambiguous field configurations); (ii) there is no guarantee that the derived  $B$ - $\psi$  diagram corresponds to a field which fits in a globally consistent picture if all rotational phases are regarded; (iii) and it cannot be guaranteed that a distribution of electric currents exists which produces the derived  $B$ - $\psi$  diagram. Remaining discrepancies between the observations and integrated synthetic spectra derived with the method of [Donati et al. \(1994\)](#) would be, nevertheless, a good measure for the magnitude of systematic errors in the model spectra.

Somewhat unfortunately, the two objects we have analysed so far with our Zeeman tomography code both have equal  $T_{\text{eff}}$  (Paper II and this work). It would be desirable to examine the magnetic field geometries of MWDs for a broader range of effective temperatures in order to search for potential effects of a secular field evolution as a function of cooling age.

The outcome of the first three data releases of the *Sloan Digital Sky Survey* (SDSS) has nearly tripled the number of known MWDs. The multitude of newly found objects covers a broad range of effective temperatures and surface dipole field strengths ([Gänsicke et al. 2002](#); [Schmidt et al. 2003](#); [Vanlandingham et al. 2005](#)). Several new objects with  $B > 200$  MG have been found, while the majority of objects is found in the low-field regime with  $B < 20$  MG. The SDSS objects provide a vast hunting ground for further systematic studies of the field geometry of MWDs. The SDSS has also nearly doubled the number of helium-rich MWDs and an interesting option is the extension of our Zeeman tomography technique to the synthesis of their spectra. Calculations of the atomic parameters for He are available now and first applications to helium-rich MWDs are available ([Jordan et al. 2001](#); [Wickramasinghe et al. 2002](#)).

Another promising avenue of research is the study of accreting MWDs in close mass-transferring binaries. In the following papers of this series, we will investigate the magnetic field structures of the accreting MWDs in magnetic cataclysmic variables.

## 4.7 Acknowledgements

This work was supported in part by BMBF/DLR grant 50 OR 9903 6. BTG was supported by a PPARC Advanced Fellowship.



## 5 Conclusions and Outlook

The intention of this work is to gain insight into the properties of magnetic fields on magnetic white dwarfs (MWDs). For that purpose, a method to derive the surface field geometry from phase-resolved optical Zeeman spectra has been developed. Since the determination of the field distribution on the (two-dimensional) stellar surface from a time series of (one-dimensional) spectra is analogous to tomographical methods used in other fields of research (e.g., the well-known CT and PET techniques in medicine), the term ‘Zeeman tomography’ was coined for this new type of analysis. The algorithm was tested on synthetic data sets with artificial noise and yielded promising results (Chapter 2). In particular, the observational prerequisites for a successful application of the method could be determined, namely the need of high-quality phase-resolved flux and circular polarization spectra with  $S/N \simeq 50\text{--}100$  for the individual flux spectra. Given the intrinsic faintness of white dwarfs, 8-m class telescopes equipped with instruments capable of recording circular polarization are required to obtain data of such quality. Fortunately, we were able to obtain appropriate data for two objects, HE 1045–0908 and PG 1015+014, with the best instrument available world-wide at that time, the FORS1 spectrograph at the ESO VLT.<sup>1</sup>

The analyses of these two objects are the first systematic determinations of the magnetic field structure of MWDs based on phase-resolved optical Zeeman spectra including the circular polarization. The best fits reproduce the observed spectra with unprecedented accuracy and yield the most detailed picture of the surface field that could be obtained so far. Since in principle different field geometries can lead to almost identical spectra, absolute knowledge on the true field topology can never be achieved. However, our stepwise approach of starting at the simplest possible fields and gradually increasing the degree of complexity ensures that we find the simplest and, according to *Occam’s razor*, most probable field which is compatible with the observations. For HE 1045–0908, the reliability of our results is slightly affected by the incompleteness of our data set which leaves the rotational period somewhat unconstrained, but we are confident that our findings come close to reality given the very good match of the best-fitting spectra to the observational data. In the case of PG 1015+014, larger deviations between our best fits and the observations remain. As discussed in Sect. 4.6, these are probably due to additional spatial small-scale structure of the magnetic field which cannot be resolved by our geometrical models for the field.

This thesis was inspired by the pioneering work of Donati et al. (1994), who presented a different approach to the same problem which they called the ZEBRA method.<sup>2</sup> These authors also use a pre-computed database of synthetic model spectra that are computed on a two-dimensional parameter grid for a fixed effective temperature of 20 000 K,  $\log g = 8$ , and viewing angle  $\mu = 2/3$ . The free parameters are the transverse ( $B_t$ ) and longitudinal ( $B_l$ ) component of the vector of

---

<sup>1</sup> Part of the FORS1 spectrograph was built in the mechanical workshop of the University Observatory Göttingen. The observational data analysed in this thesis have been taken in guaranteed time allocated to the cooperation partners.

<sup>2</sup> ZEBRA is an acronym for ZEeman BRoadening Analysis of magnetic white dwarfs.



magnetic field strength relative to the line of sight. The graphical representation of such a matrix of parameters is referred to as ZEBRA diagram by the authors. The choice of parameters is analogous to our description using the absolute value  $B$  and the direction cosine  $\cos\psi$ , and the ZEBRA diagrams are analogous to our  $B$ - $\psi$  diagrams. In the approach of Donati et al., a fit to a reference spectrum used as input for the routine is performed through the determination of optimal weights for the database spectra, such that their superposition yields a best fit to the input spectrum. Since no unique solution can be expected for insufficiently constrained inverse problems of this type, a maximum entropy regularization method is applied to ensure a smooth solution.

This method has the advantage that precise information on the statistical properties of the underlying field (i.e., the distribution of field strengths and directions) can be gathered, but no attempts are made to relate this information to a specific field geometry. In particular, the spatial information contained in a time series of spectra that represent consecutive rotational phases is not evaluated. For that purpose, the introduction of a geometrical field model described by a set of parameters – in analogy to our approach – would be required as an additional step. In the article in question, the method of Donati et al. has only been applied to synthetic input spectra with artificial noise, not to real observations. A ZEBRA-type analysis of our spectropolarimetric data of HE 1045–0908 and PG 1015+014 would be an ideal supplement to our tomographic studies, especially for PG 1015+014, because it could help to resolve remaining uncertainties in the  $B$ - $\psi$  diagrams that most likely arise from our truncation of the multipole expansion.

Dipole models including an inclination angle of the dipole axis relative to the line of sight and an optional off-centre shift in the direction of the dipole axis have been used frequently as first-order estimations of the magnetic field geometry based on single spectra. In this context, single spectra can either be taken from a temporal sequence in order to investigate one specific rotational phase (cf. our single phase fits discussed in Sect. 4.5.2), or, more frequently, they originate from singular observations, possibly with no further information on rotation available. An analysis of the latter type has been performed, e.g., for the newly discovered MWDs in the *Sloan Digital Sky Survey* (Schmidt et al. 2003; Vanlandingham et al. 2005). There are several reasons why dipole models are worth to be considered, at least as a starting point towards more complex geometries: Their geometry is mathematically simple and easy to visualise. Furthermore, simple theories of the secular field evolution suggest that the higher-order multipole components decay faster than the dipole, so the field geometry, according to these theories, should converge to a largely dipolar pattern on an evolutionary time scale (Wendell et al. 1987). In other theoretical studies, however, it has been argued that under certain circumstances higher-order components can be enhanced and exceed the dipole in magnitude if a strong toroidal component is present and couples back to the poloidal components (Muslimov et al. 1995).<sup>3</sup> The field geometries found for the two objects of our study differ strongly from pure centred or off-centred dipoles. While the field of HE 1045–0908 is dominated by a quadrupole component, we have shown that in the case of PG 1015+014 the octupole and probably even higher multipoles are essential to describe the field topology. With  $T_{\text{eff}} = 10\,000\text{ K}$ , the evolutionary age of both objects is  $\simeq 0.6\text{ Gyr}$  (Wood 1995). Over this time interval, no significant decay of the higher-order multipoles is expected, and, hence, no conclusion can be drawn concerning the Muslimov et al. theory. Clearly, additional theoretical studies of this intricate subject are needed.

---

<sup>3</sup> A possible normalisation error which affects the decay times quoted in the work of Muslimov et al. (1995) has been reported by Cumming (2002).

So far we have conducted authoritative Zeeman tomographic analyses only for isolated (non-accreting) magnetic white dwarfs. It is a promising avenue of research to apply this method also to the central stars of magnetic cataclysmic variables (AM Her stars or polars). An advantage of this type of studies is that the spin of the white dwarfs in magnetic cataclysmic variables is synchronised with the orbital rotation, i.e., due to their orbital periods of several hours these objects are good candidates for recording rotation-phase resolved Zeeman spectra. However, there are also major difficulties. Polars contain accreting white dwarfs, and Zeeman studies are possible only at times when accretion has temporarily ceased (low state), because in the accreting (high) state Zeeman features will be obliterated by cyclotron radiation. Furthermore, the contribution of the secondary star has to be removed using a suitable template spectrum, a process which can distort the spectral shape in the  $H\alpha$  region.

Zeeman tomographic analyses of polars should in principle provide the possibility to check the constraints placed upon the accretion geometry by high-state observations, and to determine the location and shape of the accretion region as given by foot points of accreting field lines. Our preliminary studies for several AM Her stars, however, have not yet succeeded in finding a consistent description for the accretion geometry. In analogy to the case of PG 1015+014, this might be due to insufficient spatial resolution of our magnetic models.

It would be interesting to analyse a substantial number of polars in order to answer the question if the degree of complexity of the magnetic fields found for white dwarfs in cataclysmic variables differs from the one measured in non-accreting MWDs, and to detect possible effects of accretion on the field geometry. Such an effect is made responsible for the secular decrease in magnetic field strength of accreting neutron stars.

Returning to the isolated MWDs, it should be noticed that the *Sloan Digital Sky Survey* has yielded so far a large number of suitable candidate objects for further tomographic studies, covering a broad range of effective temperatures and magnetic field strengths. Given the capabilities of modern telescopes and spectrographs, Zeeman tomography provides a good means to gain further insight into the properties of magnetic fields of magnetic white dwarfs and the role they play in stellar evolution.



## **A Additional fit results for HE 1045–0908**

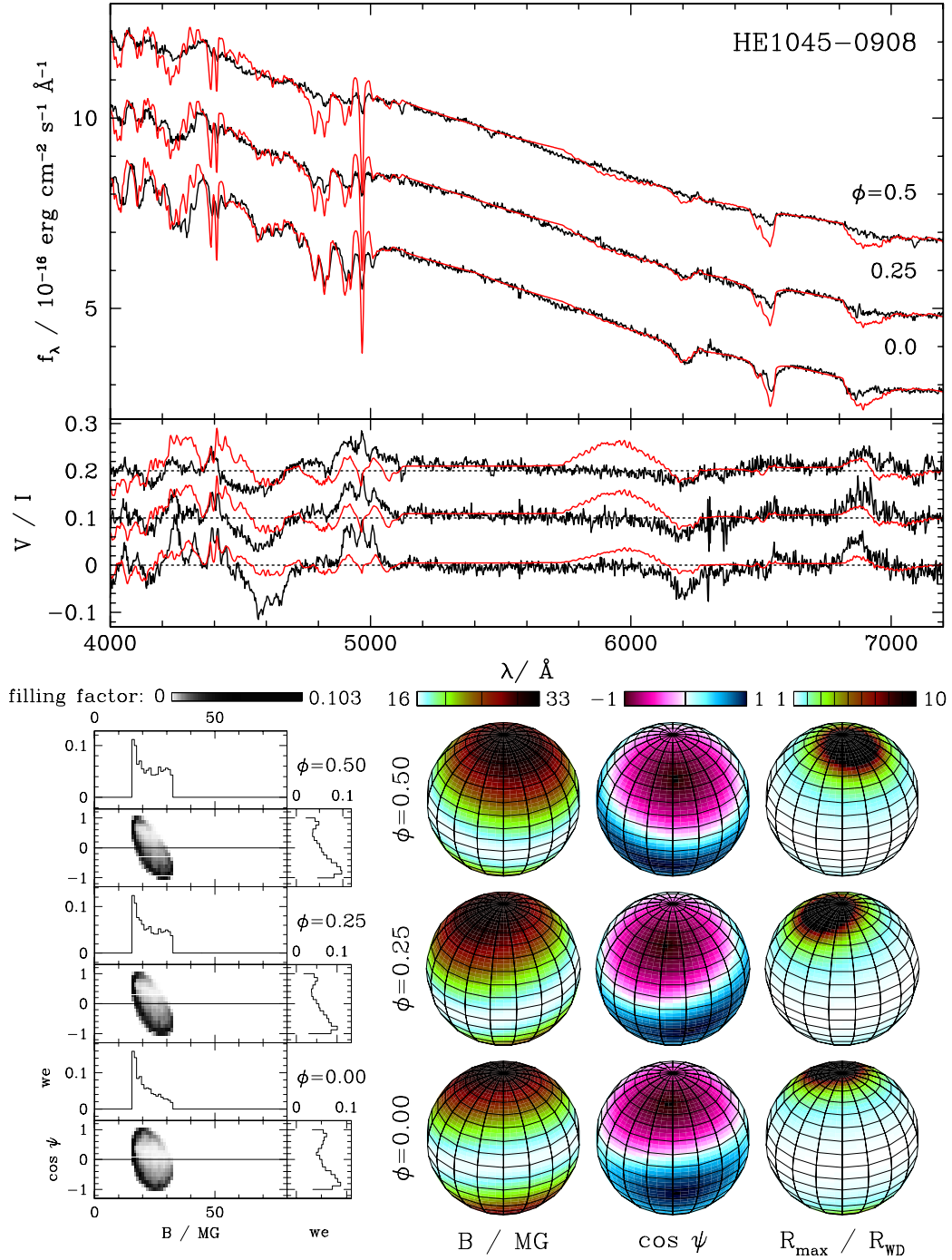


**Figure A.1:** Zeeman tomographic analysis of the magnetic field configuration of HE 1045–0908 using a centred dipole model. *Top:* Observed (black curves) and best-fit synthetic spectra (red curves). The uppermost two flux (circular polarization) spectra have been shifted for clarity by 2 and 4 (0.1 and 0.2) units in  $f_\lambda$  ( $V/I$ ). The quoted phases refer to case (i) with  $P_{\text{rot}} = 2.7 \text{ h}$ . *Bottom left:*  $B$ - $\psi$  diagram, *bottom right:* absolute value of the surface magnetic field, cosine of the angle  $\psi$  between the magnetic field direction and the line of sight, and maximum radial distance reached by field lines in units of the white dwarf radius.

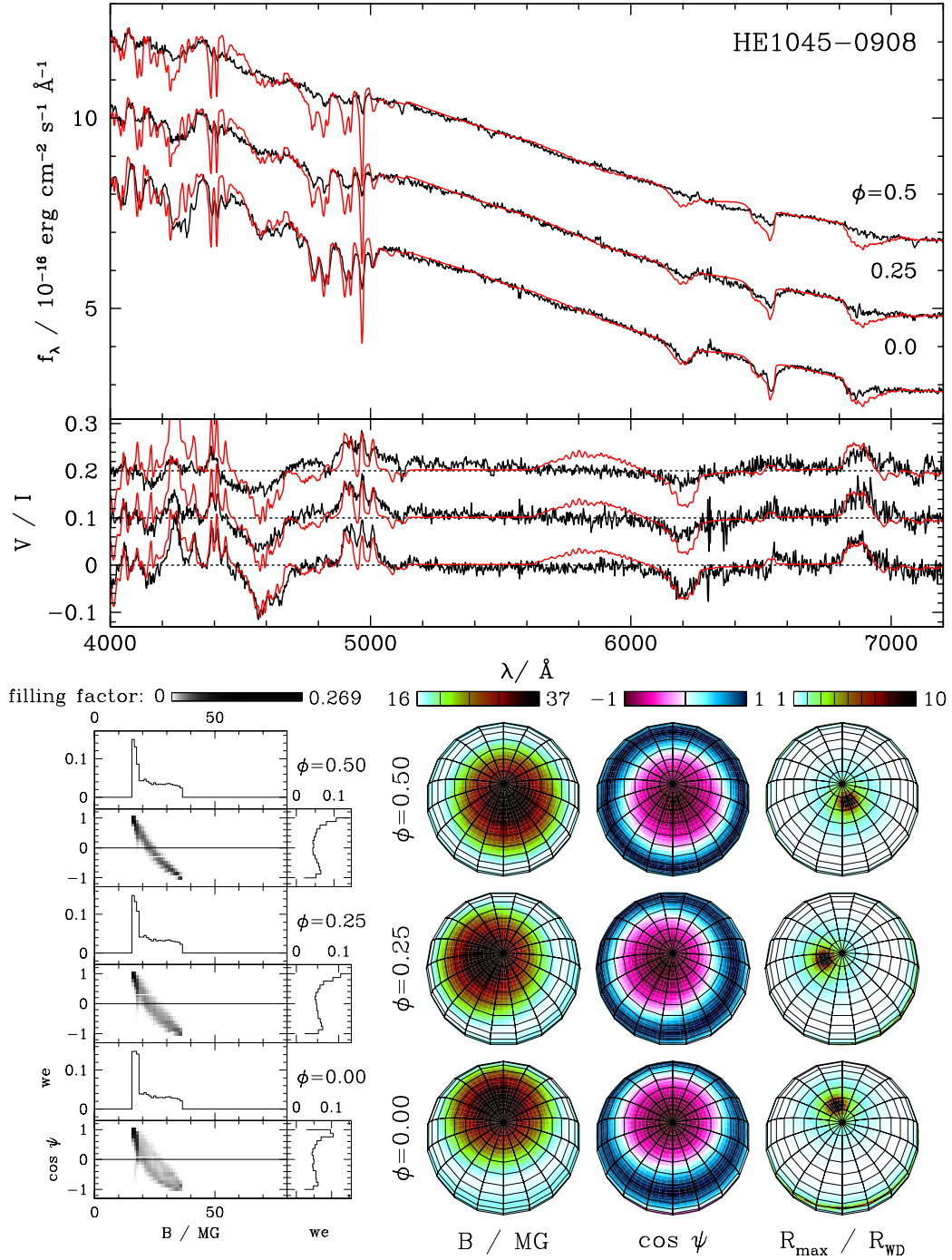


**Figure A.2:** Zeeman tomographic analysis of the magnetic field configuration of HE 1045-0908 using a centred quadrupole model. *Top:* Observed (black curves) and best-fit synthetic spectra (red curves). The uppermost two flux (circular polarization) spectra have been shifted for clarity by 2 and 4 (0.1 and 0.2) units in  $f_\lambda$  (V/I). The quoted phases refer to case (i) with  $P_{\text{rot}} = 2.7 \text{ h}$ . *Bottom left:*  $B$ - $\psi$  diagram, *bottom right:* absolute value of the surface magnetic field, cosine of the angle  $\psi$  between the magnetic field direction and the line of sight, and maximum radial distance reached by field lines in units of the white dwarf radius.

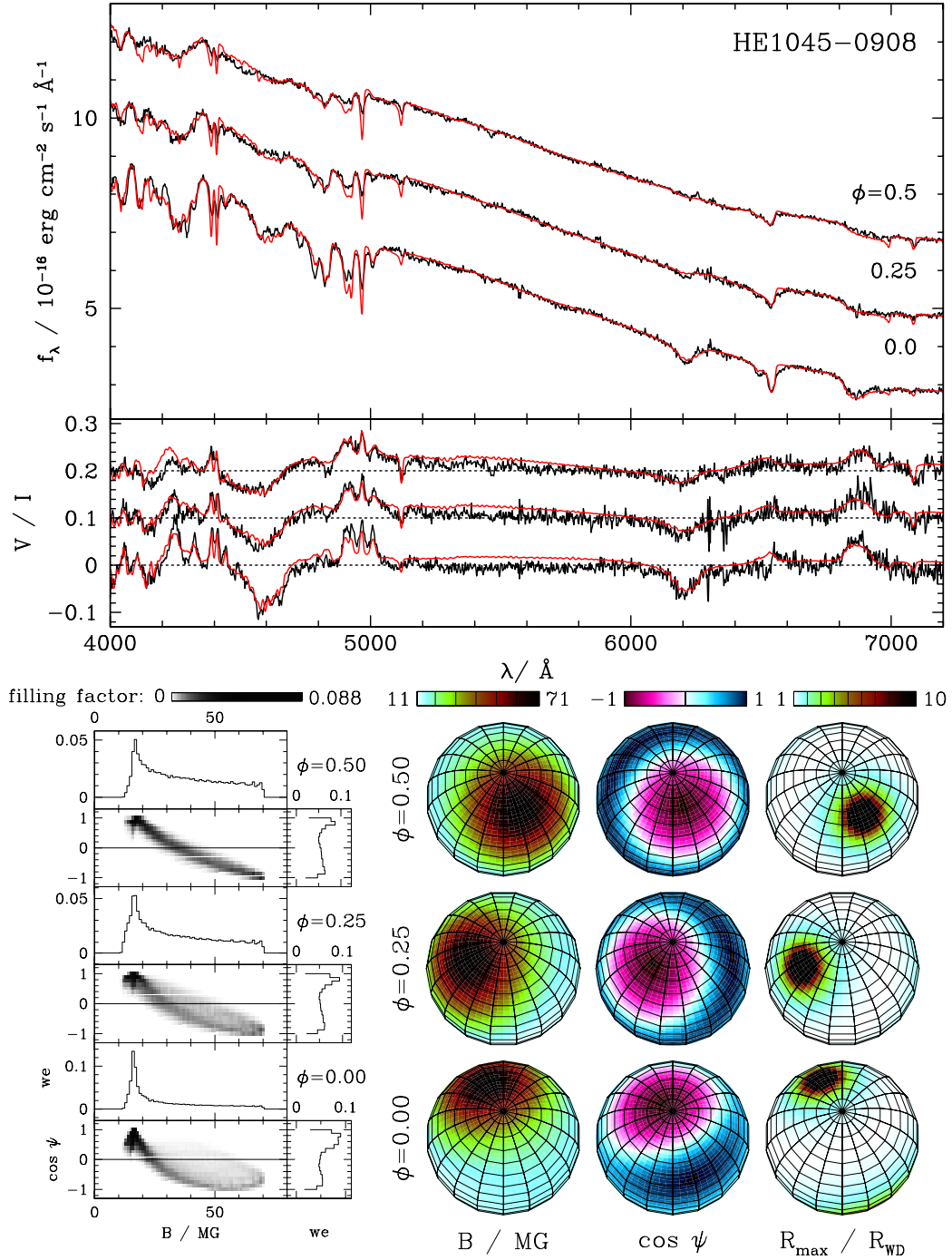


**Figure A.3:** Zeeman tomographic analysis of the magnetic field configuration of HE 1045–0908 using an off-centred dipole model. *Top:* Observed (black curves) and best-fit synthetic spectra (red curves). The uppermost two flux (circular polarization) spectra have been shifted for clarity by 2 and 4 ( $0.1$  and  $0.2$ ) units in  $f_\lambda$  ( $V/I$ ). The quoted phases refer to case (i) with  $P_{\text{rot}} = 2.7 \text{ h}$ . *Bottom left:*  $B$ - $\psi$  diagram, *bottom right:* absolute value of the surface magnetic field, cosine of the angle  $\psi$  between the magnetic field direction and the line of sight, and maximum radial distance reached by field lines in units of the white dwarf radius.



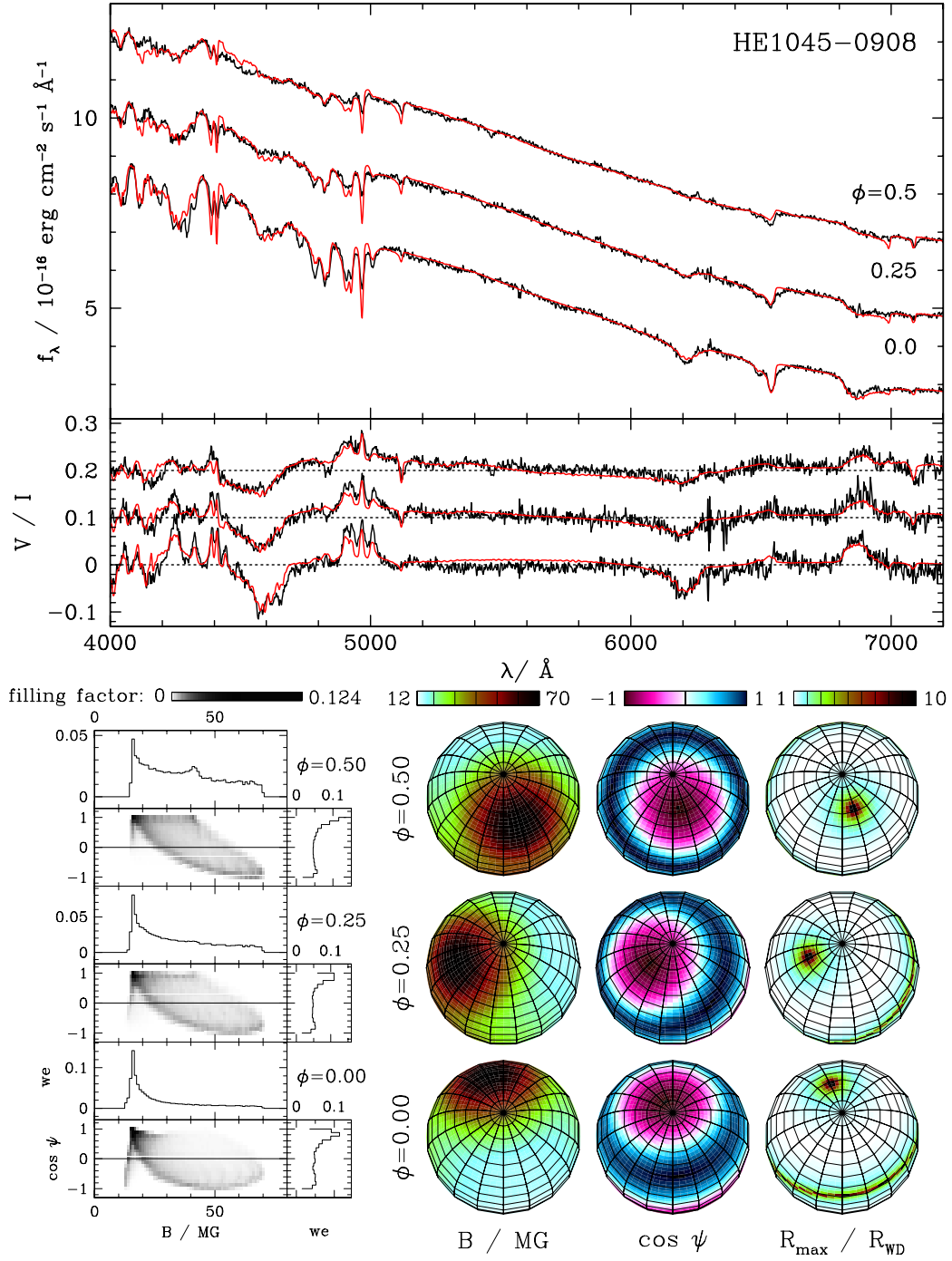


**Figure A.4:** Zeeman tomographic analysis of the magnetic field configuration of HE 1045-0908 using an off-centred quadrupole model. *Top:* Observed (black curves) and best-fit synthetic spectra (red curves). The uppermost two flux (circular polarization) spectra have been shifted for clarity by 2 and 4 (0.1 and 0.2) units in  $f_{\lambda}$  ( $V/I$ ). The quoted phases refer to case (i) with  $P_{\text{rot}} = 2.7$  h. *Bottom left:*  $B$ - $\psi$  diagram, *bottom right:* absolute value of the surface magnetic field, cosine of the angle  $\psi$  between the magnetic field direction and the line of sight, and maximum radial distance reached by field lines in units of the white dwarf radius.



## **B Additional fit results for PG 1015+014**

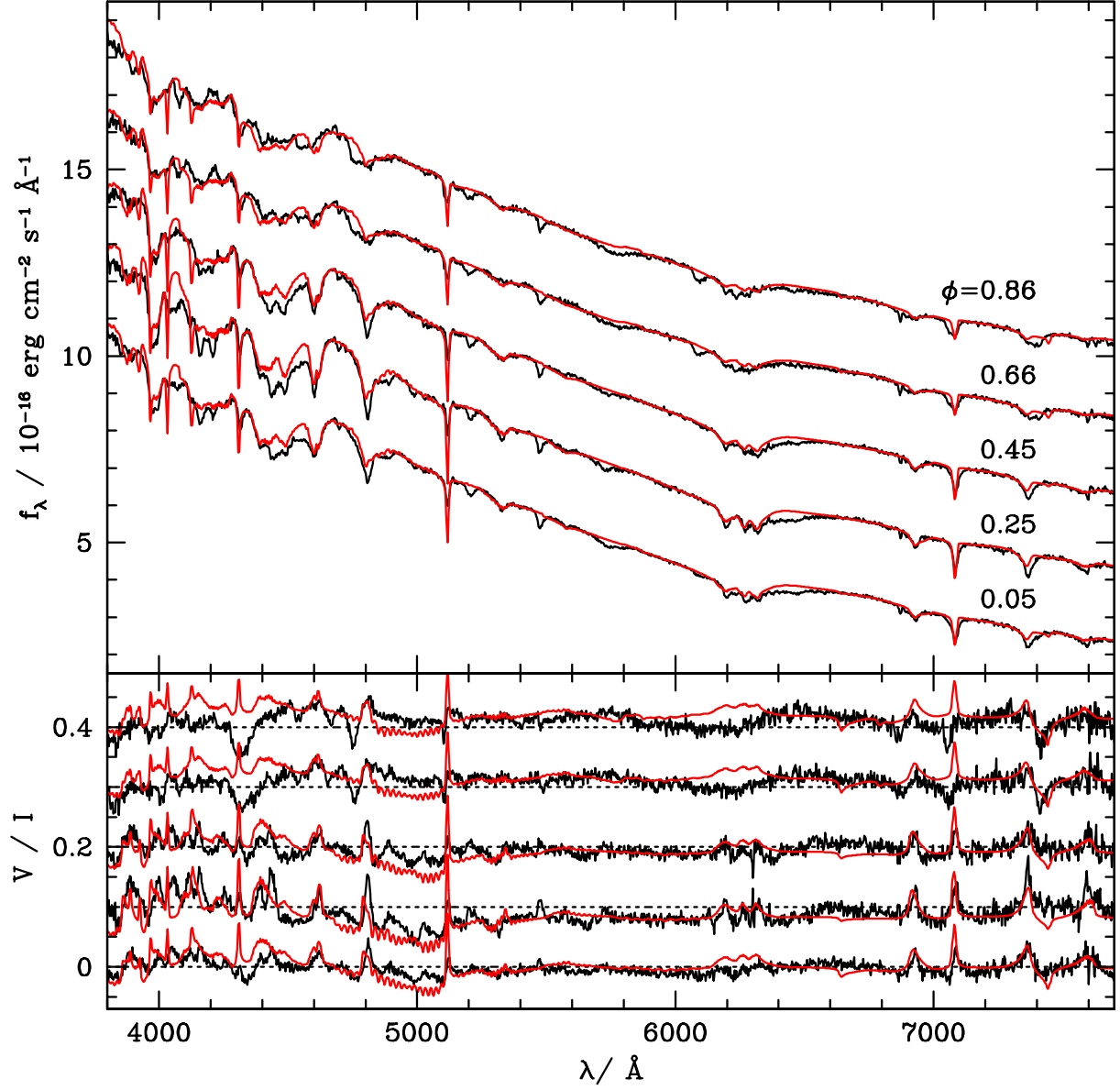


**Figure B.1:** Observed (black curves) and best-fit synthetic spectra (red curves) for PG 1015+014 using an off-centred dipole model. The uppermost four flux (circular polarization) spectra have been shifted for clarity by 2, 4, 6, and 8 (0.1, 0.2, 0.3, and 0.4) units in  $f_\lambda$  ( $V/I$ ).

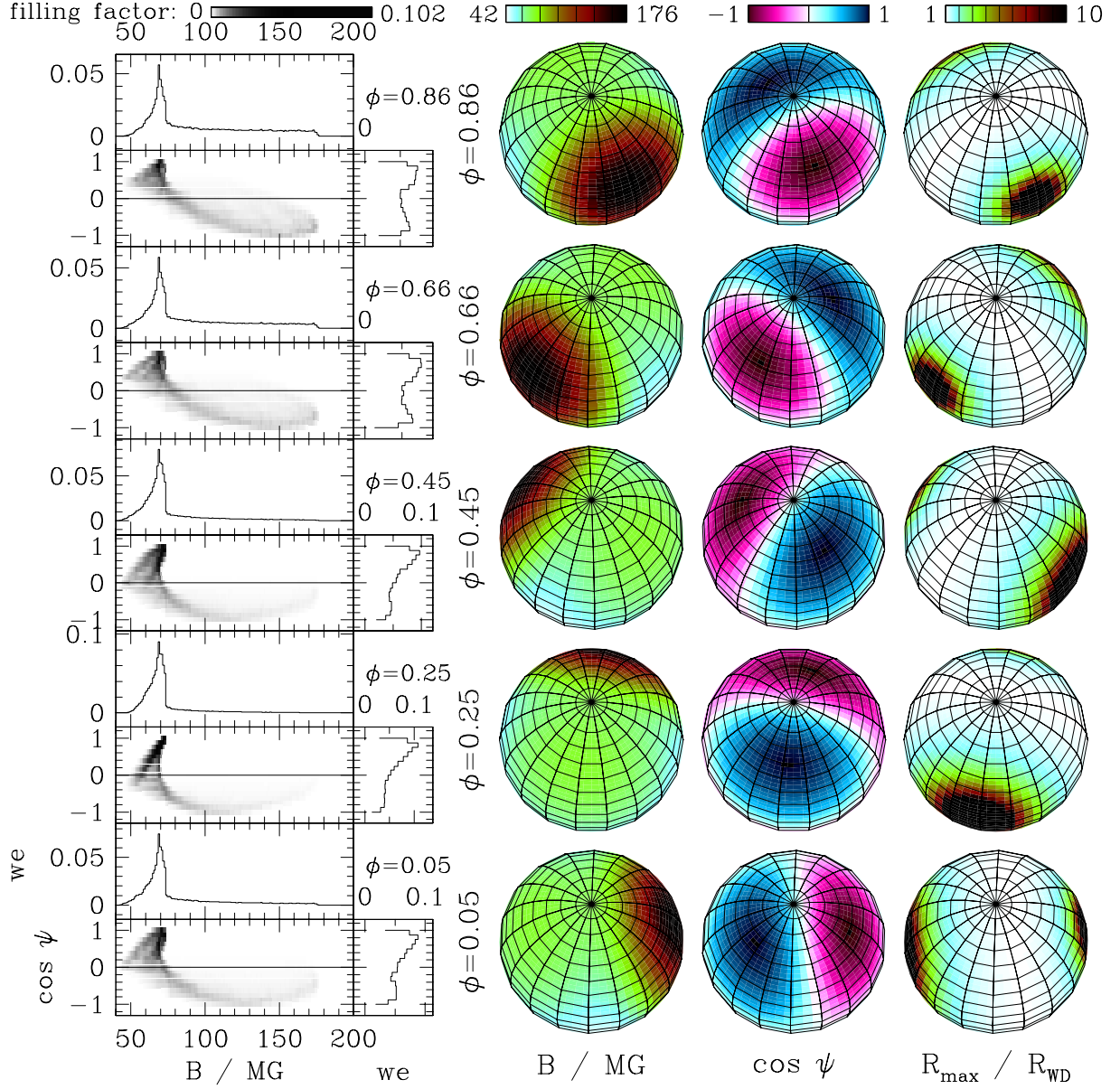


**Figure B.2:** Zeeman tomographic analysis of the magnetic field configuration of PG 1015+014 using an off-centred dipole model. *Left panel:*  $B$ - $\psi$  diagram, *right panel:* absolute value of the surface magnetic field, cosine of the angle  $\psi$  between the magnetic field direction and the line of sight, and maximum radial distance reached by field lines in units of the white dwarf radius.

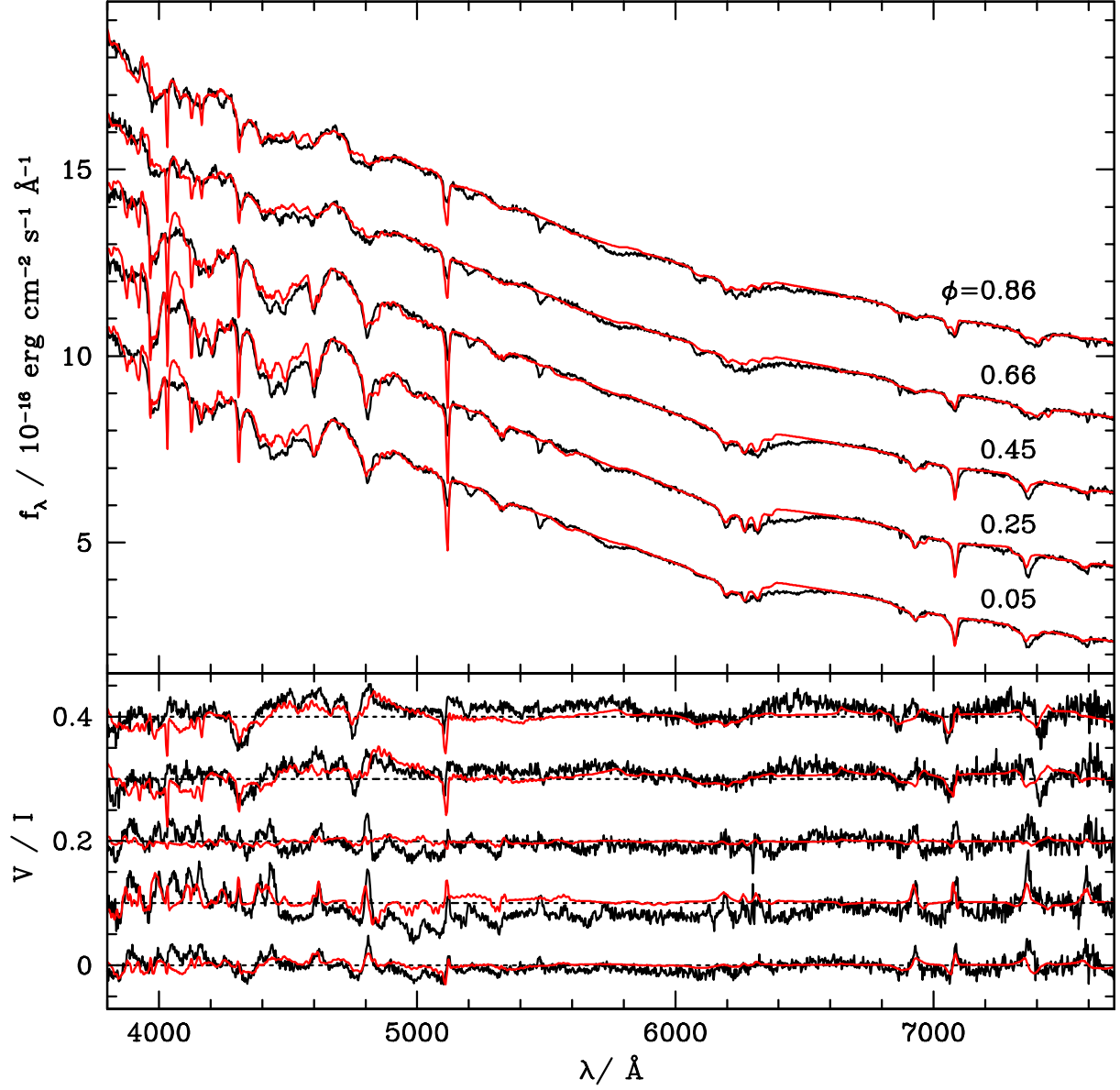


**Figure B.3:** Observed (black curves) and best-fit synthetic spectra (red curves) for PG 1015+014 using a centred, non-aligned combination of dipole, quadrupole, and octupole components. The uppermost four flux (circular polarization) spectra have been shifted for clarity by 2, 4, 6, and 8 (0.1, 0.2, 0.3, and 0.4) units in  $f_\lambda$  ( $V/I$ ).



**Figure B.4:** Zeeman tomographic analysis of the magnetic field configuration of PG 1015+014 using a centred, non-aligned combination of dipole, quadrupole, and octupole components. *Left panel:*  $B$ - $\psi$  diagram, *right panel:* absolute value of the surface magnetic field, cosine of the angle  $\psi$  between the magnetic field direction and the line of sight, and maximum radial distance reached by field lines in units of the white dwarf radius.



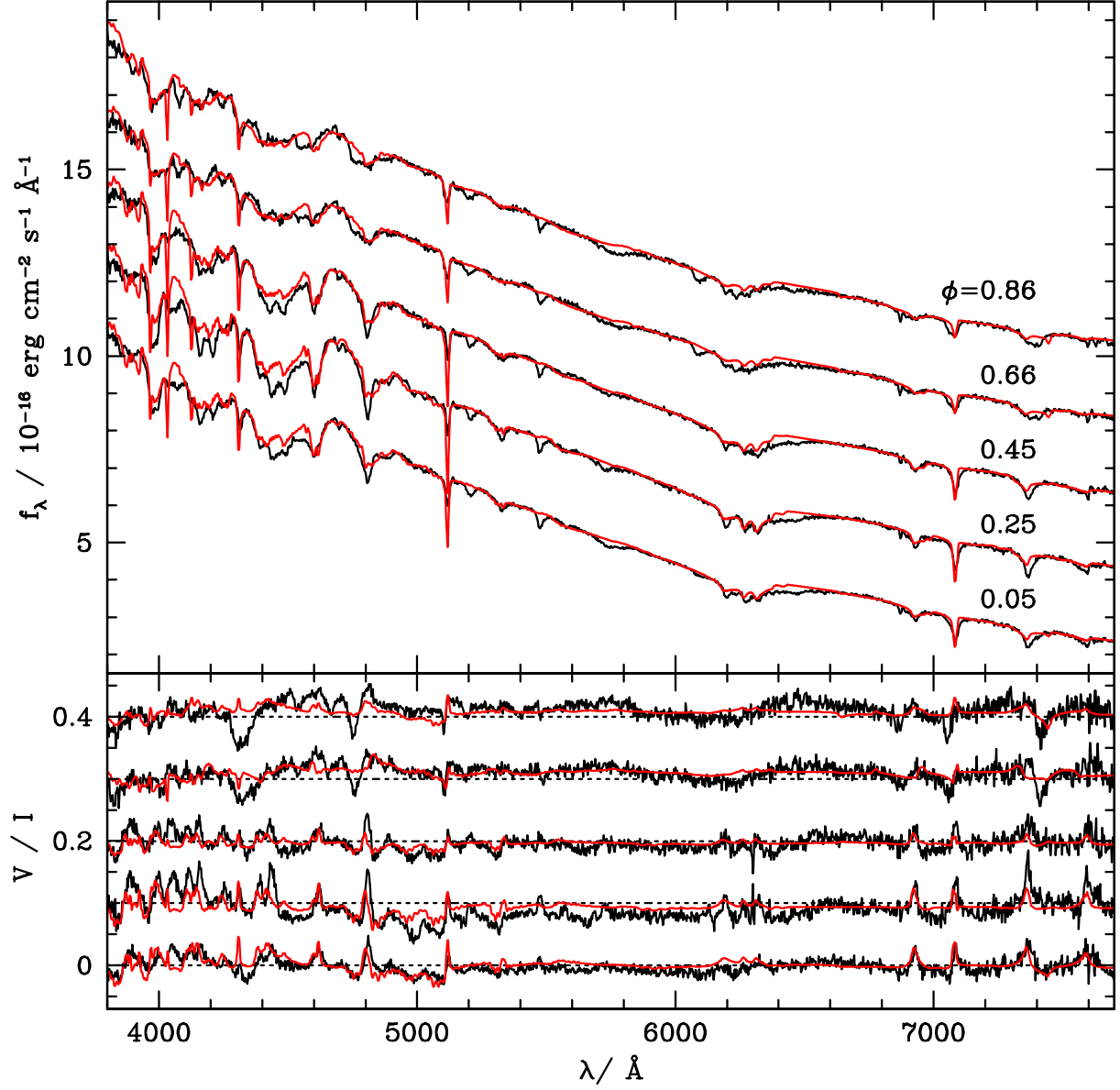


**Figure B.5:** Observed (black curves) and best-fit synthetic spectra (red curves) for PG 1015+014 using an off-centred, non-aligned combination of dipole, quadrupole, and octupole components. The uppermost four flux (circular polarization) spectra have been shifted for clarity by 2, 4, 6, and 8 (0.1, 0.2, 0.3, and 0.4) units in  $f_\lambda$  ( $V/I$ ).

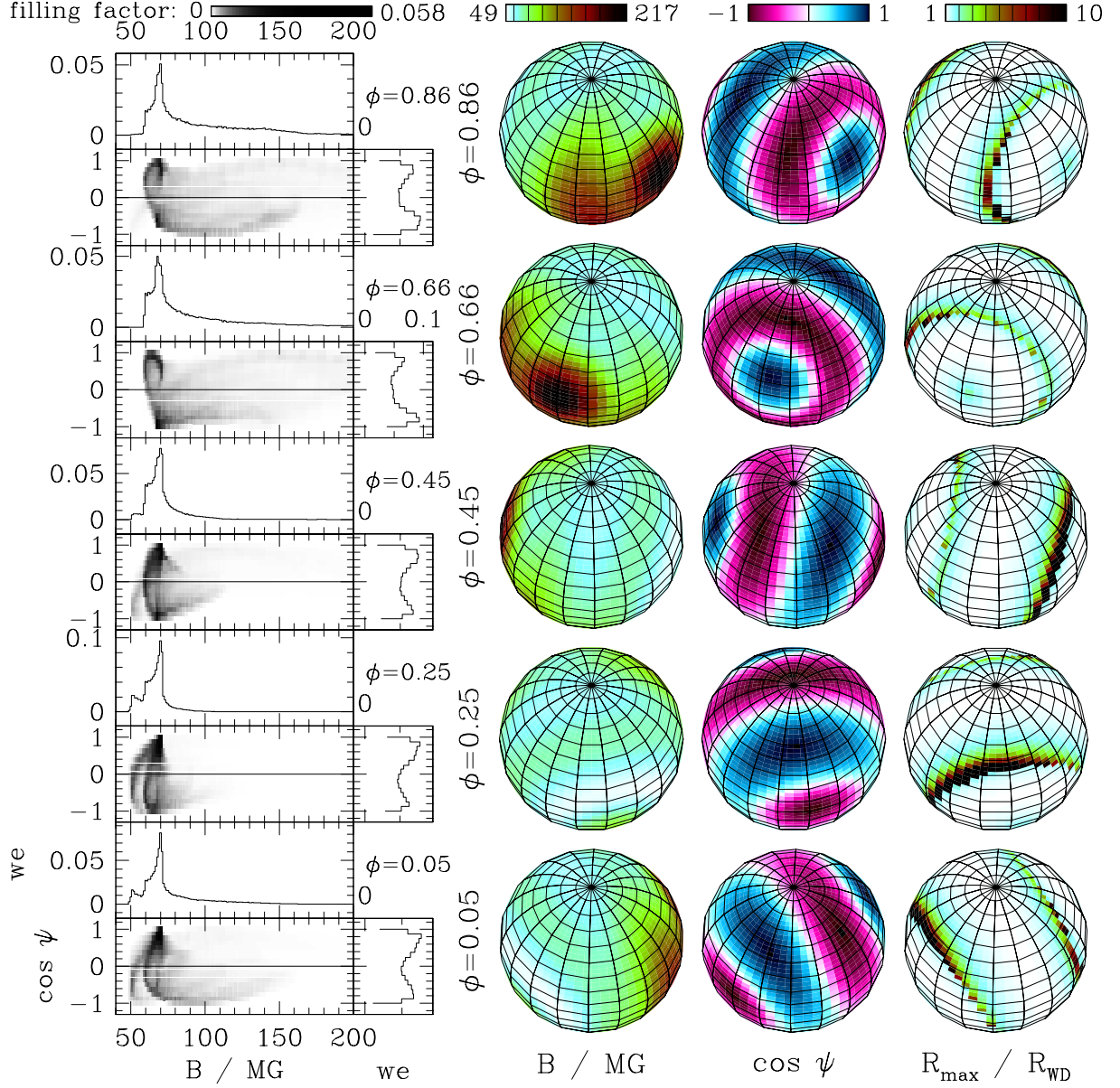


**Figure B.6:** Zeeman tomographic analysis of the magnetic field configuration of PG 1015+014 using an off-centred, non-aligned combination of dipole, quadrupole, and octupole components. *Left panel:*  $B$ - $\psi$  diagram, *right panel:* absolute value of the surface magnetic field, cosine of the angle  $\psi$  between the magnetic field direction and the line of sight, and maximum radial distance reached by field lines in units of the white dwarf radius.



## C MWDcat – an interactive, online catalogue of magnetic white dwarfs

At the *Institut für Astrophysik* in Göttingen, we have set up *MWDcat*, an interactive, online database on magnetic white dwarfs which can be freely accessed via the internet by everyone at the URL <http://mwdcat.org>. The installation of this catalogue is part of a DFG-funded project called *AstroCat*, which is aimed at the development of a software package for the installation of interactive astronomical catalogues of a general type (Kube et al. 2003; Euchner et al. 2004). The AstroCat homepage can be found at <http://astrocat.org>.

Currently, the status of MWDcat is a read-only public demonstration version, i.e., catalogue users cannot add new data to the catalogue. After the official release of MWDcat, which is planned for the 15<sup>th</sup> European Workshop on White Dwarfs (to be held in Leicester/UK, August 7–11<sup>th</sup> 2006), the addition of new data by the registered users – a key feature of the catalogue – will be possible. Instructions how to request a user account for MWDcat are given on the catalogue web site.

The catalogue content as provided by now is taken mainly from the object lists given in Wickramasinghe & Ferrario (2000); Schmidt et al. (2003); and Vanlandingham et al. (2005). Major new contributions to the database can be expected, e.g., from the Data Release 4 of the *Sloan Digital Sky Survey*.



# Bibliography

- ACHILLEOS, N., WICKRAMASINGHE, D. T., LIEBERT, J., SAFFER, R. A. & GRAUER, A. D. (1992) Exploring the peculiar magnetic field of Feige 7. *ApJ*, **396**, 273–288. [3](#)
- AURIÈRE, M., SILVESTER, J., WADE, G. A., BAGNULO, S., DONATI, J.-F., JOHNSON, N., LANDSTREET, J. D., LIGNERES, F. ET AL. (2003) A survey of magnetic Ap/Bp stars for weak longitudinal magnetic fields. *A Peculiar Newsletter*, vol. 39. [4](#)
- AZNAR CUADRADO, R., JORDAN, S., NAPIWOTZKI, R., SCHMID, H. M., SOLANKI, S. K. & MATHYS, G. (2004) Discovery of kilogauss magnetic fields in three DA white dwarfs. *A&A*, **423**, 1081–1094. [2](#), [34](#), [52](#)
- BARSTOW, M. A., BOND, H. E., HOLBERG, J. B., BURLEIGH, M. R., HUBENY, I. & KOESTER, D. (2005) Hubble Space Telescope spectroscopy of the Balmer lines in Sirius B. *MNRAS*, **362**, 1134–1142. [1](#)
- BARSTOW, M. A., JORDAN, S., O'DONOGHUE, D., BURLEIGH, M. R., NAPIWOTZKI, R. & HARROP-ALLIN, M. K. (1995) RE J0317–853: the hottest known highly magnetic DA white dwarf. *MNRAS*, **277**, 971–985. [2](#)
- BECKERS, J. M. (1969) The profiles of Fraunhofer lines in the presence of Zeeman splitting. *Sol. Phys.*, **9**, 372. [9](#)
- BEUERMANN, K. & REINSCH, K. (2002) The high-field magnetic white dwarf LP 790–29: Not a fast rotator. *A&A*, **381**, 487–490. [3](#)
- BHATTACHARYA, D. (1996) The Origin of Millisecond Pulsars. In *IAU Colloq. 160: Pulsars: Problems and Progress*, edited by S. Johnston, M. A. Walker & M. Bailes, no. 105 in ASP Conf. Ser., Astronomical Society of the Pacific, San Francisco. [3](#)
- BORRA, E. F., LANDSTREET, J. D. & MESTEL, L. (1982) Magnetic stars. *ARA&A*, **20**, 191–220. [3](#)
- BRAITHWAITE, J. & SPRUIT, H. C. (2004) A fossil origin for the magnetic field in A stars and white dwarfs. *Nat*, **431**, 819–821. [34](#)
- BROWN, S. F., DONATI, J.-F., REES, D. E. & SEMEL, M. (1991) Zeeman-Doppler Imaging of solar-type and Ap stars IV. Maximum entropy reconstruction of 2D magnetic topologies. *A&A*, **250**, 463–474. [8](#), [27](#)
- BURLEIGH, M. R., JORDAN, S. & SCHWEIZER, W. (1999) Phase-resolved Far-Ultraviolet Hubble Space Telescope Spectroscopy of the Peculiar Magnetic White Dwarf RE J0317–853. *ApJ Lett.*, **510**, L37–L40. [3](#), [10](#), [34](#), [64](#)

- CUMMING, A. (2002) Magnetic field evolution in accreting white dwarfs. *MNRAS*, **333**, 589–602. [34](#), [48](#), [72](#)
- DITTMANN, O. (1995) *Transport polarisierter Strahlung in Medien beliebiger Geometrie*. Dissertation, Ruprecht-Karls-Universität, Heidelberg, Germany. [10](#)
- DONATI, J.-F., ACHILLEOS, N., MATTHEWS, J. M. & WESEMAEL, F. (1994) ZEBRA – ZEeman BRoadening Analysis of magnetic white dwarfs I. Maximum entropy reconstruction of H $\alpha$  profiles. *A&A*, **285**, 285–299. [8](#), [17](#), [28](#), [48](#), [63](#), [69](#), [71](#), [72](#)
- DONATI, J.-F., SEMEL, M. & PRADERIE, F. (1989) Zeeman-Doppler imaging of active stars II. Numerical simulation and first observational results. *A&A*, **225**, 467–478. [8](#)
- EUCHNER, F. (1998) *Multipolanalyse der magnetischen Feldstruktur des Weißen Zwergs in V834 Centauri*. Diplomarbeit, Georg-August-Universität, Göttingen, Germany. [10](#)
- EUCHNER, F., JORDAN, S., BEUERMANN, K., GÄNSICKE, B. T. & HESSMAN, F. V. (2002) Zeeman tomography of magnetic white dwarfs I. Reconstruction of the field geometry from synthetic spectra. *A&A*, **390**, 633–647 (Paper I). [34](#), [35](#), [40](#), [53](#)
- EUCHNER, F., JORDAN, S., REINSCH, K., BEUERMANN, K. & GÄNSICKE, B. T. (2005a) Surface Magnetic Field Distributions of the White Dwarfs PG 1015+014 and HE 1045–0908. In *Proceedings of the 14<sup>th</sup> European Workshop on White Dwarfs*, edited by D. Koester & S. Moehler, no. 334 in ASP Conf. Ser., Astronomical Society of the Pacific, San Francisco. [34](#), [46](#)
- EUCHNER, F., POLLMER, A., GÄNSICKE, B. T., KUBE, J. & BEUERMANN, K. (2004) AstroCat/CVcat: A catalogue on Cataclysmic Variables based on a new framework for online interactive astronomical databases. In *Astronomical Data Analysis Software and Systems XIII*, edited by F. Ochsenbein, M. G. Allen & D. Egret, no. 314 in ASP Conf. Ser., Astronomical Society of the Pacific, San Francisco. [89](#)
- EUCHNER, F., REINSCH, K., JORDAN, S., BEUERMANN, K. & GÄNSICKE, B. T. (2005b) Zeeman tomography of magnetic white dwarfs II. The quadrupole-dominated magnetic field of HE 1045–0908. *A&A*, **442**, 651–660 (Paper II). [53](#)
- FABRIKA, S. & VALYAVIN, G. (1999) Observations of white dwarfs magnetic fields in the sub-megagauss region. In *11<sup>th</sup> European Workshop on White Dwarfs*, edited by J.-E. Solheim & E. G. Meistas, no. 169 in ASP Conf. Ser., Astronomical Society of the Pacific, San Francisco. [2](#), [34](#)
- FASSBINDER, P. & SCHWEIZER, W. (1996) Stationary hydrogen lines in magnetic and electric fields of white dwarf stars. *A&A*, **314**, 700–706. [64](#)
- FONTAINE, G., THOMAS, J. H. & VAN HORN, H. M. (1973) On the Evolution of Magnetic White Dwarfs. *ApJ*, **184**, 911–916. [4](#)
- FORSTER, H., STRUPAT, W., RÖSNER, W., WUNNER, G., RUDER, H. & HEROLD, H. (1984) *J. Phys. V*, **17**, 1301. [1](#), [10](#), [38](#), [55](#)
- GÄNSICKE, B. T. & BEUERMANN, K. (1996) The cooling of the white dwarf in VW Hyi. *A&A*, **309**, L47. [20](#)



- GÄNSICKE, B. T., EUCHNER, F. & JORDAN, S. (2002) Magnetic white dwarfs in the Early Data Release of the Sloan Digital Sky Survey. *A&A*, **394**, 957–963. 2, 69
- GÄNSICKE, B. T., HOARD, D. W., BEUERMANN, K., SION, E. M. & SZKODY, P. (1998) HST/GHRS observations of AM Herculis. *A&A*, **338**, 933–946. 20
- GAUSS, C. F. (1838) Allgemeine Theorie des Erdmagnetismus. In *Resultate magn. Verein 1838*, reprinted in: Werke, Vol. 5, p. 121. 41
- GREEN, R. F., SCHMIDT, M. & LIEBERT, J. (1987) *ApJS*, **61**, 305. 53
- HARDORP, J., SHORE, S. N. & WITTMANN, A. (1976) Line Formation with Magnetic Field: Review and Practical Applications. In *Physics of Ap stars*, edited by W. W. Weiss, H. Jenkner & H. J. Wood, no. 32 in IAU Coll. 9
- HEBER, U., NAPIWOTZKI, R. & REID, I. N. (1997) Rotation velocities of white dwarf stars. *A&A*, **323**, 819–826. 2
- HENRY, R. J. W. & O’CONNELL, R. F. (1984) *ApJ*, **282**, L97. 1
- HENRY, R. J. W. & O’CONNELL, R. F. (1985) *PASP*, **97**, 333. 1
- HOLBERG, J. B., BARSTOW, M. A., BRUHWEILER, F. C., CRUISE, A. M. & PENNY, A. J. (1998) Sirius B: A New, More Accurate View. *ApJ*, **497**, 935–942. 1
- JEHIN, E., O’BRIEN, K. & SZEIFERT, T. (2004) *FORS1+2 User Manual 2.8*. European Southern Observatory, VLT-MAN-ESO-13100-1543. 36
- JORDAN, S. (1992) Models of white dwarfs with high magnetic fields. *A&A*, **265**, 570–576. 10, 64
- JORDAN, S. (2001) Magnetic White Dwarfs. In *12<sup>th</sup> European Workshop on White Dwarfs*, edited by J. L. Provençal, H. L. Shipman, J. MacDonald & S. Goodchild, no. 226 in ASP Conf. Ser., Astronomical Society of the Pacific, San Francisco. 8, 10
- JORDAN, S. & FRIEDRICH, S. (2002) Search for variations in circular-polarization spectra of the magnetic white dwarf LP 790–29. *A&A*, **383**, 519–523. 3
- JORDAN, S. & MERANI, N. (1995) The Influence of the Bound-Free Opacity on the Radiation from Magnetic DA White Dwarfs. In *9<sup>th</sup> European Workshop on White Dwarfs*, edited by D. Koester & K. Werner, no. 443 in Lecture Notes in Physics, Springer Verlag, Berlin. 10, 65
- JORDAN, S., SCHMELCHER, P. & BECKEN, W. (2001) Stationary components of He I in strong magnetic fields – a tool to identify magnetic DB white dwarfs. *A&A*, **376**, 614–620. 3, 69
- JORDAN, S., WERNER, K. & O’TOOLE, S. J. (2005) Discovery of magnetic fields in central stars of planetary nebulae. *A&A*, **432**, 273–279. 2, 34, 52
- KAWKA, A. (2003) *A Study of White Dwarfs in the Solar Neighbourhood*. Dissertation, Murdoch University, Perth, Australia. 2, 5
- KOESTER, D. & HERRERO, A. (1988) Non-local thermodynamic equilibrium line profiles, rotation, and magnetic fields in seven DA white dwarfs. *ApJ*, **332**, 910–916. 2

- KOESTER, D., SCHULZ, H. & WEIDEMANN, V. (1979) *A&A*, **76**, 262. 10
- KUBE, J., GÄNSICKE, B. T. & BEUERMANN, K. (2000) Eclipse mapping of the accretion stream in UZ Fornacis. *A&A*, **356**, 490–500. 20
- KUBE, J., GÄNSICKE, B. T., EUCHNER, F. & HOFFMANN, B. (2003) CVcat: An interactive database on cataclysmic variables. *A&A*, **404**, 1159–1163. 89
- LAMB, F. K. & SUTHERLAND, P. G. (1974) Continuum Polarization in Magnetic White Dwarfs. In *Physics of Dense Matter*, edited by C. J. Hansen, no. 53 in IAU Symp., Reidel, Dordrecht. 10
- LANGEL, R. A. (1987) The Main Field. In *Geomagnetism*, edited by J. A. Jacobs, vol. 1, Academic Press, London, p. 249. 10, 41, 58
- LATTER, W. B., SCHMIDT, G. D. & GREEN, R. F. (1987) The rotationally modulated Zeeman spectrum at nearly  $10^9$  Gauss of the white dwarf PG 1031+234. *ApJ*, **320**, 308–314. 3
- LIEBERT, J., BERGERON, P. & HOLBERG, J. B. (2003) The True Incidence of Magnetism Among Field White Dwarfs. *AJ*, **125**, 348–353. 2, 34, 52
- MARKIEL, J. A., THOMAS, J. H. & VAN HORN, H. M. (1994) Dynamo generation of magnetic field in the white dwarf GD 358. *ApJ*, **430**, 834–838. 4
- MATHYS, G. (2001) Magnetic Fields of Ap and Bp Stars. In *Magnetic Fields Across the Hertzsprung-Russell Diagram*, edited by G. Mathys, S. K. Solanki & D. T. Wickramasinghe, no. 248 in ASP Conf. Ser., Astronomical Society of the Pacific, San Francisco. 4
- MAXTED, P. F. L., FERRARIO, L., MARSH, T. R. & WICKRAMASINGHE, D. T. (2000) WD 1953–011: a magnetic white dwarf with peculiar field structure. *MNRAS*, **315**, L41–L44. 34
- MCCOOK, G. P. & SION, E. M. (1999) A Catalog of Spectroscopically Identified White Dwarfs [4th Edition]. *ApJS*, **121**, 1. 2, 52
- MERANI, N., MAIN, J. & WUNNER, G. (1995) Atomic Data for Bound-Bound and Bound-Free Opacities of Hydrogen in a Strong Magnetic Field. In *Astrophysical Applications of Powerful New Databases*, edited by S. J. Adelman & W. L. Wiese, no. 78 in ASP Conf. Ser., Astronomical Society of the Pacific, San Francisco. 10
- MINKOWSKI, R. (1938) Ann. Rep. Mount Wilson Observatory, p. 28. 1
- MUSLIMOV, A. G., VAN HORN, H. M. & WOOD, M. A. (1995) Magnetic Field Evolution in White Dwarfs: The Hall Effect and Complexity of the Field. *ApJ*, **442**, 758–767. 8, 34, 48, 72
- NELDER, J. A. & MEAD, R. (1965) A simplex method for function minimization. *Computer Journal*, **7**, 308–313. 22
- O'TOOLE, S. J., JORDAN, S., FRIEDRICH, S. & HEBER, U. (2005) Discovery of magnetic fields in hot subdwarfs. *A&A*, **437**, 227–234. 2, 34, 52
- PRESS, W. H., TEUKOLSKY, S. A., VETTERLING, W. T. & FLANNERY, B. P. (1992) *Numerical Recipes in C*. 2nd edn., Cambridge University Press. 22

- PUTNEY, A. & JORDAN, S. (1995) Off-Centered Dipole Models for 3 Isolated Magnetic White Dwarfs. *ApJ*, **449**, 863. [8](#)
- RAHN, T. (1999) *Modellierung phasenaufgelöster Spektren magnetischer Weißer Zwerge*. Diplomarbeit, Christian-Albrechts-Universität, Kiel, Germany. [10](#)
- RAMATY, R. (1969) *ApJ*, **158**, 753. [9](#)
- RECHENBERG, I. (1994) *Evolutionsstrategie '94*. No. 1 in Werkstatt Bionik und Evolutionstechnik, frommann-holzboog, Stuttgart. [20](#)
- REID, I. N., LIEBERT, J. & SCHMIDT, G. D. (2001) Discovery of a Magnetic DZ White Dwarf with Zeeman-Split Lines of Heavy Elements. *ApJ Lett.*, **550**, L61–L63. [xix](#), [4](#)
- REIMERS, D., JORDAN, S. & CHRISTLIEB, N. (2004) HE 0241–0155 – Evidence for a large scale homogeneous field in a highly magnetic white dwarf. *A&A*, **414**, 1105–1108. [xix](#), [4](#), [34](#)
- REIMERS, D., JORDAN, S., KÖHLER, T. & WISOTZKI, L. (1994) HE 1045–0908: a new magnetic DA white dwarf with a distinctive Zeeman line splitting pattern. *A&A*, **285**, 995–997. [35](#)
- RÖSNER, W., WUNNER, G., HEROLD, H. & RUDER, H. (1984) *J. Phys. V*, **17**, 29. [1](#), [10](#), [38](#), [55](#)
- SCHMIDT, G. D., HARRIS, H. C., LIEBERT, J., EISENSTEIN, D. J., ANDERSON, S. F., BRINKMANN, J., HALL, P. B., HARVANEK, M. ET AL. (2003) Magnetic White Dwarfs from the Sloan Digital Sky Survey: The First Data Release. *ApJ*, **595**, 1101–1113 (S03). [xix](#), [2](#), [3](#), [4](#), [5](#), [34](#), [52](#), [69](#), [72](#), [89](#)
- SCHMIDT, G. D. & NORSWORTHY, J. E. (1991) Rotation and magnetism in white dwarfs. *ApJ*, **366**, 270. [2](#), [53](#), [55](#)
- SCHMIDT, G. D., VENNES, S., WICKRAMASINGHE, D. T. & FERRARIO, L. (2001) Studies of magnetic and suspected-magnetic southern white dwarfs. *MNRAS*, **328**, 203–210. [3](#), [35](#), [36](#), [38](#), [46](#), [47](#)
- SCHMIDT, G. D., WEST, S. C., LIEBERT, J., GREEN, R. F. & STOCKMAN, H. S. (1986) The new magnetic white dwarf PG 1031+234: Polarization and field structure at more than 500 million Gauss. *ApJ*, **309**, 218–229. [3](#)
- SCHWOPE, A. D. (1995) Accretion and magnetism – AM Herculis stars. *Rev. Mod. Astron.*, **8**, 125–146. [8](#)
- SEMEL, M. (1989) Zeeman-Doppler imaging of active stars I. Basic principles. *A&A*, **225**, 456–466. [8](#)
- SION, E., GREENSTEIN, J. L., LANDSTREET, J. D., LIEBERT, J., SHIPMAN, H. L. & WEGNER, G. A. (1983) A proposed new white dwarf spectral classification system. *ApJ*, **269**, 253–257. [1](#)
- TAKEDA, Y. (1991) *PASJ*, **43**, 719. [9](#)
- THOMAS, J. H., MARKIEL, J. A. & VAN HORN, H. M. (1995) Dynamo Generation of Magnetic Fields in White Dwarfs. *ApJ*, **453**, 403–410. [4](#)

- TOUT, C. A., WICKRAMASINGHE, D. T. & FERRARIO, L. (2004) Magnetic fields in white dwarfs and stellar evolution. *MNRAS*, **355**, L13–L16. 5, 34
- TRINT, K. & UTECHT, U. (1994) <ftp://biobio.bionik.tu-berlin.de/pub/software/evoC/>. 20
- UNNO, W. (1956) *PASJ*, **8**, 108. 9
- VANLANDINGHAM, K. M., SCHMIDT, G. D., EISENSTEIN, D. J., HARRIS, H. C., ANDERSON, S. F., HALL, P. B., LIEBERT, J., SCHNEIDER, D. P. ET AL. (2005) Magnetic White Dwarfs from the SDSS. II. The Second and Third Data Releases. *AJ*, **130**, 734–741 (V05). xix, 2, 3, 4, 52, 69, 72, 89
- VENNES, S. (1999) Properties of Hot White Dwarfs in Extreme-Ultraviolet/Soft X-Ray Surveys. *ApJ*, **525**, 995–1008. 3
- VILLATA, M. (1992) Angular momentum loss by a stellar wind and rotational velocities of white dwarfs. *MNRAS*, **257**, 450–454. 2
- WENDELL, C. E., VAN HORN, H. M. & SARGENT, D. (1987) Magnetic field evolution in white dwarfs. *ApJ*, **313**, 284–297. 34, 48, 72
- WESEMAEL, F., GREENSTEIN, J. L., LIEBERT, J., LAMONTAIGNE, R., FONTAINE, G., BERGERON, P. & GLASPEY, J. W. (1991) An Atlas of Optical Spectra of White-Dwarf Stars. *PASP*, **105**, 761–778. 1
- WICKRAMASINGHE, D. T. & CROPPER, M. (1988) Spectropolarimetry of the magnetic white dwarf PG 1015+014: evidence for a 100-MG field. *MNRAS*, **235**, 1451–1465 (WC88). 8, 53, 55, 59, 68
- WICKRAMASINGHE, D. T. & FERRARIO, L. (2000) Magnetism in Isolated and Binary White Dwarfs. *PASP*, **112**, 873–924 (WF00). xix, 2, 3, 4, 8, 34, 52, 53, 66, 89
- WICKRAMASINGHE, D. T. & FERRARIO, L. (2005) The origin of the magnetic fields in white dwarfs. *MNRAS*, **356**, 1576–1582. 5
- WICKRAMASINGHE, D. T. & MARTIN, B. (1979) Solutions for radiative transfer in magnetic atmospheres. *MNRAS*, **189**, 883. 9
- WICKRAMASINGHE, D. T., SCHMIDT, G., FERRARIO, L. & VENNES, S. (2002) On the nature of the magnetic DB white dwarfs. *MNRAS*, **332**, 29–33. 69
- WINGET, D. E., NATHER, R. E., CLEMENS, J. C., PROVENCAL, J., KLEINMAN, S. J., BRADLEY, P. A., WOOD, M. A., CLAVER, C. F. ET AL. (1991) Asteroseismology of the DOV star PG 1159–035 with the Whole Earth Telescope. *ApJ*, **378**, 326–346. 2
- WISOTZKI, L., KÖHLER, T., GROOTE, D. & REIMERS, D. (1996) The Hamburg/ESO survey for bright QSOs. I. Survey design and candidate selection procedure. *A&AS*, **115**, 227–233. 35
- WOOD, M. A. (1995) Theoretical White Dwarf Luminosity Functions: DA Models. In *9<sup>th</sup> European Workshop on White Dwarfs*, edited by D. Koester & K. Werner, no. 443 in Lecture Notes in Physics, Springer Verlag, Berlin. 72

- WUNNER, G., RÖSNER, W., HEROLD, H. & RUDER, H. (1985) Stationary hydrogen lines in white dwarf magnetic fields and the spectrum of the magnetic degenerate Grw +70°8247. *A&A*, **149**, 102. [1](#), [10](#), [38](#), [55](#)
- ZHANG, E.-H., ROBINSON, E. L. & NATHER, R. E. (1986) The eclipses of cataclysmic variables. I – HT Cassiopeiae. *ApJ*, **305**, 740–758. [41](#)



# Acknowledgements / Danksagungen

In allererster Linie gilt mein Dank Klaus Beuermann, der diese Arbeit betreut hat. In den etlichen Jahren, die ich bei ihm arbeiten durfte, habe ich viel gelernt. Herzlichen Dank! Sami Solanki vom MPS Lindau, der freundlicherweise das Korreferat übernommen hat, bin ich ebenfalls zu Dank verpflichtet. Herzlich bedanken möchte ich mich bei Stefan Dreizler für die freundliche Aufnahme in seine Arbeitsgruppe und für die gute Zusammenarbeit beim *AstroCat*-Projekt.

Einen ganz großen Dank muss ich loswerden an Stefan Jordan. Ohne seine Modellspektren wäre diese Arbeit nicht möglich gewesen. Lieber Stefan: Die Zusammenarbeit mit dir hat riesigen Spaß gemacht, und deine Besuche in Göttingen waren immer Höhepunkte im sonstigen Alltagstrott – insbesondere auch die „Nachsitzungen“. Klare Sache und damit hopp! Ebenso großer Dank gebührt Boris Gänsicke. Ich durfte sowohl im Zuge dieser Arbeit als auch bei *AstroCat* mit ihm zusammenarbeiten und kann seine Qualitäten als Kollege und als Mensch nicht hoch genug rühmen. Auch seine aktive Beteiligung an der einen oder anderen Nachsitzung soll nicht unerwähnt bleiben. Klaus Reinsch gilt ebenfalls mein Dank. Er hat nicht nur die Beobachtungsdaten aufgenommen, die Grundlage dieser Arbeit sind, sondern war auch stets ein kompetenter Ansprechpartner und verlässlicher Helfer bei allen größeren und kleineren Computerproblemen. Besonders sympathisch war mir immer sein enthusiastischer Einsatz für das Instituts-Volleyball, der mir erst den Zugang zu diesem Spiel eröffnete und viele schöne Mittwochnachmittage an der alten Sternwarte bescherte. Vielen Dank, Klaus! Danken möchte ich auch Rick Hessman, von dem ich insbesondere in meiner Anfangszeit an der Sternwarte viel gelernt habe.

Meinem Freund und ehemaligen Zimmerkollegen Alexander Pollmer danke ich für die schöne gemeinsame Zeit im *AstroCat*-Projekt. An die vielen Fußballabende bei Nino nach der Arbeit denke ich gerne zurück. Auch einem weiteren ehemaligen Zimmerkollegen, Jens Kube, möchte ich ganz besonders danken. Das Titelbild dieser Arbeit habe ich mit seinem genialen Programm *OGLstar* erstellt. Die Tatsache, dass ich „seinen“ Posten bei *AstroCat* übernehmen durfte, gab mir die Gelegenheit, mich persönlich weiterzuentwickeln und viel zu lernen. Vielen Dank, Jens, für die gute Zusammenarbeit, und bleib’ *AstroCat*/*CVcat* weiterhin treu!

Zum Gelingen dieser Arbeit hat nicht zuletzt die gute Arbeitsatmosphäre am Institut beigetragen. Ich bin vielen Kolleginnen und Kollegen dafür zu Dank verpflichtet. In erster Linie will ich hier Sonja Schuh nennen, die „Scheffin“ vom oberen Flur, aber natürlich auch die weiteren „Gang“-Mitglieder: Christian Hettlage, Derek Homeier, Simon Hügelmeier, Holger Israel, Matthias König, Robert Schwarz, Thorsten Stahn und Jörg Steiper.

In der Zeit meines Wirkens an der Sternwarte habe ich viele weitere nette Menschen und interessante Kollegen kennengelernt. Einigen noch nicht genannten möchte ich ebenfalls meinen Dank für die schöne gemeinsame Zeit am Institut aussprechen: Vadim Burwitz, Stefan Eisenbart, Essam El-Kholy, Andreas Fischer, Tina Hoffmann und Matthias Schreiber.



Außerdem danke ich den Institutssekretärinnen Ute Kellermann, Monika Scheja, Nicole Böker und Klaudia Wolters für ihre stets freundliche Hilfe in vielen Dingen, insbesondere mit der leidigen Bürokratie.

Ich möchte weiterhin ganz besonders fünf langjährigen Freunden und Mit-Physikern danken, die mir auf verschiedenen Etappen meiner Karriere als Physiker hilfreich zur Seite standen: Matthias Spangenberg, Danijel Schorlemmer, Jörg Wichard, Martin Bednarzik und Lars-Oliver Kautschor.

Herzlichen Dank auch an Christina König für ihre kompetente Hilfe in sprachlichen Fragen und unzähligen anderen Dingen.

Meinen Eltern sowie meiner Schwester Sibylle und meinem Schwager Marcus gebührt ein großer Dank für ihre Unterstützung meiner wissenschaftlichen Aktivitäten und auch für die manchmal notwendige Ablenkung. Ich denke gerne an viele schöne Abende bei schwäbischem Essen und Viertele zurück, sowie an so manche erfolgreich bezwungene Loipe und an so manchen Wandersteig.

Ich danke dem Bundesland Niedersachsen für die Gewährung eines Graduiertenstipendiums, sowie der Berliner-Ungewitter-Stiftung für die Gewährung einer einmaligen finanziellen Beihilfe.

# List of publications

## Refereed Journals

EUCHNER, F., JORDAN, S., BEUERMANN, K., REINSCH, K. & GÄNSICKE, B. T. (2006) Zeeman tomography of magnetic white dwarfs III. The 70–80 Megagauss magnetic field of PG 1015+014. *Astronomy & Astrophysics*, **451**, 671–681 ([doi:10.1051/0004-6361:20064840](https://doi.org/10.1051/0004-6361:20064840)).

EUCHNER, F., REINSCH, K., JORDAN, S., BEUERMANN, K. & GÄNSICKE, B. T. (2005) Zeeman tomography of magnetic white dwarfs II. The quadrupole-dominated magnetic field of HE 1045–0908. *Astronomy & Astrophysics*, **442**, 651–660 ([doi:10.1051/0004-6361:20053038](https://doi.org/10.1051/0004-6361:20053038)).

KUBE, J., GÄNSICKE, B. T., EUCHNER, F. & HOFFMANN, B. (2003) CVcat: An interactive database on cataclysmic variables. *Astronomy & Astrophysics*, **404**, 1159–1163 ([doi:10.1051/0004-6361:20030533](https://doi.org/10.1051/0004-6361:20030533)).

GÄNSICKE, B. T., EUCHNER, F. & JORDAN, S. (2002) Magnetic white dwarfs in the Early Data Release of the Sloan Digital Sky Survey. *Astronomy & Astrophysics*, **394**, 957–963 ([doi:10.1051/0004-6361:20021225](https://doi.org/10.1051/0004-6361:20021225)).

EUCHNER, F., JORDAN, S., BEUERMANN, K., GÄNSICKE, B. T. & HESSMAN, F. V. (2002) Zeeman tomography of magnetic white dwarfs I. Reconstruction of the field geometry from synthetic spectra. *Astronomy & Astrophysics*, **390**, 633–647 ([doi:10.1051/0004-6361:20020726](https://doi.org/10.1051/0004-6361:20020726)).

BEUERMANN, K., WHEATLEY, P. J., RAMSAY, G., EUCHNER, F. & GÄNSICKE, B. T. (2000) Evidence for a substellar secondary in the magnetic cataclysmic binary EF Eridani. *Astronomy & Astrophysics*, **354**, L49–52.

## Conference Proceedings

EUCHNER, F., JORDAN, S., REINSCH, K., BEUERMANN, K. & GÄNSICKE, B. T. (2005) Surface Magnetic Field Distributions of the White Dwarfs PG 1015+014 and HE 1045–0908. In: *Proceedings of the 14<sup>th</sup> European Workshop on White Dwarfs*, edited by D. Koester & S. Moehler, ASP Conf. Ser., Astronomical Society of the Pacific, San Francisco, vol. 334, p. 269.

REINSCH, K., EUCHNER, F., BEUERMANN, K., JORDAN, S. & GÄNSICKE, B. T. (2005) The Structure and Origin of Magnetic Fields on Accreting White Dwarfs. In: *The Astrophysics of Cataclysmic Variables and Related Objects*, edited by J. M. Hameury & J. P. Lasota, ASP Conf. Ser., Astronomical Society of the Pacific, San Francisco, vol. 330, p. 177.

REINSCH, K., EUCHNER, F., BEUERMANN, K. & JORDAN, S. (2004) Magnetic field topology of accreting white dwarfs. In: *Second Cape Workshop on Magnetic Cataclysmic Variables, Proceedings of the 190<sup>th</sup> IAU Colloquium*, edited by S. Vrielmann & M. Cropper, ASP Conf. Ser., Astronomical Society of the Pacific, San Francisco, vol. 315, p. 71–77.

EUCHNER, F., POLLMER, A., GÄNSICKE, B. T., KUBE, J. & BEUERMANN, K. (2004) AstroCat/CVcat: A catalogue on Cataclysmic Variables based on a new framework for online interactive astronomical databases. In: *Astronomical Data Analysis Software and Systems XIII*, edited by F. Ochsenbein, M. G. Allen & D. Egret, ASP Conf. Ser., Astronomical Society of the Pacific, San Francisco, vol. 314, p. 578–581.

EUCHNER, F., POLLMER, A., GÄNSICKE, B. T. & KUBE, J. (2003) AstroCat/CVcat – a framework for web-based interactive astronomical catalogues. *Astronomische Nachrichten*, **324**, Supplementary Issue 3, p. 177.

GÄNSICKE, B. T., EUCHNER, F. & JORDAN, S. (2003) Magnetic white dwarfs in the SDSS. In: *White Dwarfs, Proceedings of the 13<sup>th</sup> European Workshop on White Dwarfs*, edited by D. de Martino, R. Kalytis, R. Silvotti & J. E. Solheim, no. XIII in NATO Science Ser. II, Kluwer, Dordrecht, vol. 105, p. 199.

EUCHNER, F., BEUERMANN, K., REINSCH, K., JORDAN, S., HESSMAN, F. V. & GÄNSICKE, B. T. (2003) Zeeman tomography of magnetic white dwarfs: General method and application to EF Eridani. In: *White Dwarfs, Proceedings of the 13<sup>th</sup> European Workshop on White Dwarfs*, edited by D. de Martino, R. Kalytis, R. Silvotti & J. E. Solheim, no. XIII in NATO Science Ser. II, Kluwer, Dordrecht, vol. 105, p. 195.

# Curriculum Vitae

Dipl.-Phys. Fabian Euchner  
Landwacht 10 B  
37075 Göttingen

7. Sep. 1970	geboren in Kronberg/Taunus, Staatsangehörigkeit: deutsch
Aug. 1976 – Jul. 1980	Grundschule Göttingen-Herberhausen
Aug. 1980 – Jul. 1982	Orientierungsstufe Lutherschule, Göttingen
Aug. 1982 – Jun. 1989	Max-Planck-Gymnasium, Göttingen
11. Mai 1989	allgemeine Hochschulreife
Okt. 1989 – Sep. 1990	Wehrdienst in Koblenz und Göttingen
Okt. 1990 – Sep. 1993	Physikstudium an der Georg-August-Universität Göttingen
7. Mai 1993	Vordiplom in Physik, Georg-August-Universität Göttingen
Okt. 1993 – Sep. 1994	Physikstudium an der Technischen Universität Berlin
ab Okt. 1994	Fortsetzung des Studiums an der Georg-August-Universität Göttingen
Okt. 1996 – Okt. 1998	Diplomarbeit an der Universitäts-Sternwarte Göttingen
30. Okt. 1998	Diplom in Physik, Georg-August-Universität Göttingen
Aug. 1999 – Jul. 2001	Promotionsstipendiat (Graduiertenförderung des Landes Niedersachsen)
Okt. 1997 – Okt. 1998	studentische Hilfskraft, Universitäts-Sternwarte Göttingen
Nov. 1998 – Jul. 2001	wissenschaftliche Hilfskraft, Universitäts-Sternwarte Göttingen
Aug. 2001 – Dez. 2002	wissenschaftlicher Mitarbeiter, Universitäts-Sternwarte Göttingen (BMBF/DLR)
Jan. 2003 – Mär. 2006	wissenschaftlicher Mitarbeiter, Institut für Astrophysik / Universitäts-Sternwarte Göttingen (DFG)

